SPECinc
stratton park engineering company inc
cloud physics and instrumentation
3022 Sterling Circle, Suite 200, Boulder, Colorado 80301, Tel (303) 449-1105, Fax (303) 449-0132

FINAL REPORT

FOR

Analysis of TRMM Microphysical Measurements: Tropical Rainfall Measuring Mission (TRMM)

Submitted to the:

NASA Goddard Space Flight Center
Code 210.5
Greenbelt Road
Greenbelt, MD 20771

February 4, 2004

SPECinc

Final Report
NASA Goddard Space Flight Center
Contract No. NAS5-00244

Analysis of TRMM Microphysical Measurements: Tropical Rainfall Measuring Mission (TRMM) For the Period 3 October 2000 – 30 November 2003

Research activities were focused in the five major areas over the course of this three-year effort:

i. *Software algorithms were developed to improve the analysis of microphysical measurements collected by the TRMM aircraft during the four field campaigns. Particular attention was paid to developing and/or improving algorithms used to compute particle size distributions and ice water content.*

ii. *Software was developed in support of production of the TRMM Common Microphysical Product (CMP) data files.*

iii. *CMP data files for TEFLUN-A field campaign were produced and submitted to the DAAC.*

iv. *Typical microphysical properties of convective and stratiform regions from TEFLUN-A and KWAJEX clouds were produced.*

v. *Typical microphysical and radiative properties of the cloud particles in tropical and continental anvils were analyzed.*

ABSTRACT

SPEC Incorporated participated in three of the four TRMM field campaigns (TEFLUN-A, TEFLUN-B and KWAJEX), installing and operating a cloud particle imager (CPI) and a high volume precipitation spectrometer (HVPS) on the SPEC Learjet in TEFLUN-A, the University of North Dakota Citation in TEFLUN-B and KWAJEX, and a CPI on the NASA DC-8 in KWAJEX. This report presents and discusses new software tools and algorithms that were developed to analyze microphysical data collected during these field campaigns, as well as scientific interpretations of the data themselves.

Software algorithms were developed to improve the analysis of microphysical measurements collected by the TRMM aircraft during the field campaigns. Particular attention was paid to developing and/or improving algorithms used to compute particle size distributions and ice water content. Software was also developed in support of production of the TRMM Common Microphysical Product (CMP) data files. CMP data files for TEFLUN-A field campaign were produced and submitted to the DAAC.

Typical microphysical properties of convective and stratiform regions from TEFLUN-A and KWAJEX clouds were produced. In general, it was found that In the upper cloud region near –20 to –25 ° C, stratiform clouds contain very high (> 1 cm^{-3}) concentrations of small ice particles, which are suspected to be a residual from homogeneous freezing and sedimentation of small drops in a convective updraft. In the upper cloud region near –20 to –25 ° C, convective clouds contain aggregates, which are not found lower in the cloud. Stratiform clouds contain aggregates at all levels, with the majority in the lowest levels. Convective cloud regions contain much higher LWC and drop concentrations than stratiform regions at all levels, and higher IWC in the middle and upper regions. Stratiform clouds contain higher IWC than convective clouds only at the lowest level. Irregular shaped ice particles are found in very high concentrations throughout both convective and stratiform cloud regions.

A striking difference in particle shape in cirrus formed in situ, cirrus formed from maritime anvils and cirrus formed from continental anvils. Over 50% of the mass of in situ cirrus ice particles is composed of bullet rosettes, while bullet rosettes are virtually non-existent in maritime and tropical anvils. Tropical anvils are composed of mostly singular, plates, capped columns, and blocky irregular shapes, while continental anvils have a much higher percentage of aggregates, some of which are chains of small spheroidal particles that appear to result from homogeneous freezing of drops. A correlation between high electric fields in continental anvils and the formation of aggregates is hypothesized.

1. Software Development

Software development pursued multiple goals during the course of this research. Initially software was written that allows the combination of data from multiple particle probes in order to create combined particle size distributions (PSDs) and compute parameters derived from the PSDs. In addition algorithms for automatic classification of ice particles were developed and tested in certain cloud situations.

1.1 Combining PDSs

Algorithms were developed to combine FSSP, CPI, and 2D-C PSDs to obtain a composite PSD that can be used to compute liquid water content (LWC), ice water content (IWC), mean particle size, total particle concentration and other derived parameters. Software written in the IDL language has been developed that enables the user to view FSSP, CPI and 2D-C data so that the CPI data can be scaled. Initially, the CPI is scaled to the 2DC in the 150 – 500 micron size range where the 2D-C measurements are generally thought to be reliable. Examples of PSDs from UND Citation FSSP, CPI and 2D-C data collected from TEFLUN-B are shown in **Figures 1** and **2**. The figures show a comparison of PSDs from 10-km rimed and unrimed regions of a decaying stratiform region. The program allows the user to scale the CPI by whatever single scaling factor seems best. Later in the research, a standalone program was developed that scaled the CPI without the necessity of scaling to the 2D-C probe.

RIMED ICE PARTICLES IN FLORIDA ANVIL AT -38° C (TEFLUN-B 13 AUG 1998)

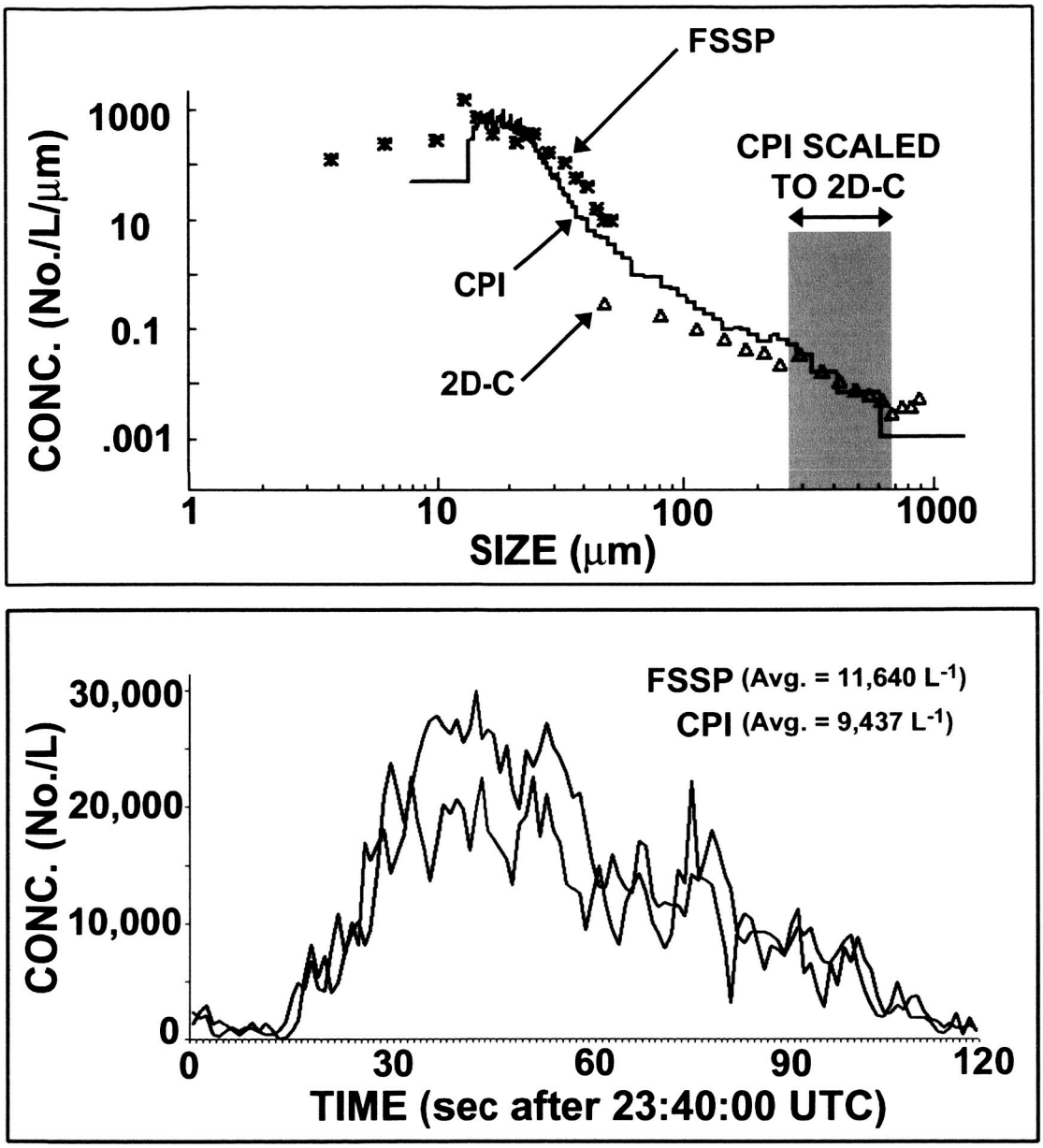

Figure 1. (Top) Particle size distributions from the FSSP, CPI, 2D-C and (bottom) total particle concentration collected in a 10 km region with primarily rimed particles.

UNRIMED ICE PARTICLES IN FLORIDA ANVIL AT -38°C (TEFLUN-B 13 AUG 1998)

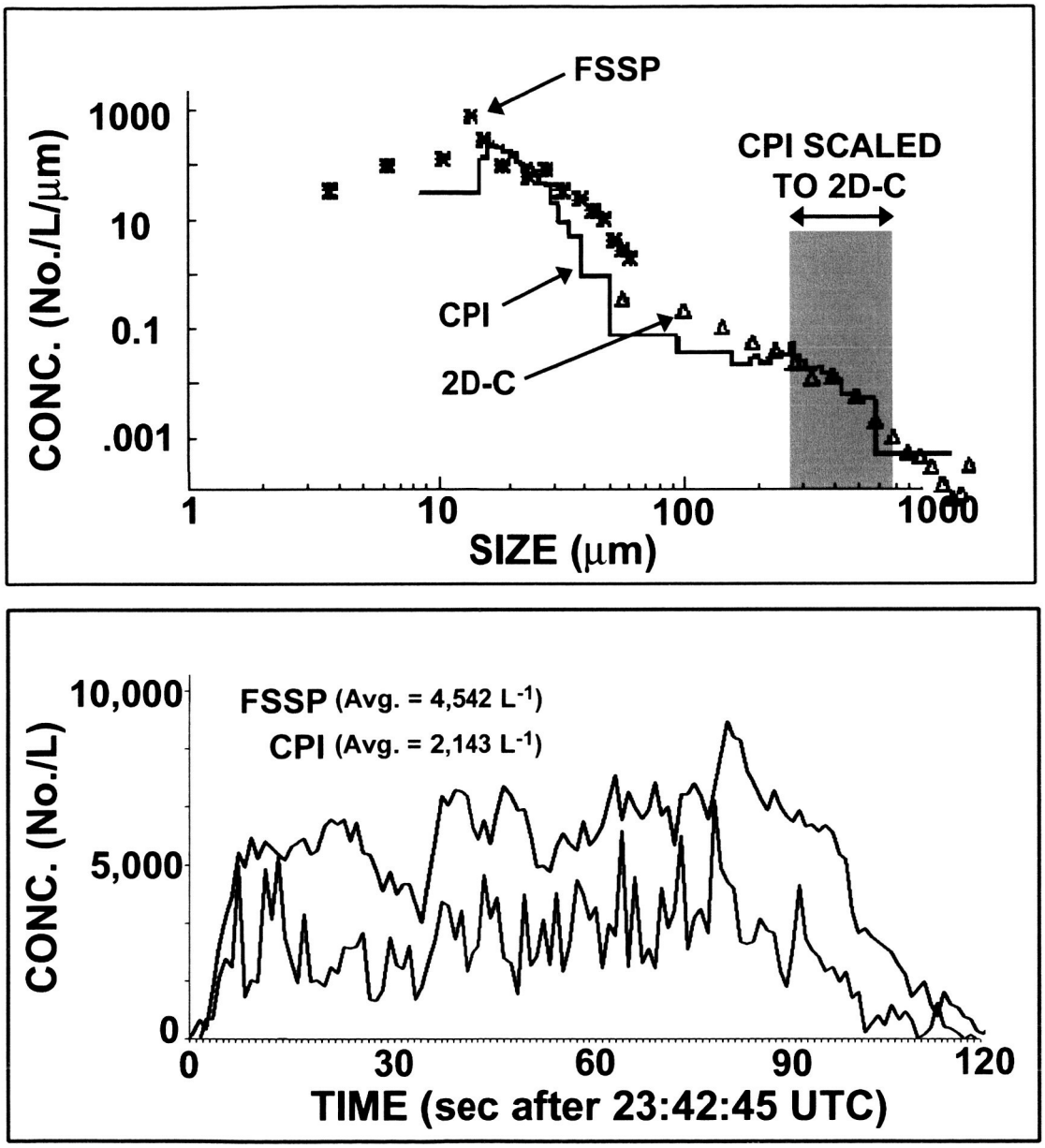

Figure 2. As in Figure 1 except for a 10 km region with unrimed ice particles, located in juxtaposition with the 10 km region shown in Figure 1.

1.2 Self-scaling the Particle Size Distribution (PSD)

The approach to CPI self-scaling is to assume that the largest particles trigger the PDS with near 100% efficiency. This is a theoretically reasonable assumption when there are sufficient particles larger than 150 μm and the probe is not dominated by triggers on coincidence events due to high concentration of small particles. Frames with a particle larger than a given size (say 150 μm) are counted ($\#_{frames}$) and it is assumed that if there is more than one particle in the frame, the other particles were not involved in triggering the PDS. In this case, since we measure the fraction of time that the probe is live and ready to trigger and the fraction of time that the probe is dead, unable to trigger, we can calculate the concentration of particles larger than 150 μm (C_{150}) from the known sample area of the PDS (SA) and the speed of the air through the probe (TAS).

$$C_{150} = \#_{frames} \div (TAS \times SA \times \Delta t) \quad (1)$$

where Δt is the product of the sample time period and the fraction of time that the probe was live. The full CPI PSD is now scaled so that it agrees with the value from equation 1 for C_{150}.

Previously we applied this technique to cirrus data where the PDS was operated at just above noise level. In this case the self-scaling has worked quite well, as shown in **Figure 3.** Examples of CPI self-scaled size distributions are plotted with the FSSP and 2DC size distributions. The agreement is good. We also previously applied the technique to two examples of NASA DC8 data from Kwajex, as shown in **Figure 4**. Here the agreement is poor. The CPI PSD is orders of magnitude low compared to the other probes. We are uncertain as to the exact causes of this discrepancy, however several factors may have contributed. First, we recently learned from investigations during CAMEX4 that the combination of the high vibration level on the DC-8, the long mounting pylon and the absence of a hard rubber gasket between the CPI and pylon (disallowed by NASA engineers) generates vibrations in the imaging optics that strongly degrade the performance of the instrument. This largely results in failures to obtain good background images and a low percentage of frames with valid images. Next, the person operating the CPI was relatively new and inexperienced, and also, at that time there was little known about how to properly set the PDS threshold levels, so they were set higher than desirable. Third, based on CAMEX4 data, it appears that the location of the CPI on top of the fuselage may contribute to selectively missing some of the larger particles.

The self-scaling is meant to scale the PSD for the larger sized particles and is expected to work when those large particles are found usually only one per image frame. For 92 cloud penetrations in cirrus, wave, and stratus clouds we compare the concentration of particles between 150 to 450 microns in size measured by the CPI and measured by the 2DC. The data are presented in

Figure 5 as a scatter plot. This comparison shows that improvement has been achieved in that the CPI is now usually of the correct order of magnitude. While the correlation between the 2DC and CPI in **Figure 5** is not as good as one would like, the scatter between two 2DC probes can exceed an order of magnitude (Gayet et al. 1993), so it is not clear which particle probe in **Figure 5** is in error.

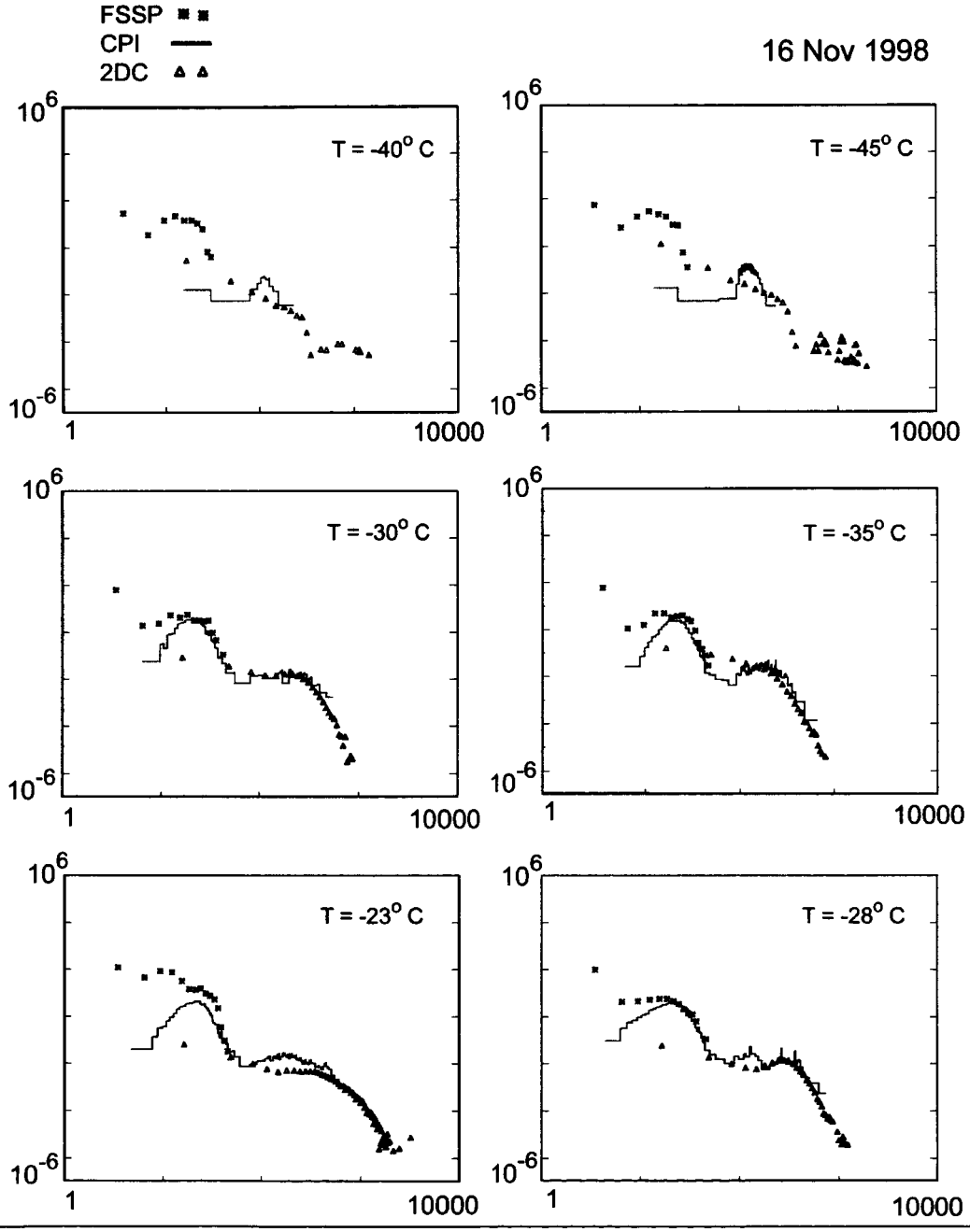

Figure 3. Examples showing comparisons of FSSP, CPI and 2D-C particle size distributions collected at various levels in cirrus where the CPI size distribution has been self-scaled and still agrees well with the size distributions from the other probes.

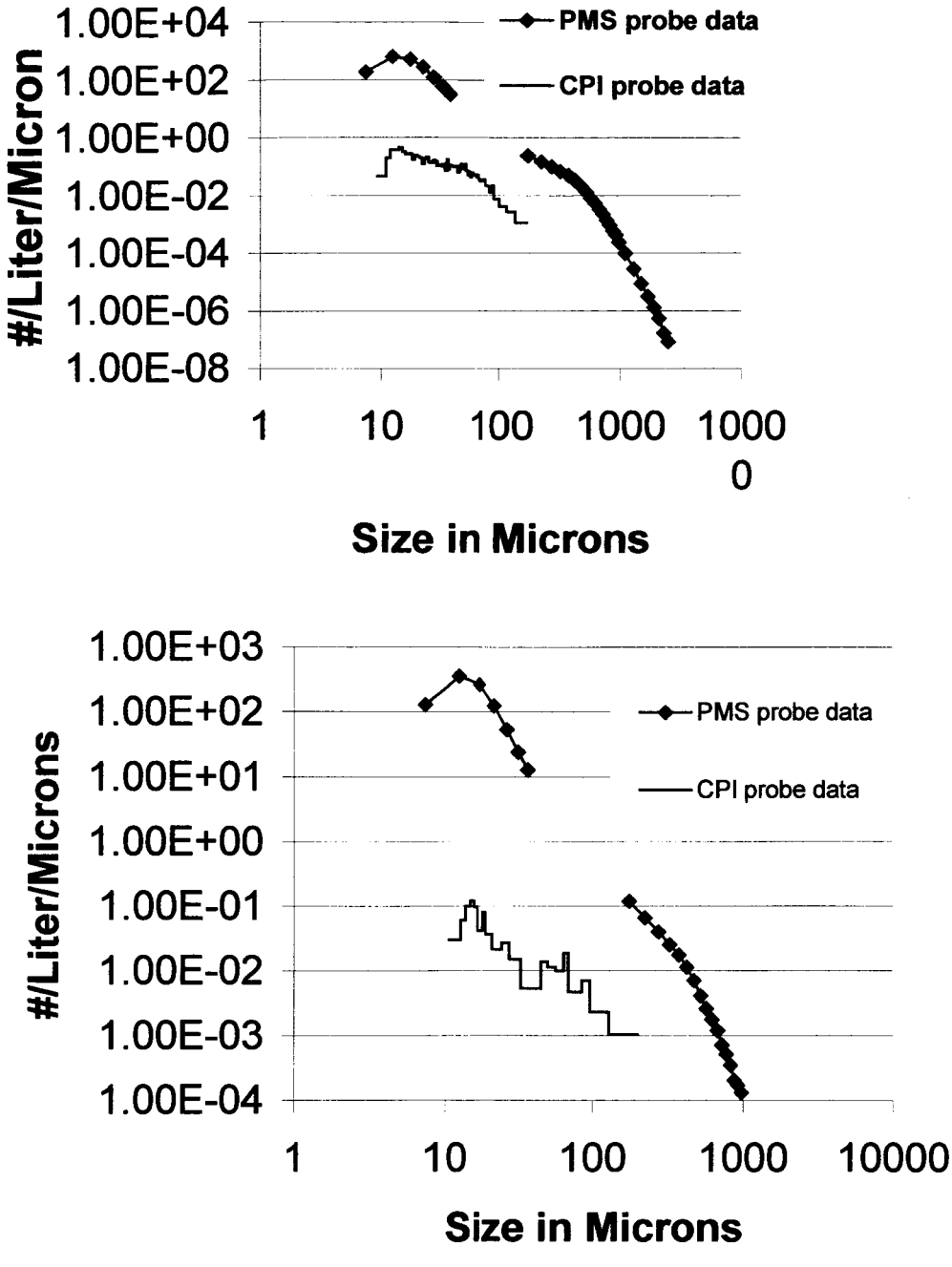

Figure 4. Examples of the CPI software self-scaling of the CPI together with the measurements from the FSSP and 2DC probes where the scaling procedure did not work well, most likely due to CPI hardware intermittencies, operator problems and airflow perturbations associated with the CPI installation on the DC-8.

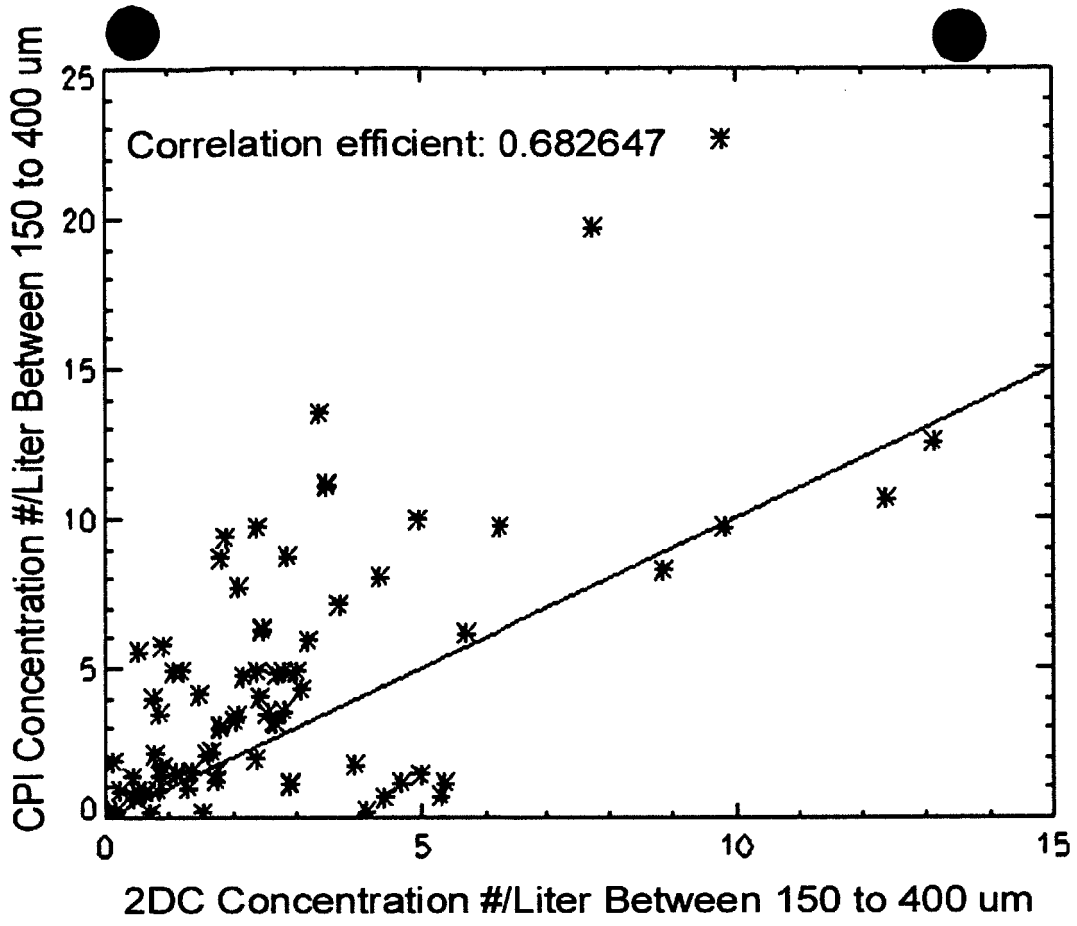

Figure 5. Scatterplot showing comparison of 92 CPI and 2D-C PSDs that have been integrated to obtain the total particle concentration between 150 and 450 μm. A data point represents one integration each from 150 to 450 μm of the PSD curves measured by the 2D-C and CPI for selected time intervals in cirrus, stratus and wave clouds.

1.3 Adjusting the small end of the PSD for Particle Detection System (PDS) sensitivity and adjusting for PDS threshold settings above the optimum level

Initially, we attempted to account for the dependence of the sensitivity of the Particle Detection System (PDS) on particle size and PDS threshold setting simultaneously. We use data collected at the South Pole because of the greater stability of conditions with time compared with aircraft measurements. The attempt was a failure. Subsequently, we made some progress by dividing the problem into two somewhat separable parts. One is adjusting the small size end of the Particle Size Distribution (PSD) for Particle Detection System (PDS) sensitivity when the CPI is run at optimum PDS thresholds. The optimum PDS threshold setting is at just above noise level. The other part is adjusting for PDS threshold settings above the optimum level.

Our first attempt took account of both parts by adjusting for the probability of particle detection where that probability is estimated from the following equation:

$$P_{est} = C_0 - C_1 \times \text{Threshold} + C_2 \times \text{Area} \quad (2)$$

The coefficients (C_0=1.14 C_1=0.00141 C_2=0.00006) were estimated from data collected at the South Pole as described in the second quarterly report of this period. In our more recent attempt we set C_1=0. That is we have not attempted part two, adjusting for PDS threshold settings above the optimum level. Then rather than estimating C_0 and C_2 from the South Pole data, which was taken at relatively low particle velocities and is thus not necessarily representative for aircraft collected data, we set C_0 and C_2 by scaling the CPI size distribution to the FSSP size distribution using cirrus cloud data collected using the SPEC Lear jet. Once values of C_0 = -0.2 and C_2 = 0.00012 were thus obtained, we have continued to use them to this date without modification. We have been pleased with the results so far. During the NASA CRYSTAL-FACE experiment for example, we did no scaling of the CPI PSDs other than that just mentioned above. We used the CPI self-scaling method with the adjustments for PDS sensitivity for small particles described just above and the CPI PSDs generally compared well with the SPP100 PSDs in their overlap region. An example is shown in **Figure 6**.

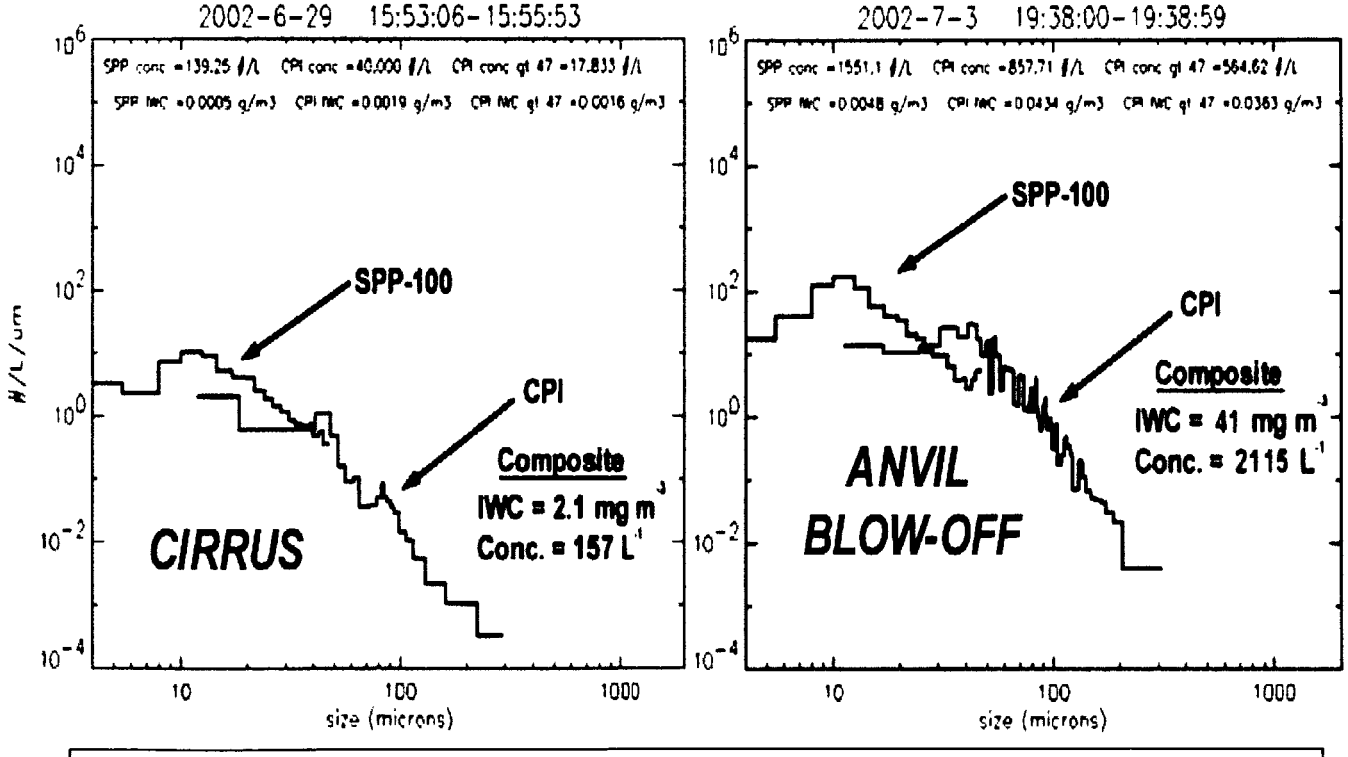

Figure 6. Examples from the CRYSTAL-FACE website showing results of the CPI self-scaling algorithm. The SPP-100 is an FSSP-100 probe with upgraded electronics.

1.4 Improving ice water content measurements from in-situ particle image data.

The ice water content (IWC) of natural clouds is a quantity that is fundamental to several disciplines in the atmospheric sciences, including studies of the formation of the ice phase and precipitation, radiative transfer, cloud chemistry and all numerical models that include cold cloud processes. Airborne techniques to measure IWC vary, but are fundamentally based on two approaches: 1) the mass of ice in a known concentration of cloudy air is melted and then vaporized. Ice mass is related to measurement of the ice vaporization process, either by measuring the vapor added to the sample volume (e.g., Twohy et al. 1997), or the increase of latent heat on the vaporizing substrate (Korolev et al. 1998). 2) Digital images of ice particles are examined and the mass is related to the shape and size of the particle image (e.g., Mitchell et al. 1990; Brown and Francis 1995).

The first technique has the advantage that it measures properties that are directly related to phase changes of ice mass, i.e., the latent heats of fusion and vaporization, and the measurement of ice mass after phase changes from ice to water vapor. Since during phase changes latent heats are known quantities and mass is conserved, these measurement techniques have inherent advantages. On the other hand, two-dimensional images of ice particles do not provide complete information describing the particle volume and ice density, so translation from particle image to mass (called here the size-to-mass relationship) can never be perfect. Although the size-to-mass relationship is not perfect, recording two-dimensional images of ice particles has other significant advantages. For example, particle size distribution and particle shape can be obtained from particle images, but not from measurement techniques that convert ice mass to vapor. Ice particle size distributions and shapes are themselves very important quantities that strongly impact cloud physical and radiative calculations. In addition, the instrumentation used to digitally record two-dimensional cloud particle images has been readily available for the past 30 years (e.g., the 2D-C probe described by Knollenberg 1970). As a result, there are large existing data sets of 2D images that can be re-analyzed if improved particle image-to-mass algorithms can be identified.

The literature contains a number of size-to-mass relationships based on a categorization of the particle type and the maximum dimension of the particle (Bashkirova and Pershina 1964; Heymsfield 1972; Davis 1974; Locatelli and Hobbs 1974; Mitchell et al. 1990; Brown and Francis 1995). All of these relationships take the form $M = \alpha L^{\beta}$, where M is particle mass, L is particle maximum dimension and α and β are constants determined by curve fitting to a population of ice particles. In this paper, we examine the data set used by Mitchell et al. (1990), hereafter M90. The M90 data were obtained by collecting ice particles falling from winter storms onto glass slides positioned near the

surface in the Sierra Nevada Mountains. The ice particles were photographed, brought inside and melted, where the slides of melted drops were again photographed. Later, the slides were analyzed to categorize the ice particles, measure their maximum dimension and the mean diameter of the melted drops. Details of the process are discussed in M90. Our main contributions to Mitchell's work are to use software that automatically measures not only the maximum particle dimension (L), but also the width (W), area (A) and perimeter (P) of the ice particles, and formulate a new relationship that relates these parameters to particle mass. The advantages of the new formulation are: 1) An improved estimate of ice particle mass, and thus IWC in natural clouds, and 2) A single size-to-mass relationship that translates a two-dimensional particle image to mass, without having to sort the images into particle habits (which is often an intractable process when using 2D-C images).

1.4.1 The New Algorithm

Figure 7a shows an example from M90 of ice particle images and equivalent melted drops data collected during their 1986-87 field study. A set of fifty-one 35-mm photographic slides of ice particle and associated melted drop data that were collected during the 1986-87 field season was obtained from Dr. Mitchell. The 35-mm photographic slides were digitally scanned and converted to .tif files. Software code was then written to convert the .tif files to a data format that could be ingested by an existing SPEC software program, named CPIview, which is used to process data from 2D-C and cloud particle imager (CPI) probes. CPIview is commonly used to derive several parameters from CPI images, such as maximum particle dimension, width, area, perimeter, degree of roundness and radial harmonics (Lawson et al. 2001).

Figure 7b shows examples of three of the ice crystals (circled in **Figure 7a**) that were digitally scanned and then ingested by CPIview. The CPIview software automatically finds the perimeter of the particle, which is shown drawn around each particle in **Figure 7b**, and computes the particle dimensions used in this study. **Figure 7c** shows a schematic comparison of the single parameter, maximum particle length (L) used in the M90 analysis, and the four parameters, L, W, A and P, used in the present analysis. The comparison can be explained by considering the relationship

$$M = a X^{b} \tag{3}$$

where

$$X = L \tag{3a}$$

in the M90 analysis, and

$$X = A \times W \times 2(L + W) / P \tag{3b}$$

in the reanalysis. The new relationship, illustrated in **Figure 7c** and called the "new algorithm", improves on the M90 analysis by measuring parameters that describe the shape of the ice particle. In the new algorithm, *A* represents the solid part of the particle on the 2D image, *W* represents its extension out of the 2D plane and $2 \times (L + W)/P$ reflects its decreased average density when its perimeter is convoluted. The new algorithm will over predict the mass of spherically shaped particles with diameters less 100 μm. Since this is physically unrealistic, the algorithm is applied with the condition that, if the computed mass exceeds that of a sphere with diameter equal to *L*/2, then the mass of the equivalent sphere is used. Since small ice particle images are often not perfectly spherical, the particle size where the new algorithm typically transitions to a perfect sphere ranges from about 30 to 50 μm. This is demonstrated in **Figure 8**, which shows the sizes where small particles from a typical data set transition to the equivalent calculation.

M90, the shapes of the particles are considered by classifying each particle as a certain type, and then using a size-to-mass relationship determined for that type of crystal. In the current technique, the particle shape information is included in the single parameter $X = A \times W \times 2 \times (L + W)/P$. In addition to including more parameters, the new technique eliminates the need to initially (manually or algorithmically) classify the images by particle type. Ice particle images in data sets collected by 2D-C probes can rarely be automatically (or manually) classified into the habit categories used by M90, so the shape information supplied by M90 is seldom of practical value.

1.4.2 Errors

The purpose of this research is to explore and reduce the errors involved in this method. The errors we consider here are of two basic types. One is simply the difference between the actual particle masses and their estimated masses using the mass-size relationship. This we call error type I and represent it with the RMS difference. The other is the robustness of the mass-size relationships or how accurately did we find β from the limited data set? This we call error type II and explore it with a bootstrap style analysis. In this application of a bootstrap style analysis, the full data set is subdivided in half and the subsets are analyzed in the same manner as the full data set. This process is repeated one thousand times. The variation of the results of analyses on the subsets provides an estimate of the uncertainty in the result (i.e., β) of analysis on the full data set.

Type I error is a reflection of how many particles must be averaged together to obtain an acceptable estimate of IWC, assuming the relationship is correct on average. *Type II* error deals with whether the size-to-mass relationship is correct on average when applied to data other than the set from which the relationship was built.

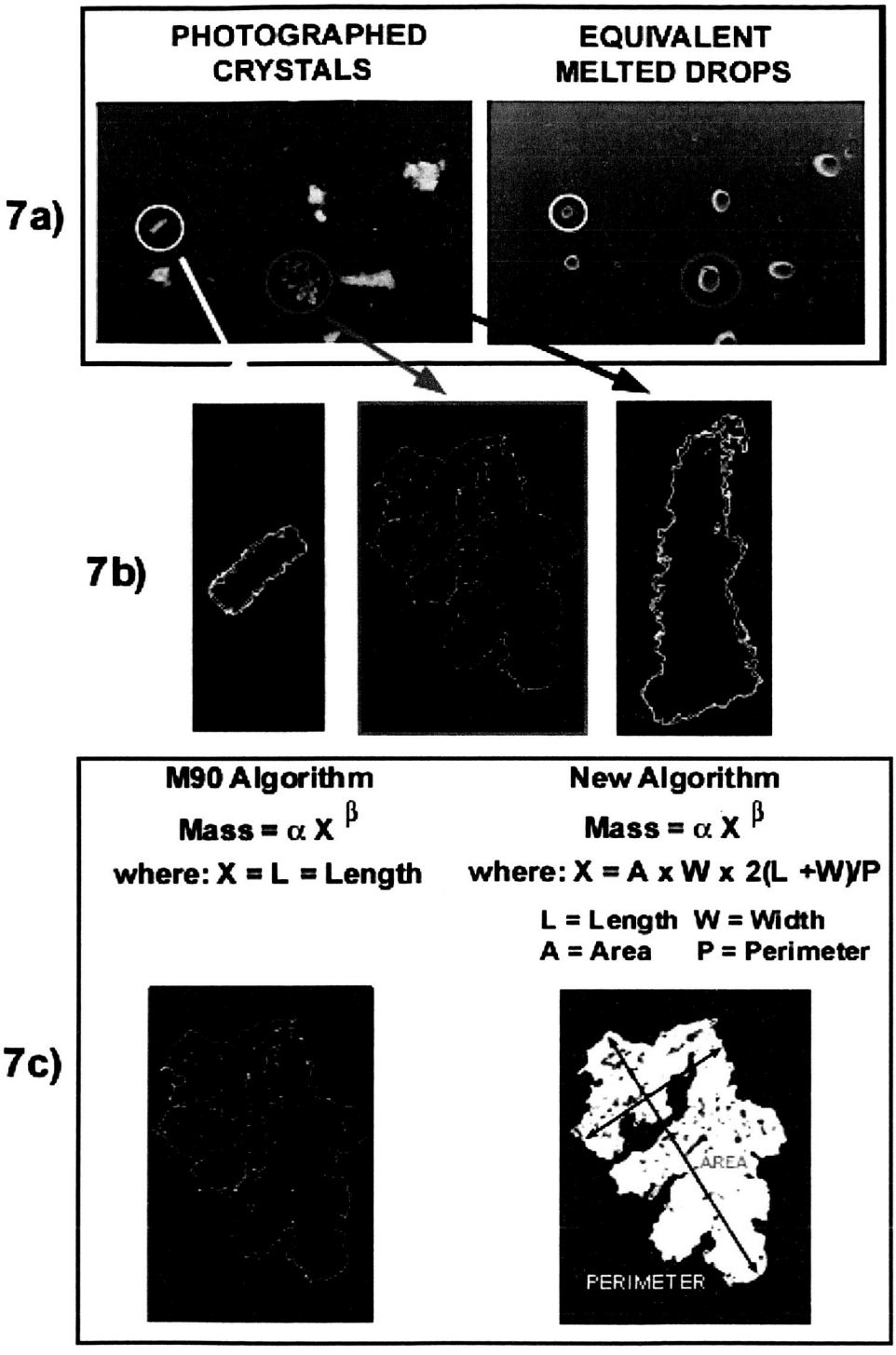

Figure 7. (a) Example of ice crystals photographed on slides under a microscope and equivalent melted drops from the Mitchell et al. (1990) field experiment. (b) Shows examples of three of the ice crystals (circled in Figure 7a) that were digitally scanned and then ingested by CPIview (c) Shows a schematic comparison of the single parameter, maximum particle length (*L*) used in the M90 analysis, and the four parameters, *L*, *W*, *A* and *P*, used in the present analysis.

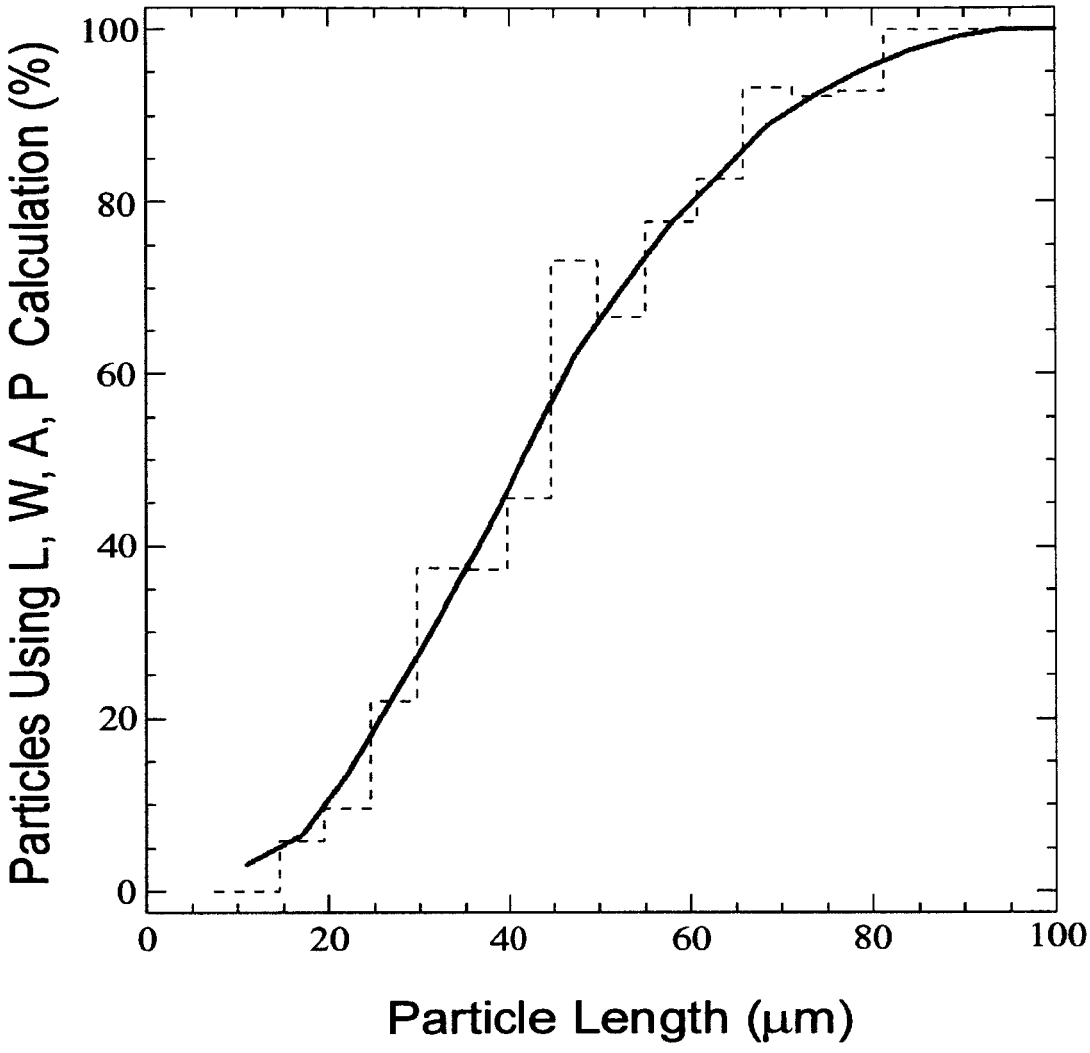

Figure 8. Plot showing percentage versus particle length of ice particles that use the L, W, A, P calculation instead of a spherical assumption. The L, W, A, P algorithm is used whenever the calculated mass is less than the mass of a sphere with diameter equal to L. For example, about 50% of the particles that were 40 microns or larger used the L, W, A, P calculation and 50% used the spherical assumption, while 80% of particles 60 microns and larger used the L, W, A, P calculation. Plot is based on a data set of 842,860 ice particles

The purpose of this research is to quantify the source of the errors in IWC using the Mitchell et al. (1990) methodology and then identify techniques that will lead to improvement in the accuracy of IWC. This work is fundamental to analysis of physical processes in TRMM clouds and for validation of remote sensing estimates of IWC.

Type I error, the differences between actual and estimated masses, can be reduced by basing the estimates on more than one (maximum length) size parameter, or possibly by basing the estimates on a single size parameter other

than maximum length. For example from PMS probe and CPI two-dimensional images, in addition to length (*L*), the area (*A*), perimeter (*P*) and width (*W*) can also be derived. Since CPI images are of much higher resolution than PMS images, additional parameters, such as radial harmonics (*Hs*), which is the Fourier spectrum of the centroid-to-perimeter distance as a function of position along the perimeter, were also calculated for each particle.

As shown in Table 1 in M90, 643 ice crystals were classified in the original study. In our reanalysis, we selected 537 of these ice particle and equivalent melted drop images that we could unambiguously identify. **Figure 9** shows scatter plots of predicted mass versus measured mass for three cases. The first case (**Figure 9a**) is basically a repeat of the analysis procedure used by M90, except it is performed on 537 images from the original data set of 643 images, and the images have not been first classified by crystal type. In this case, the RMS error in the predicted mass is 0.049 mg.

The next plot, **Figure 9b**, shows the same data from M90, but first each of the images has been classified into one of the seventeen crystal habit categories identified in M90. Fitting subsets of the data separately based on particle type should improve predictions, at least for that data set. After classifying the images by particle type, the RMS error in predicted mass is reduced from 0.049 to 0.041 mg.

The third scatter plot, **Figure 9c**, shows the results using the new algorithm, where (3b) has been substituted for X in (3). The result of the new algorithm, shown in **Figure 9c**, yields improvement in the prediction of measured mass over both M90 techniques shown in **Figures 9a** and **9b**. The RMS error in predicted mass is reduced to 0.030 mg. Thus the new parameter, $X = A \times W \times [2 \times (L + W)/P]$, is a much better predictor of mass than length alone, or even length alone but with a different relationship for each crystal type. The best-fit equation to the data in **Figure 9c** yields values of $\alpha = 0.139$ and $\beta = 0.803$.

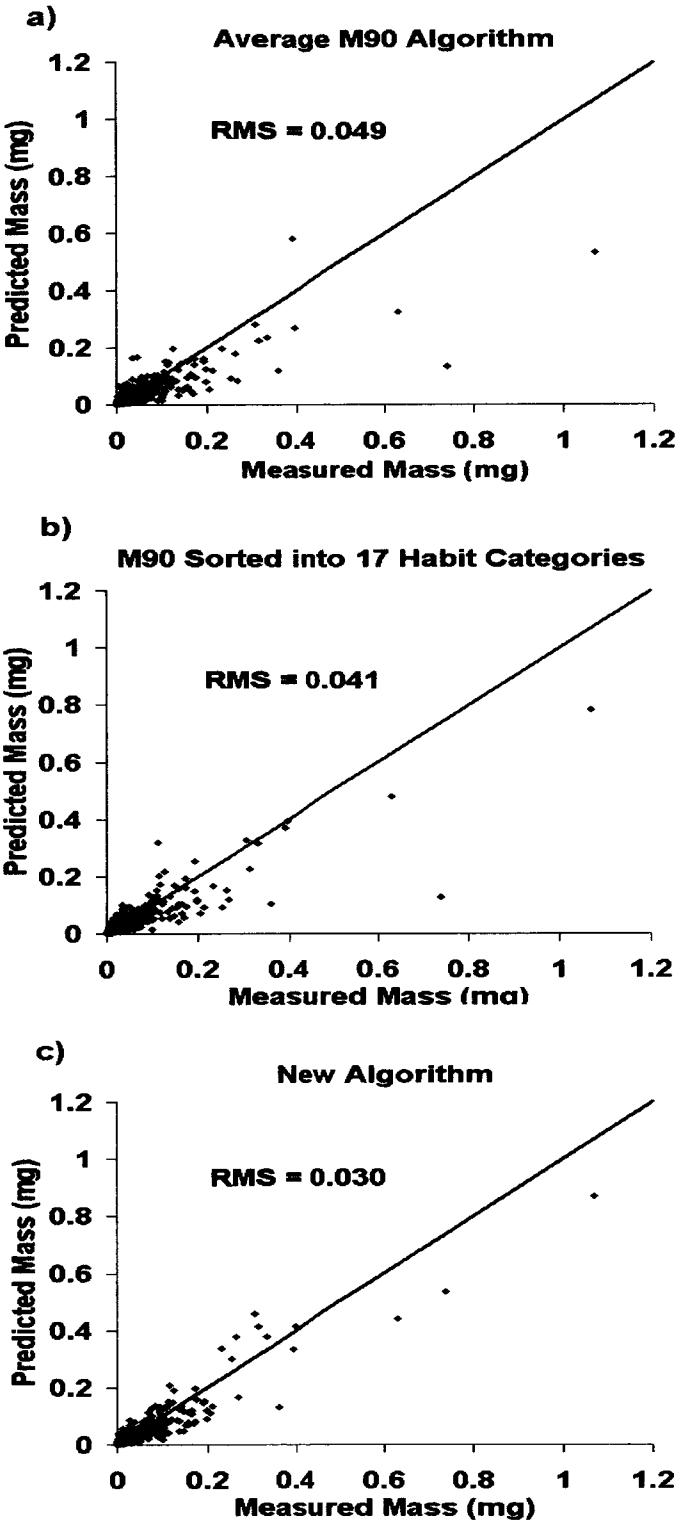

Figure 9. Estimated versus actual masses (in mg) for three cases. Top: The fit is to $X = L$, the length. Middle: Masses are estimated with the M90 habit-conditioned size-to-mass relationships. Bottom: The fit is to $X = A \times W \times [2 (L + W)/P]$, the new algorithm. The RMS errors are shown on each plot.

Since CPIview software was used to analyze the digitized M90 ice crystal photographs, a 2.3 μm (CPI) pixel resolution was incorporated into the computation of the image dimensions, *L, W, A* and *P*. This suggests that when the new algorithm is applied to CPI images, a reduction in RMS error commensurate with the results reported here would be expected. However, when applied to 2D-C images, which typically have poorer pixel resolution, on the order of 25 μm, the resulting improvement may be degraded somewhat. A complete treatment of the error contributed by the coarser resolution of 2D-C images would require extensive simulations. However, some general trends can be predicted using simple examples. For larger particles, say for $L > 1$ mm where the pixel size is < 1% of the typical particle area, the degraded pixel resolution should not significantly increase the error in calculated *M*. For smaller particles, the improvement in RMS error will degrade with decreasing particle size and depends on particle shape. Of course, the original M90 equations are also degraded in a similar way by the coarser resolution of 2D-C images. For example, if the actual $L = 250$ μm, then an individual particle measurement of *L* using 25 μm pixel resolution cannot be more accurate than 10%.

1.5 Automatic Habit Classification

1.5.1 General classification schemes

Figures 10 and **11** show examples of CPI images and pie charts depicting the percentage of various crystal habits, including the percentage of rimed and unrimed particles that have been manually classified by crystal habit. The riming in **Figure 10** suggests that these particles may have previously been in a region associated with convection. The relatively higher total particle concentration associated with the rimed region (compare **Figures 1** and **2**) is also generally indicative of mature and decaying convective regions in TRMM clouds.

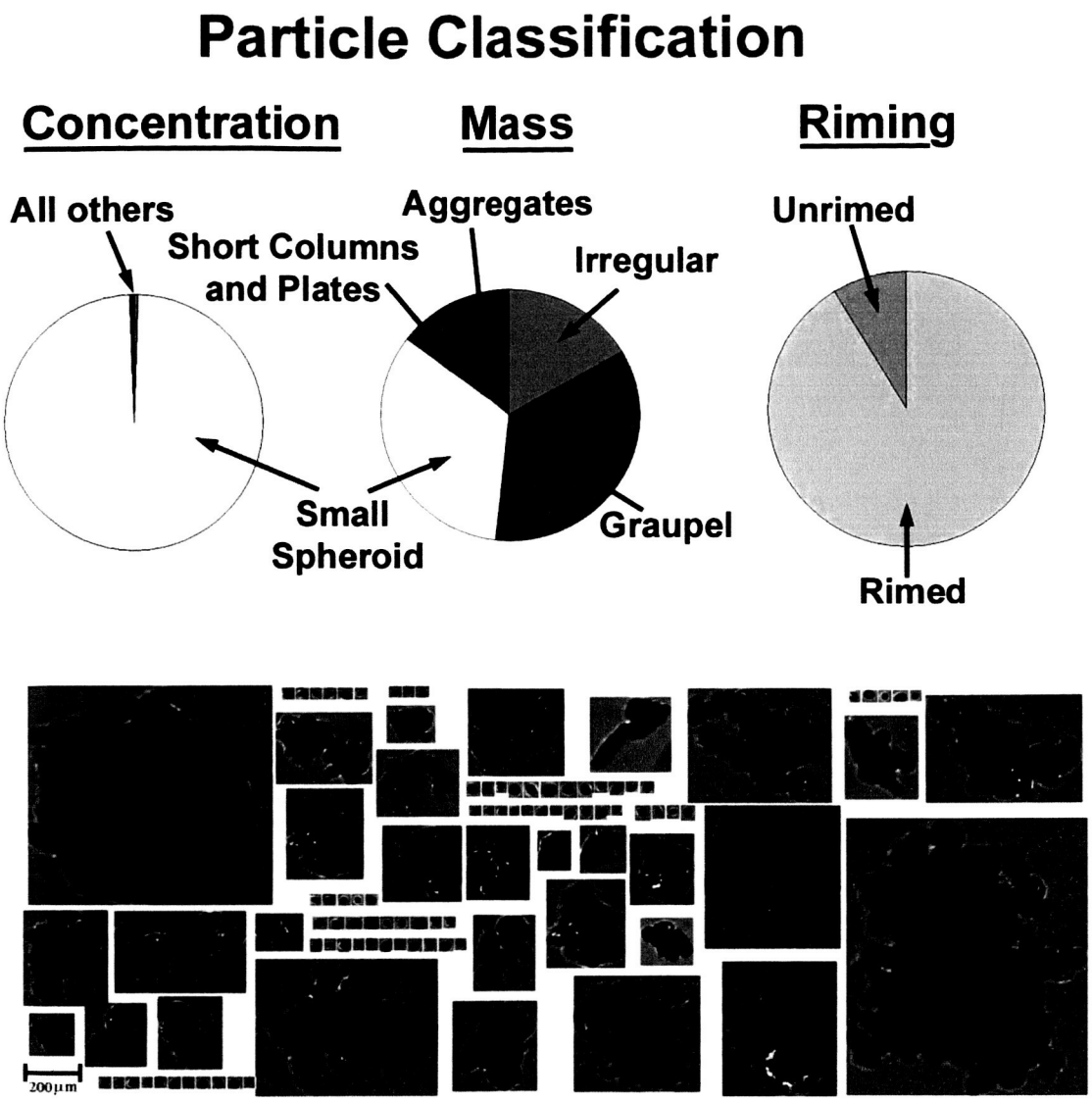

Figure 10. Examples of particles and classification percentages from the region also shown in **Figure 1.**

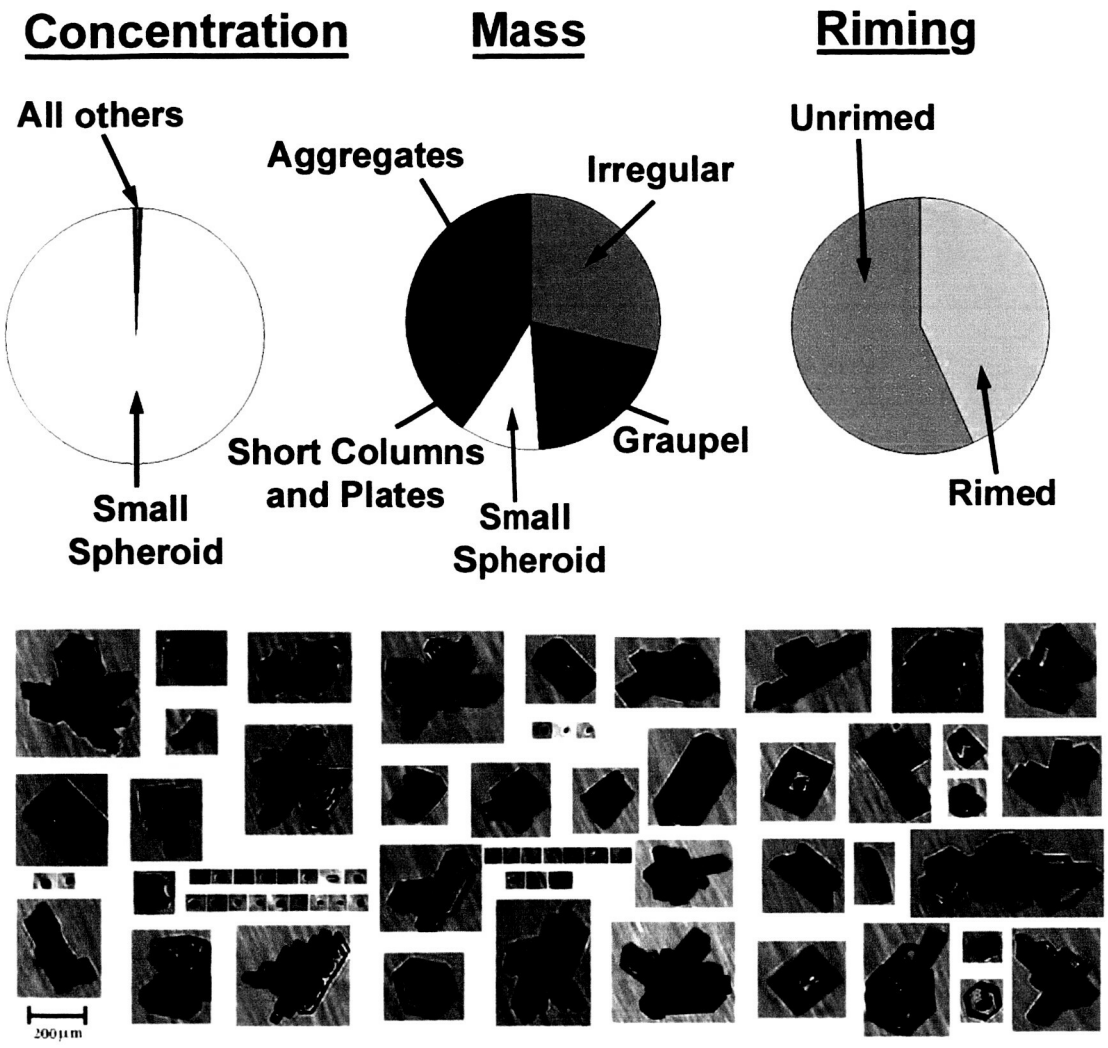

Figure 11. Examples of particles and classification percentages from the region also shown in **Figure 2.**

We also developed algorithms to automatically classify CPI images by particle type. The manual classification, used for **Figures 10** and **11** above, is educational, but the classification process is too labor intensive to be of practical

use. The ability to automatically classify particles by crystal habit improves calculations of ice water content, which aids investigators who are trying to improve remote retrieval algorithms. The particle types include columns, plates, rosettes, aggregates, graupel, irregulars, small ice spheroids and water drops. The methodology used in the development of the automatic particle classification algorithms centered around selecting an appropriate set of criteria based on particle features identified by the CPIview processing software. The CPIview code processes raw CPI data files and outputs particle images and derived parameters, and also outputs a particle statistics file in ASCII format. The particle statistics file creates a long list of characteristics for each particle that is imaged by the CPI. An example of the ASCII output describing a few particles is shown in **Table 1**. The complete list of particle statistics in **Table 1** is pared down in **Table 2**, which shows a list of particle features used to classify cirrus particles into plates, columns, rosettes, irregulars, and small ice spheroids.

CIRRUS PARTICLE CLASSIFICATION

The acceptance criteria used for habit classification in cirrus are shown below with a brief description of each. Common to all acceptance criteria is that they begin with 'focus gt 20', which means particles with focus values of 20 or less (out of a maximum value of ~100) are not considered.

Rosettes:
focus gt 20 and sqrt(area)/perim lt .1575 and not(len gt 2*wid and area gt .65*len*wid and cutoff lt 5) and crystal eq 15 and len gt 60

The second block in the criteria (sqrt(area)/perim lt .1575) is an area to perimeter ratio. The two dimensional projection of a rosette typically has a very large perimeter to area ratio. The third block in the criteria (len gt 2*wid and area gt .65*len*wid and cutoff lt 5) eliminates columns from the filter. Columns have similar area to perimeter ratios as rosettes, but different length to width ratios. The remainder of the criteria screens out very small particles that can occasionally get through the criteria.

Columns:
focus gt 20 and len gt 2*wid and area gt .65*len*wid and cutoff lt 5 and not(sqrt(area)/perim lt .1575)

The column acceptance criteria has some similarities to the rosette criteria, except for columns the length must be greater than twice the particles width. The third block in the criteria (area gt .65*len*wid and cutoff lt 5) verifies the particle is mostly filled. For example, a hair with an "S-turn" in it will pass the length to width test, but will not pass the area test. Cutoff particles are not accepted because an arm of a rosette could pass for a column. The final block in the column acceptance criteria eliminates "rosette-like" particles that may fall into the column category.

Table 1. Example of ASCII Output used for Classification; First Half of Variables.

mm:dd:hh:mm:ss	ROI #	ArrTime	TS	DeadTime	Length	Width	Dark	Area	Perim	Centroid	
8:13:23:42:51.512	0	511635	24	103.765	140.38	113.26	0	11331.18	508.03	34	35
8:13:23:42:51.727	0	727107	18	0	473	278.87	0	78440.12	1824.99	91	91
8:13:23:42:52. 77	0	77074	55	170.667	221.97	132.08	0	22106.91	726.07	37	53
8:13:23:42:52.342	0	342460	23	0	33.96	29.9	0	841.11	115.56	11	11
8:13:23:42:52.722	0	722380	5	0	179.64	155.48	0	18641.96	660.66	43	43
8:13:23:42:52.818	0	817952	20	0	205.78	192.78	0	26698.63	778.4	50	51
8:13:23:42:52.889	0	888591	24	0	246.63	147.65	0	27915.33	769.68	34	60
8:13:23:42:52.939	0	938812	18	0	317.63	149.94	0	32602.27	1044.41	46	68
8:13:23:42:53.100	0	99717	43	212.992	216.76	160.18	0	23815.58	800.21	42	55
8:13:23:42:53.154	0	153912	44	0	351.44	261.13	0	60374.77	1511.01	60	82
8:13:23:42:53.319	0	318918	135	0	268.94	167.58	0	28190.41	852.54	44	59
8:13:23:42:53.323	0	322555	40	0	31.28	24.77	0	587.19	98.12	10	9
8:13:23:42:53.401	0	400987	132	0	23.68	22.65	0	439.07	80.67	9	8
8:13:23:42:53.502	0	501852	75	0	249.47	174.03	0	30205.9	861.26	51	51
8:13:23:42:53.580	0	580034	70	0	31.28	26.22	0	682.41	106.84	11	11
8:13:23:42:53.709	0	708510	5	0	336.37	260.55	0	49657.23	1319.14	74	70
8:13:23:42:53.764	0	763673	35	0	242.1	152.91	0	29073.84	900.5	52	54
8:13:23:42:53.783	0	782744	14	0	164.59	143.01	0	17139.6	560.36	39	38
8:13:23:42:53.848	0	847909	12	0	211.11	145.46	0	23773.26	717.35	51	40
8:13:23:42:53.952	6	951608	28	0	182.22	104.74	0	11632.71	573.44	48	17
8:13:23:42:54. 82	0	81692	9	382.294	349.76	286.53	0	67225.32	1707.25	79	78
8:13:23:42:54.158	0	157982	14	0	25.71	22.65	0	486.68	85.04	9	10
8:13:23:42:54.220	0	220249	47	0	212.85	77.14	0	12389.18	547.28	48	14
8:13:23:42:54.324	0	323572	23	0	27.79	23.68	0	486.68	88.12	7	9
8:13:23:42:54.347	0	347051	83	0	29.9	22.65	0	534.29	89.4	9	8
8:13:23:42:54.500	0	500100	74	0	33.49	29.09	0	830.53	111.2	11	8
8:13:23:42:54.533	0	532854	48	0	305.15	271.93	0	49942.89	1245.01	64	65
8:13:23:42:54.597	0	596924	51	0	235.72	193.91	0	30518.01	955.92	45	55
8:13:23:42:54.626	0	626180	8	0	132.54	119.62	0	12071.78	468.79	32	32

Table 1 (continued) Example of ASCII Output used for Classification; Second Half of Variables

Rndness	X_mnt	Y_mnt	Rub_bnd	Fract_dim	SampPer	Focus	Fmin	Fmax	FStDv	Fgd	Cutoff	Crystal	P1
0.73	0	0	0	0	1	46	19	70	13.7	16	0	15	0
0.45	0	0	0	0	1	50	17	123	35.24	16	0	15	0
0.57	0	0	0	0	1	54	9	114	30.48	16	0	15	0
0.93	0	0	0	0	1	43	15	77	17.34	15	19	1	0
0.74	0	0	0	0	1	53	10	87	22.08	16	0	15	0
0.8	0	0	0	0	1	60	5	91	25.91	16	0	15	0
0.58	0	0	0	0	1	54	32	102	18.35	16	0	15	0
0.41	0	0	0	0	1	43	18	63	11.9	16	0	15	0
0.65	0	0	0	0	1	65	27	132	29.91	16	0	15	0
0.62	0	0	0	0	1	43	14	80	16.38	16	0	15	0
0.5	0	0	0	0	1	58	29	136	28.1	16	0	15	0
0.76	0	0	0	0	1	36	14	63	14.29	16	0	1	0
1	0	0	0	0	1	51	3	113	36.32	16	0	1	0
0.62	0	0	0	0	1	23	4	50	14.04	16	2	15	0
0.89	0	0	0	0	1	59	26	100	24.98	16	0	1	0
0.56	0	0	0	0	1	50	1	95	22.87	16	0	15	0
0.63	0	0	0	0	1	43	20	80	18.93	16	1	15	0
0.81	0	0	0	0	1	53	21	108	23.42	13	20	15	0
0.68	0	0	0	0	1	68	33	131	26.16	16	0	15	0
0.45	0	0	0	0	1	41	2	109	29.32	16	23	15	0
0.7	0	0	0	0	1	40	13	80	14.17	16	0	15	0
0.94	0	0	0	0	1	50	20	90	26.56	16	0	1	0
0.35	0	0	0	0	1	32	0	74	22.93	16	35	15	0
0.8	0	0	0	0	1	28	0	83	21.9	16	2	1	0
0.76	0	0	0	0	1	32	2	88	24.92	16	0	1	0
0.94	0	0	0	0	1	34	5	62	18.01	16	0	1	0
0.68	0	0	0	0	1	51	23	90	18.57	16	1	15	0
0.7	0	0	0	0	1	68	27	155	30.24	16	1	15	0
0.87	0	0	0	0	1	50	14	115	23.43	16	0	15	0

Table 2. List of Particle Features Used to Classify Both Cirrus and Anvil Particles

Focus	Value for relative focus of the particle (0 to ~100).
Len	Length of particle.
Wid	Width of particle.
Area	The imaged area of the particle.
Cutoff	The percent of the particle found along the edge of the cutout image.
Perim	The perimeter of the particle.
h2,h3,. . .	2^{nd}, and 3^{rd}, etc. Harmonics of the Fourier transform of a series of particle radii
Hole area	Percentage of the area of the particle which is significantly brighter than the rest. (i.e., transparent regions in the particle.)
Crystal	Computer classification of particle shape. 1 = spheroidal, 15 = non-spheroidal.

Plates:
focus gt 20 and ((h2 gt 0.01 and h3 lt 0.02 and h5 lt 0.02 and h6 gt 0.01 and len lt 1.8*wid and len gt 75 and h4 lt 0.02) or (len gt 75 and h2 gt 0.01 and len lt 1.8*wid and ((h4 gt 0.01) or (h6 gt 0.01)) and h3 lt 0.02 and hole area gt 10))

The acceptance criteria for plates use radial harmonics calculated by the CPIview extractor software. This criteria has two distinct parts. The first is a relatively rigid criterion that works only with harmonics to identify hexagonal shaped particles. The second part (after the 'or') allows less hexagonal looking particles through but demands that there be a light colored spot (hole) in the particle. This identifies more pristine crystals that aren't necessarily imaged face on.

Spheroidal:
focus gt 20 and (crystal eq 1 and not(len gt 2*wid and area gt .65*len*wid and cutoff lt 5) and not(len gt 2*wid and area gt .65*len*wid and cutoff lt 5))

Spheroidal particles are identified by roundness (e.g. crystal eq 1 when a particle is round). The remainder of the criteria simply eliminates stray shapes from being accepted.

Irregular:

The particles not identified by one of the above criteria are classified as irregular.

Figure 12 shows an example of the results using the automatic classification algorithm on a set of CPI images collected in a cirrus cloud, compared with a manual classification of the same particles. The sampled cloud was located over the ARM/CART site on 1 March 2000 from 23:00:00 to 23:05:00 GMT. Visual inspection of the pie charts indicates the automatic algorithm performs well on particles imaged in cirrus clouds. It produced only very small differences in classification of columns, irregular, plates and rosettes. **Figure 13** shows a logarithmic bar graph of the actual number of imaged particles place in each category by both classification techniques. The raw numbers are placed above each bar. The Automatic method classified approximately 2.3% more rosettes, taking 0.3% from the manually classified columns and 2.0% from irregulars.

Figure 14a, b, and c provide randomly selected examples of the particles imaged in the cirrus cloud. Next to (or below) each image are the classifications resulting from both the automatic and manual methods. For easier identification, particles classified "differently" have a yellow box around them.

Several of the "differently" categorized particles are cut-off images (i.e. particles imaged at 23:1:57:141 in **Figure 14a** and 23:2:25:262 in **Figure 14c**). It may be appropriate to remove these particles from analysis by constraining the Cutoff criteria even further. However, doing so would reduce the images particle statistics and may bias the habit classification in other ways. Another possibility is to continue developing neural network technology to aid in identification of these difficult to classify particles considering most differences appear to be the result of subjective interpretation by the person performing the manual classification versus objective interpretation by the automated method.

ANVIL PARTICLE CLASSIFICATION

The following are the particle acceptance criteria commonly used for anvil clouds. **Table 2** provides an explanation of the variables used in these criteria. The column, plate and spheroidal acceptance criteria are the same as is used for cirrus clouds.

Columns:

focus gt 20 and len gt 2*wid and area gt .65*len*wid and cutoff lt 5 and not(sqrt(area)/perim lt .1575)

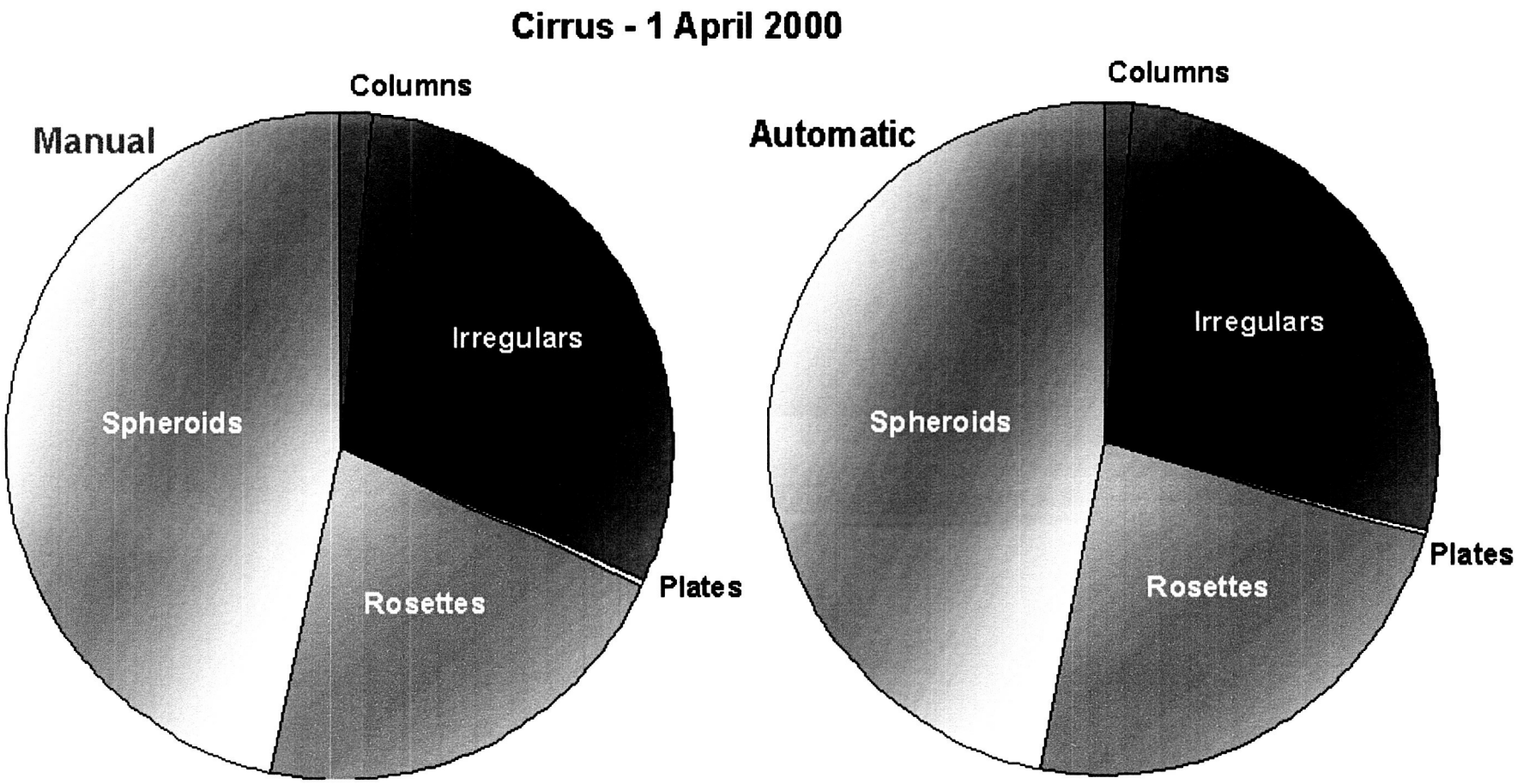

Figure 12. Pie Chart depicting fraction of imaged particles within each category for both manual (left) and automatic (right) classification methods.

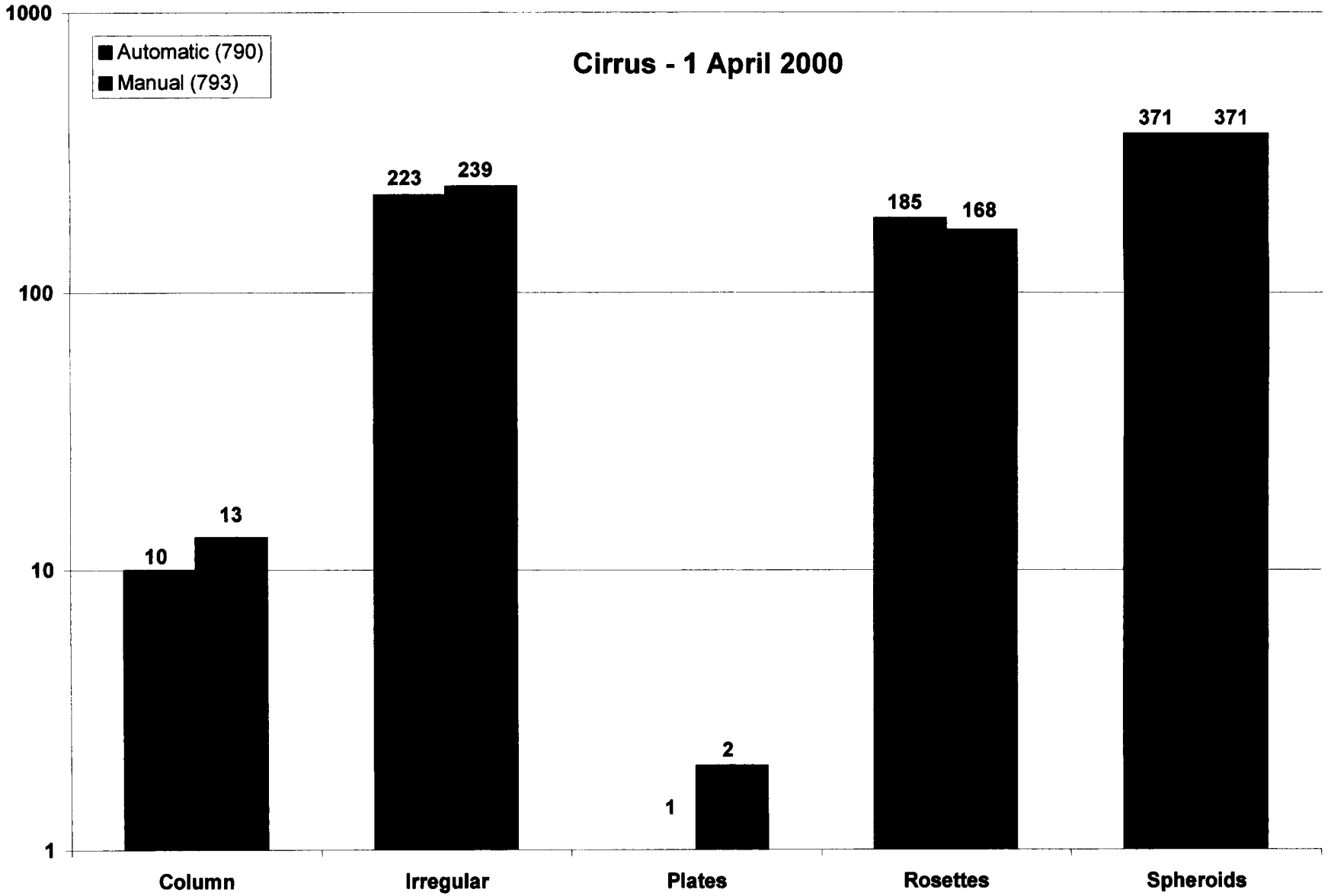

Figure 13. Bar Graph indicating actual number of particles classified by automatic (purple) and manual (green) categorization. Numbers above bars indicates total number represented by bar. Total number of identified particles provided in parenthesis in legend.

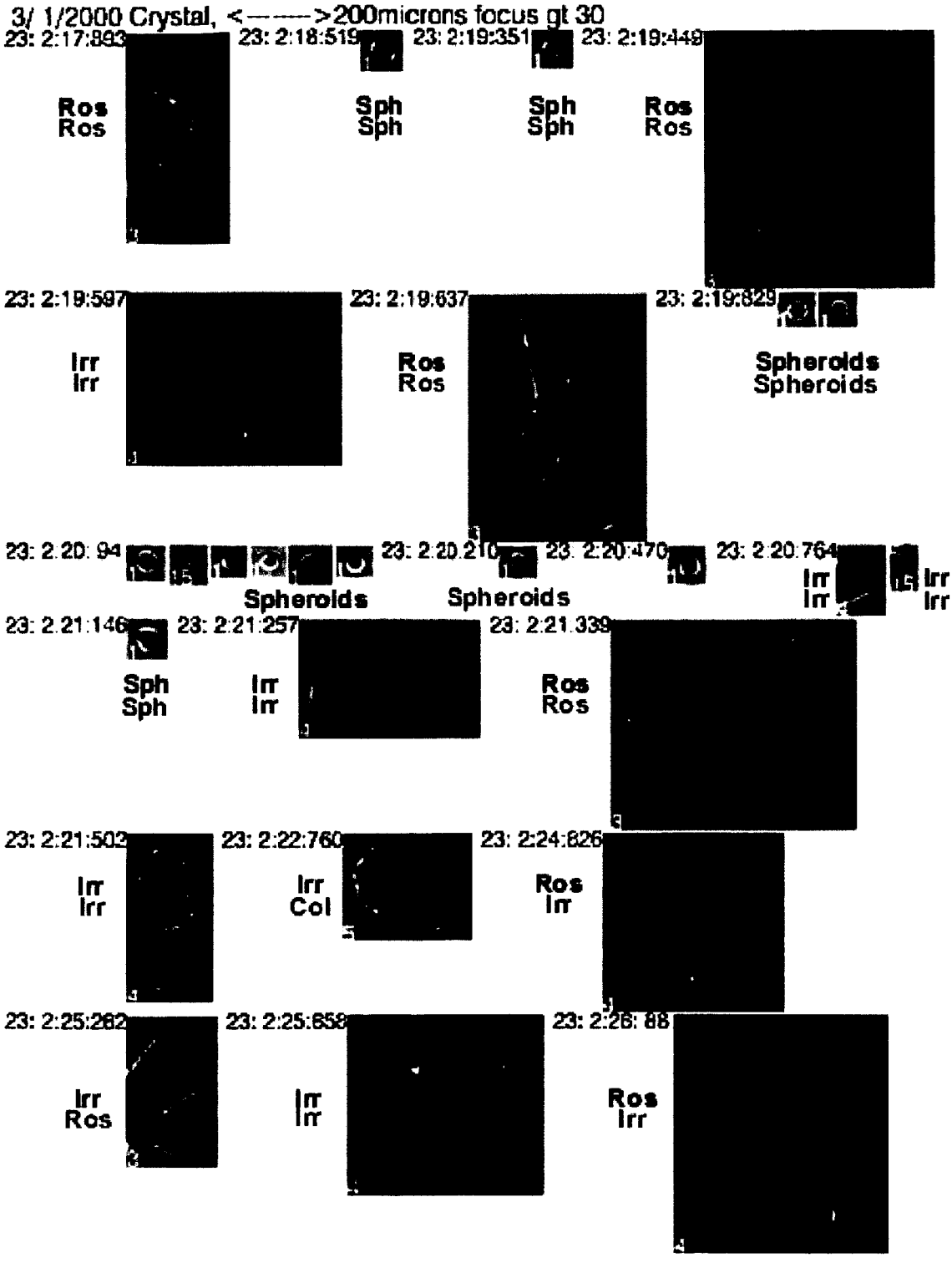

Figure 14a. Example of images with automatic (purple) and manual (green) classifications indicated to the left or directly below particles. Particles with differing classifications are highlighted in yellow.

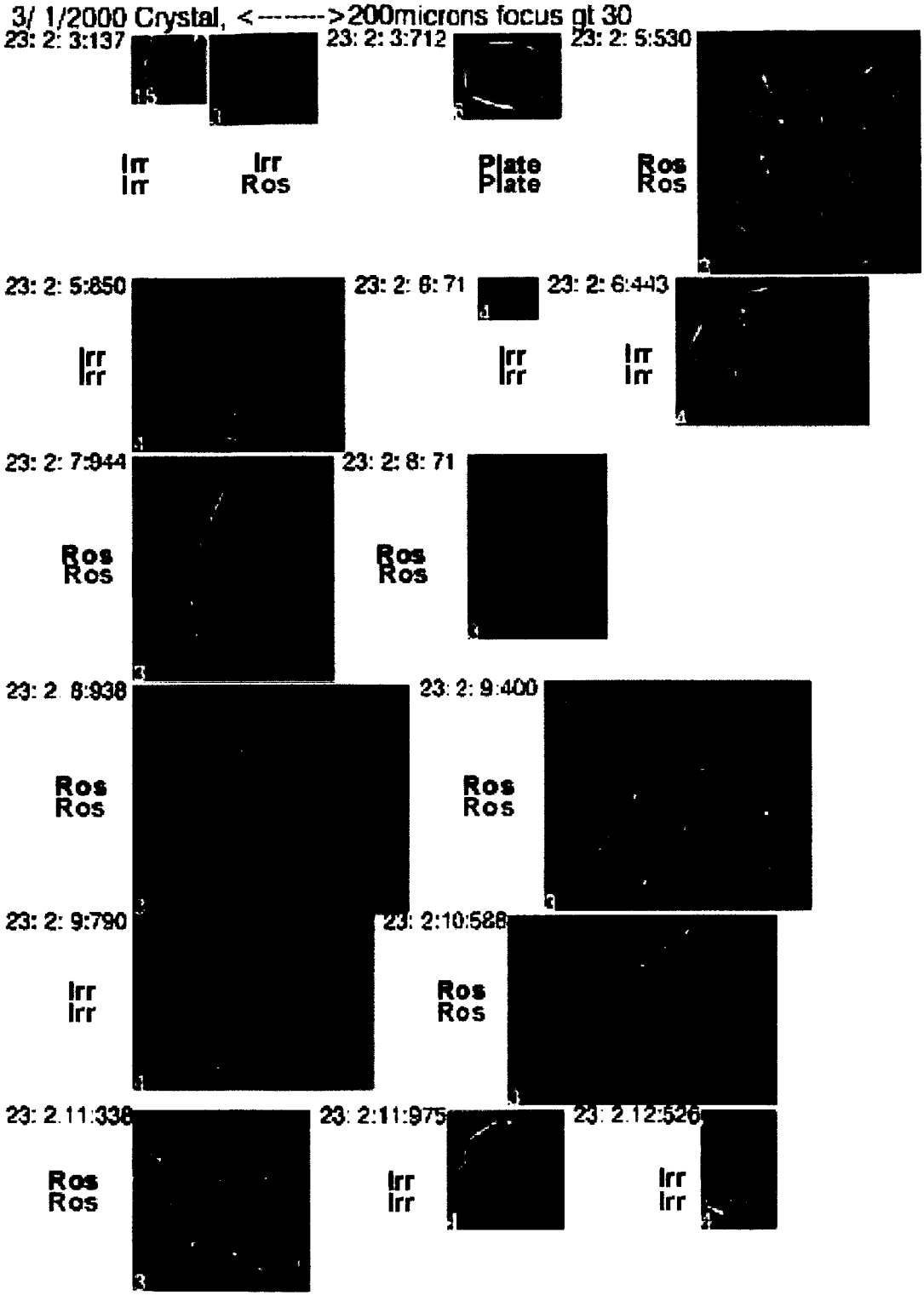

Figure 14b. Example of images with automatic (purple) and manual (green) classifications indicated to the left or directly below particles. Particles with differing classifications are highlighted in yellow.

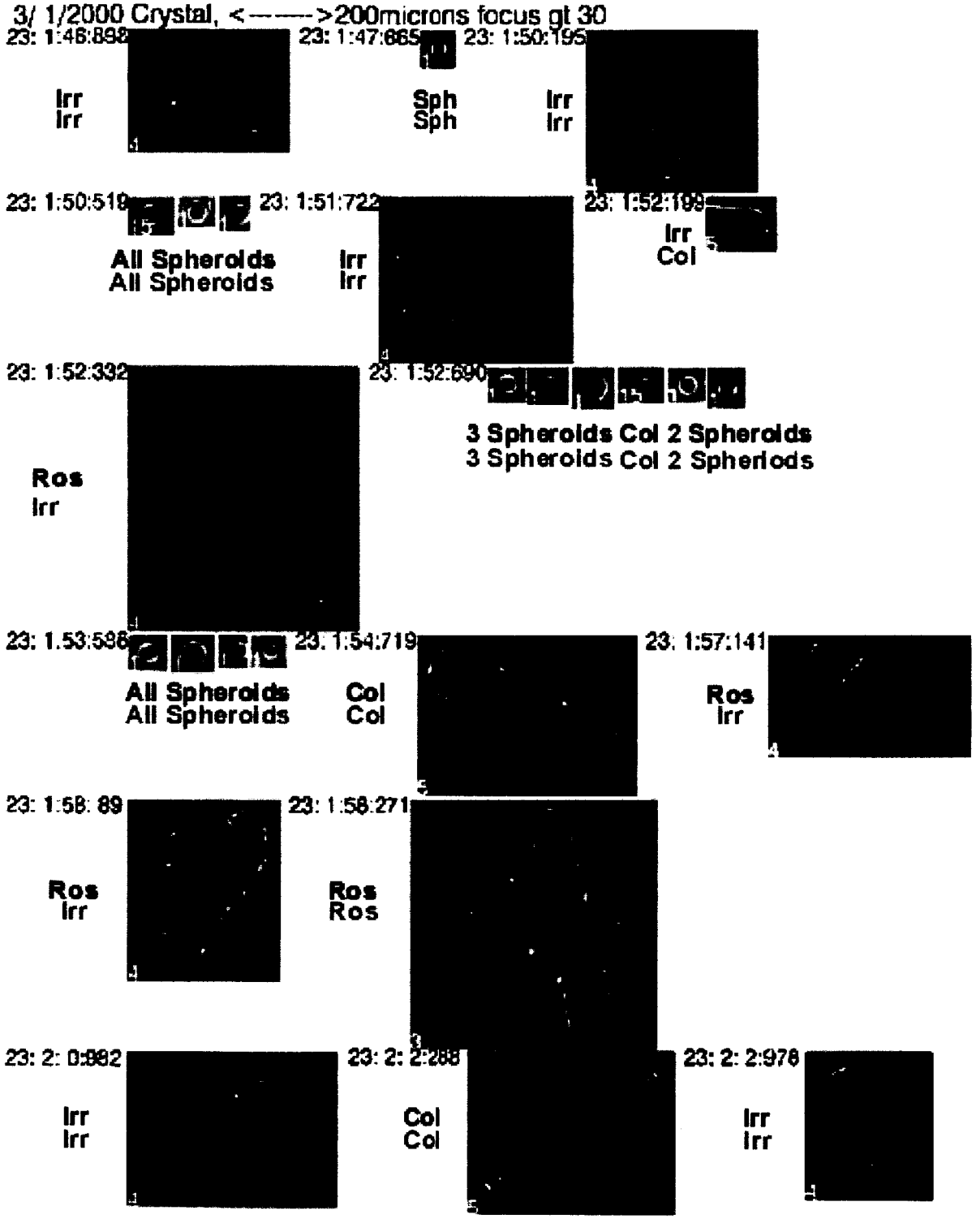

Figure 14c. Example of images with automatic (purple) and manual (green) classifications indicated to the left or directly below particles. Particles with differing classifications are highlighted in yellow.

Plates:
focus gt 20 and ((h2 gt 0.01 and h3 lt 0.02 and h5 lt 0.02 and h6 gt 0.01 and len lt 1.8*wid and len gt 75 and h4 lt 0.02) or (len gt 75 and h2 gt 0.01 and len lt 1.8*wid and ((h4 gt 0.01) or (h6 gt 0.01)) and h3 lt 0.02 and hole area gt 10))

Spheroidal:
focus gt 20 and (crystal eq 1 and not(len gt 2*wid and area gt .65*len*wid and cutoff lt 5) and not(len gt 2*wid and area gt .65*len*wid and cutoff lt 5))

Aggregate:
focus gt 20 and sqrt(area)/perim lt .175 and not(len gt 2*wid and area gt .65*len*wid and cutoff lt 5) and crystal eq 15 and len gt 60

The acceptance criteria for aggregates are similar to the rosette acceptance criteria. The sqrt(area)/perim ratio is increased to allow the acceptance of chains and clusters of particles that are less spindly than rosettes.

Graupel:
focus gt 20 and len gt 600 and wid gt 600

In anvil clouds, particles imaged by the CPI that have large lengths and widths are graupel particles

Irregular:
The particles not identified by one of the above criteria are classified as irregular.

Figure 15 shows an example of the results using the automatic classification algorithm on a set of CPI images collected in an anvil cloud during TRMM TEFLUN-B, compared with a manual classification of the same particles. The cloud was sampled on 13 August 1998 from 23:42:45 to 23:43:45. Visual inspection of the pie charts indicates that the automatic algorithm produced larger differences in classification of all particles than in the cirrus cloud. More complex particle shapes, including riming, are responsible for these increased differences. **Figure 16** shows a logarithmic bar graph of the actual number of imaged particles place in each category by both classification techniques. The raw numbers are placed above each bar and the total number of particles identified by each classification method are in parenthesis in the key. Comparison of the number of particles identified by both methods indicates the Automatic method classified approximately 6.4% more irregulars, 3.7% more aggregates, 1.1% less columns, 2.1% less plates, and 6.9% less spheroids.

Figure 17a, b, and c provide randomly selected examples of the particles imaged in the TEFLUN-B anvil cloud. Next to (or below) each image are the classifications resulting from both the manual and automatic methods. Particles classified "differently" have a yellow box around them.

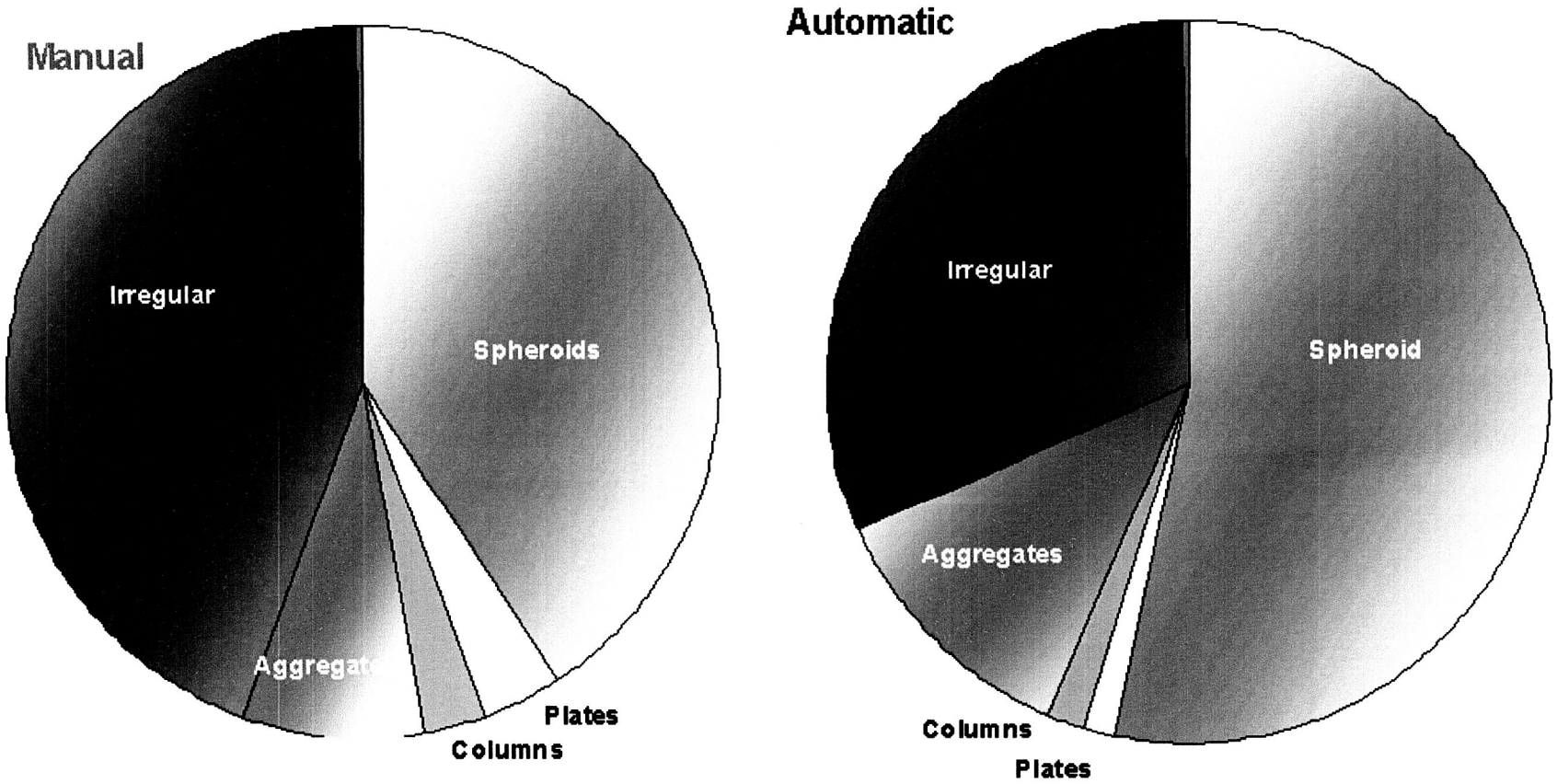

Figure15. Pie charts indicating fraction of imaged particles in each category for both manual (left) and automatic (right) classification methods.

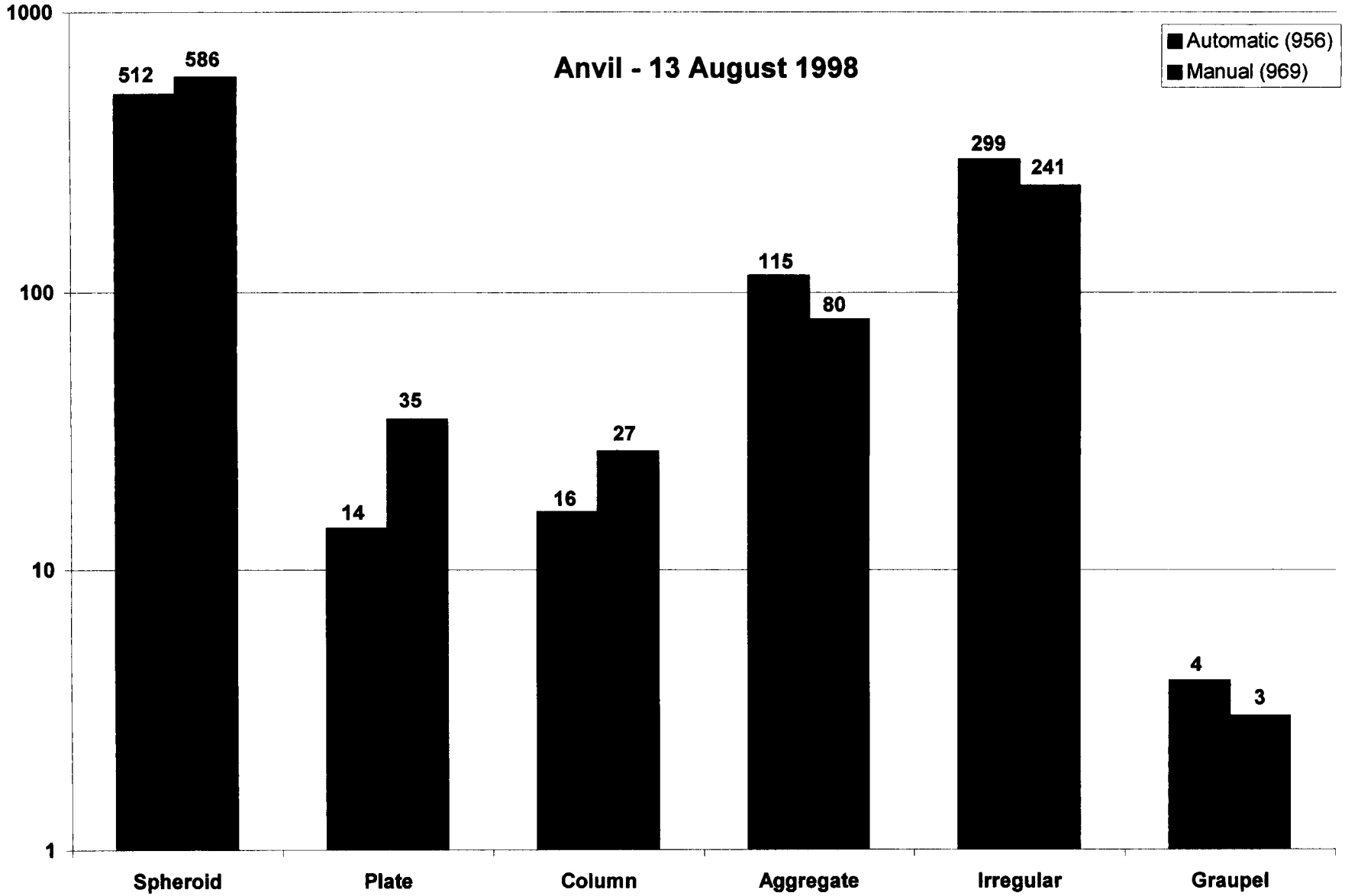

Figure 16. Bar Graph indicating actual number of particles classified by automatic (purple) and manual (green) categorization. Numbers above bars indicates total number represented by bar. Total number of identified particles provided in parenthesis in legend.

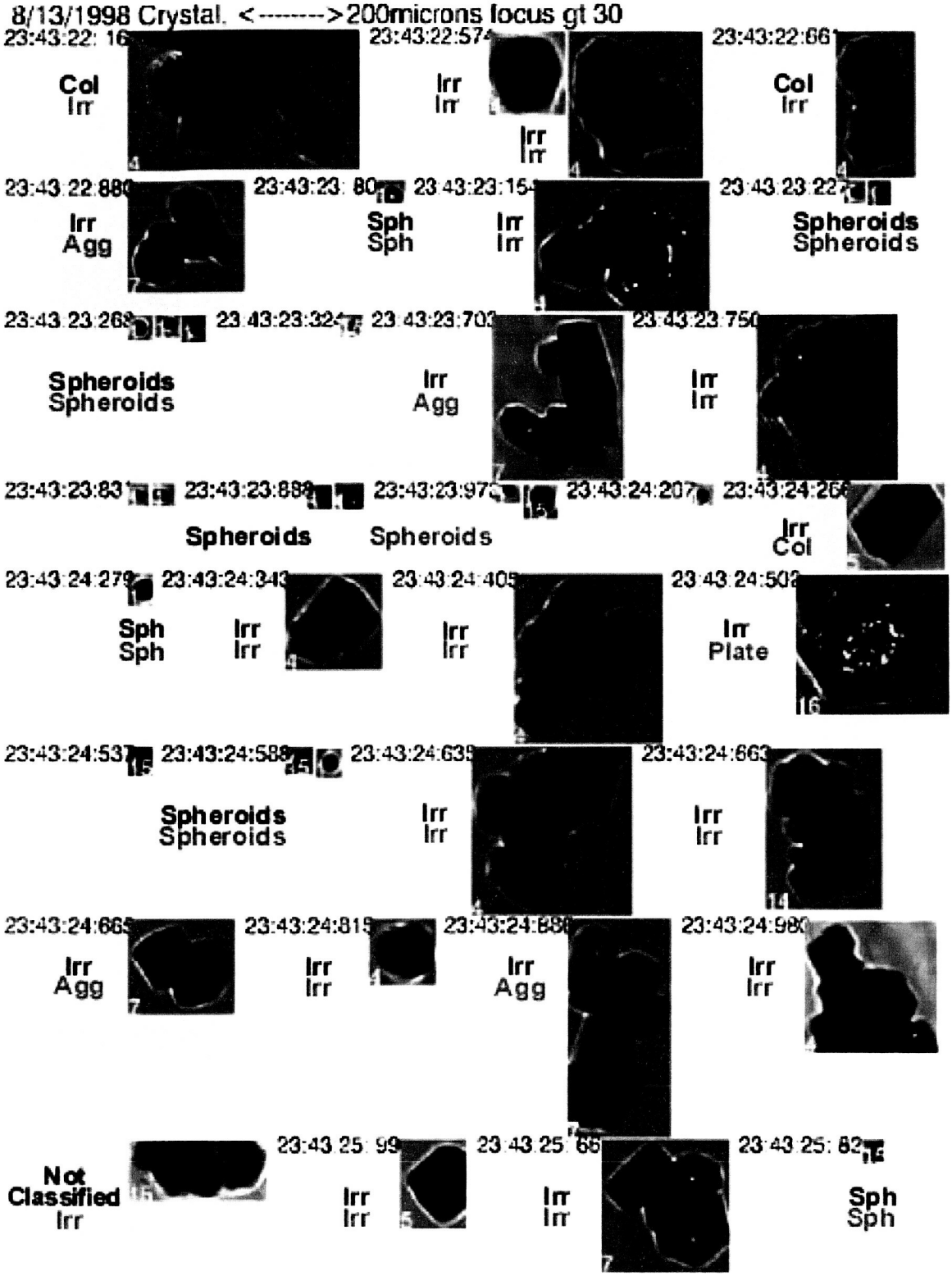

Figure 17a. Example of images with automatic (purple) and manual (green) classifications indicated to the left or directly below particles. Particles with differing classifications are highlighted in yellow.

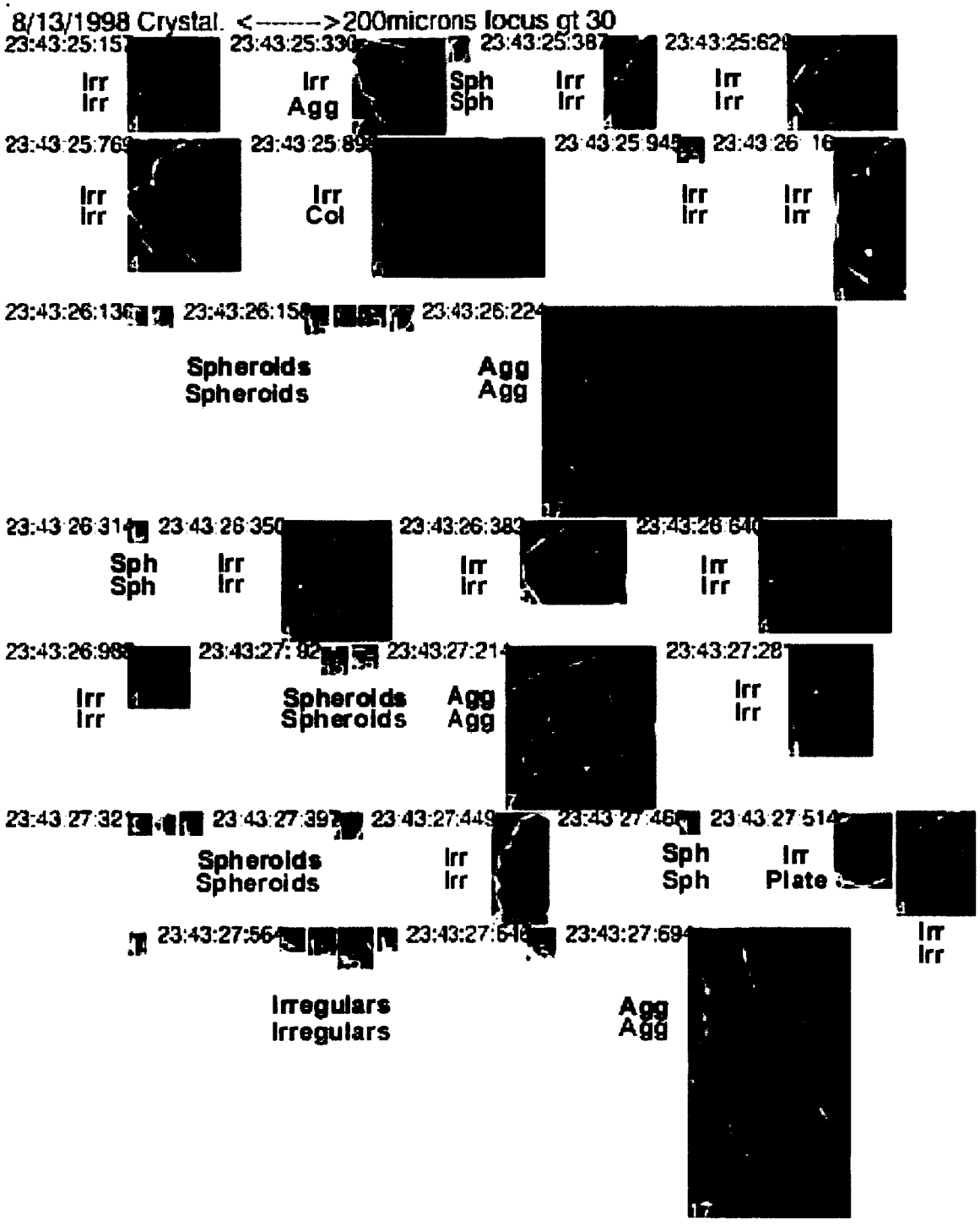

Figure 17b. Example of images with automatic (purple) and manual (green) classifications indicated to the left or directly below particles. Particles with differing classifications are highlighted in yellow.

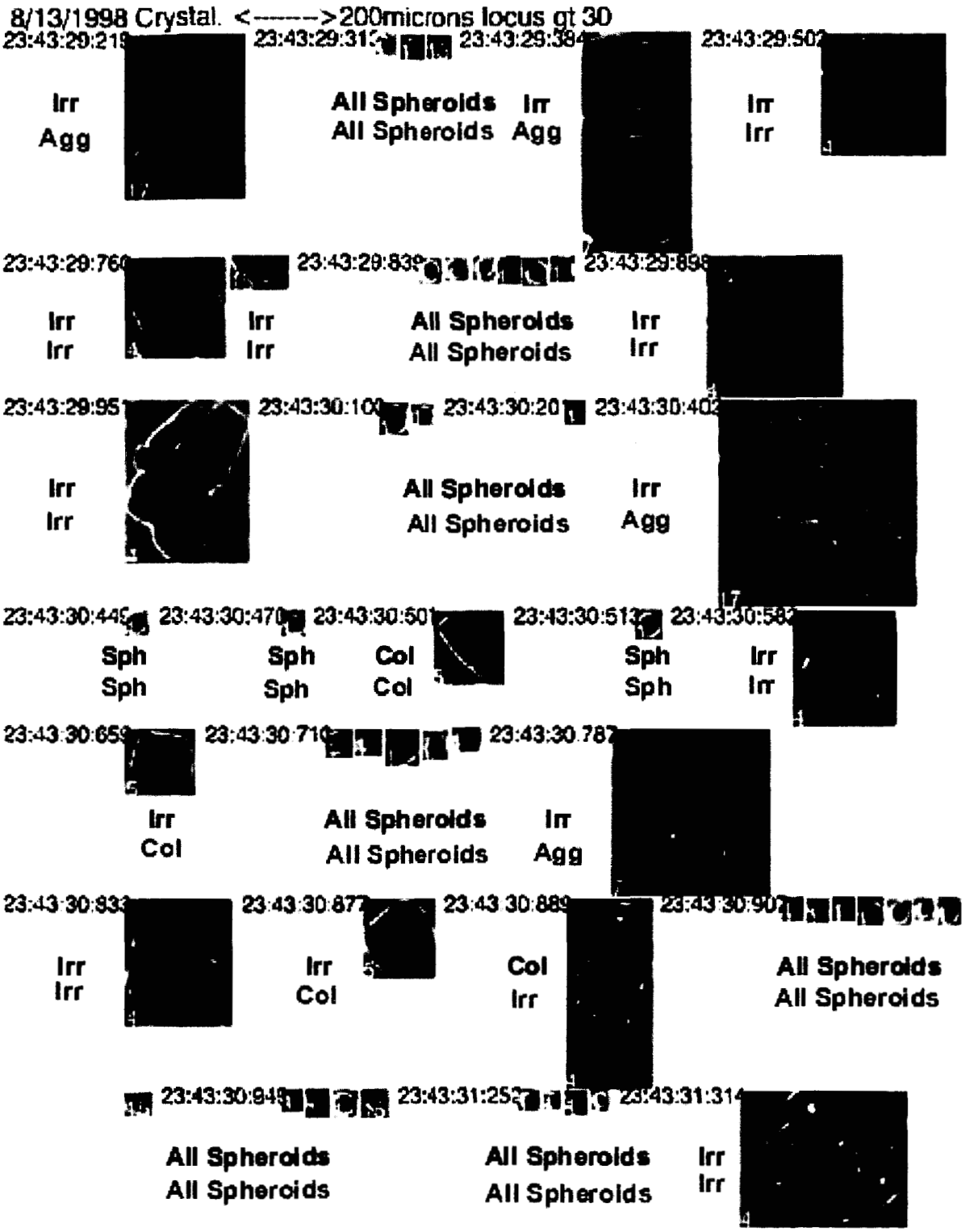

Figure 17c. Example of images with automatic (purple) and manual (green) classifications indicated to the left or directly below particles. Particles with differing classifications are highlighted in yellow

Differences are once again related to subjective interpretation of the particle habit by the manual classifier. In the examples provided, many of the automatically classified irregular particles were designated as either aggregates or columns by the manual interpretation. For example, four short column particles identified as irregular by the automatic method were classified as columns by subjective manual interpretation (23:43:24:266 in **Figure 17a**, 23:43:25:898 in **Figure 17b**, 23:43:30:659 and 23:43:30:887 in **Figure 17c**). A new category of short column will be developed to capture this ambiguity and should be reasonable to achieve through the use of length-to-width aspect ratio, perimeter, and harmonics previously defined in **Table 2**.

Riming of particles makes it difficult for the automatic method to determine the habit of many elongate particles. For example, the hex plate imaged at 23:34:24:502 (**Figure 17b**) was automatically classified as an irregular, however, to the human observer it is very obviously a plate with some light riming on the edge. A moderately rimed aggregate imaged at 23:43:30:402 (**Figure 17c**) was similarly incorrectly identified by the automatic method. Algorithms for automatic identification of rimed versus unrimed particles will also be developed and should serve to solve some of the current classification discrepancies.

1.5.2 Testing the habit classification scheme specific to TRMM CMPD

We report above results of work on habit classification schemes for cirrus cloud and thunderstorm anvil. For the software that processes data for the CMPs we will use only one scheme for all cloud types. In general this is a greater challenge. However because only a limited size of CPI data was classified and because the Common Microphysical Product Definition (CMPD) specifies fewer classes, the task is actually less difficult. In the following we report on the simple classification scheme incorporated in the CMP CPI processing software and on the results of applying it to a priority leg from the University of Washington's Convair aircraft flown in KWAJEX.

Only particles between 40 and 150 microns are to be classified from the CPI according to the CMPD. For the area PSD, particles between 1600 and 22500 microns squared are to be classified. The classes are spheres (liquid water), long and skinny particles (columns and needles), graupel, aggregates, and small indeterminate (particles covering less than 25 pixels). Graupel and aggregate particles are the most difficult of this group to classify but there are so few expected in the 40 – 150 micron size range that we are not classifying these particle types for the CMPs. At 2.3 micron resolution there are essentially no particles larger than 40 microns which contain less than 25 pixels. This classification is straightforward anyway. Our CPIVIEW software calculates particle area, which is simply proportional to the number of pixels.

Water is classified according to the following criteria. The first condition is that

$$\frac{area}{\pi L^2} > 0.75$$

where L is the particle's maximum dimension. The term $area/\pi L^2$ is called roundness. Then, if the standard deviation of the radii is less than 2 pixels and/or the maximum deviation of the radii is less than or equal to 10% of the mean radius, the particle is classified as water.

Long and skinny particles are classified according the following criteria. First the maximum dimension must be at least 3 times the transverse dimension. This simply insures that the particle is long and skinny. Then the perimeter to area ratio is compared to a pseudo perimeter to area ratio for an ideal column.

$$\frac{perimeter}{area} < 6 \times \frac{len + wid}{len \times wid}$$

This removes particles with highly convoluted perimeters that happen to be long and skinny.

We now show the results of applying these criteria to the University of Washington's Convair data that were used for testing our CPI processing code. The leg was flown at an approximately constant altitude of 6300 feet msl. The temperature was about –6 C and the liquid water content averaged a few tenths gram per meter cubed. The cloud was mixed phase and one can suspect that the Hallett-Mossop ice multiplication mechanism was in play. The aircraft flight track superimposed on a radar image is shown in **Figure 18**.

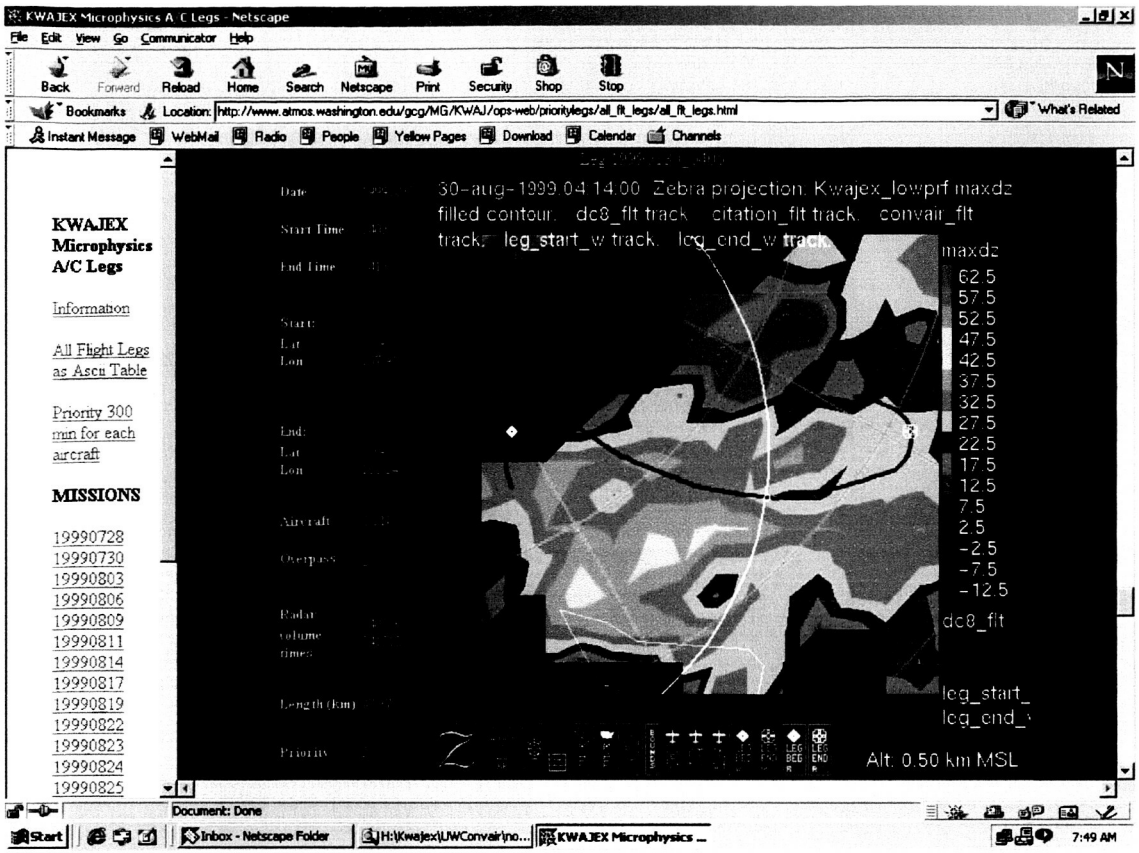

Figure 18: Radar image with University of Washington's Convair flight track superimposed, for the TRMM priority leg 19990830040456_kwajex_convair_57.

The Convair passed nearby, through, or under moderately strong cumulus cells. **Figure 18** shows a random sample of particles that were classified as long and skinny (columns and needles) and also were in the area range 1600 – 22500 square microns. **Figure 19** shows a random sample of those classified as spheres while **Figure 20** shows a random sample of particles not classified as either long and skinny, or spheres. Literally all of the hundreds of particles classified as long and skinny would also be so classified by eye. Of those classified as spheres, most of the larger particles would also be classified as spheres by eye. Many small particles classified as spheres would not be classified as spheres by eye or would not be considered classifiable by eye. When particles are too small and out of focus, it can be impossible to tell whether they are spherical. However the error can go both ways, small spheres by eye can be classified as ice by the automatic criteria. Thus some cancellation of errors occurs when only

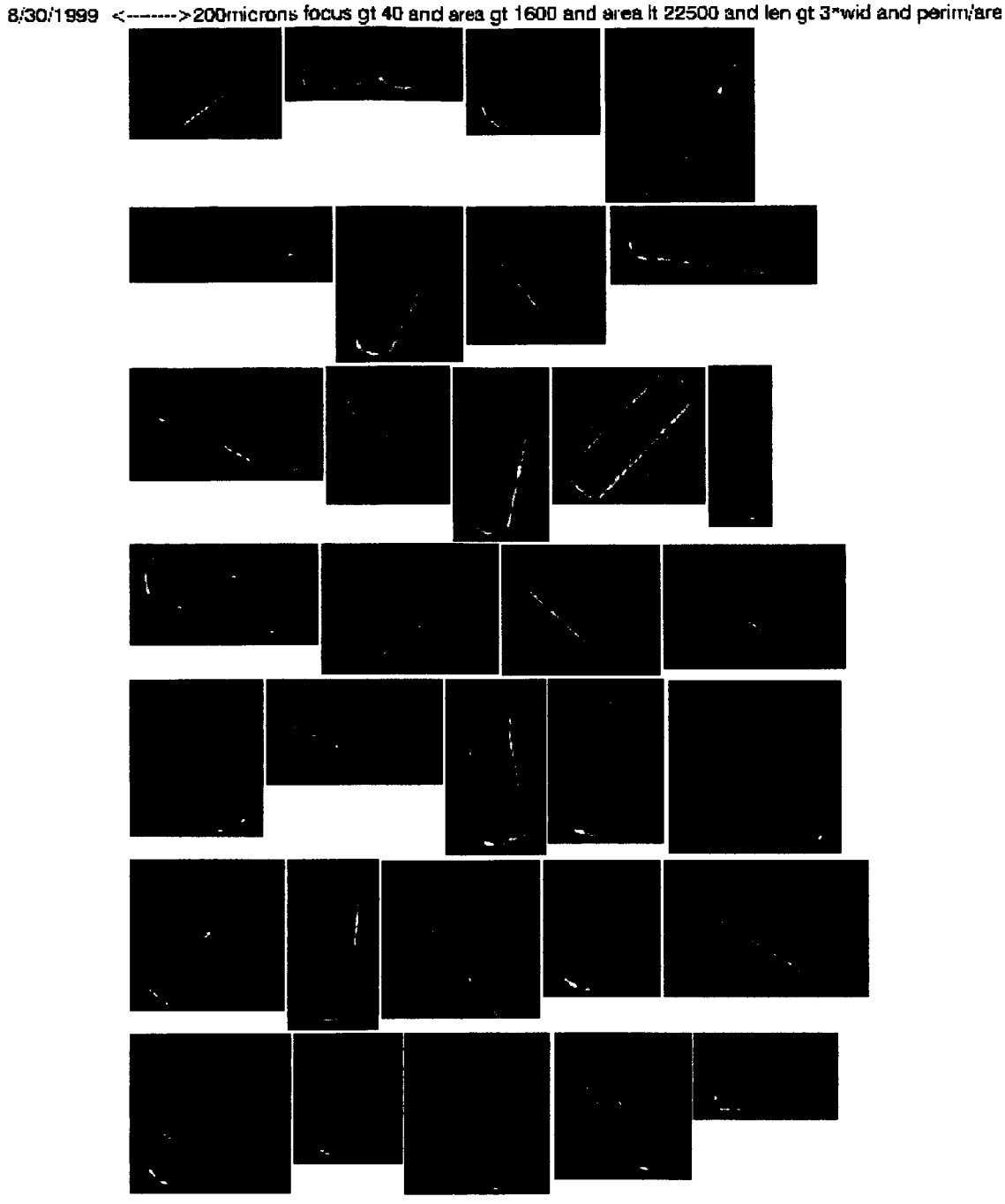

Figure 19: Examples of particles classified as long and skinny (columns and needles) by the simple criteria described in the text.

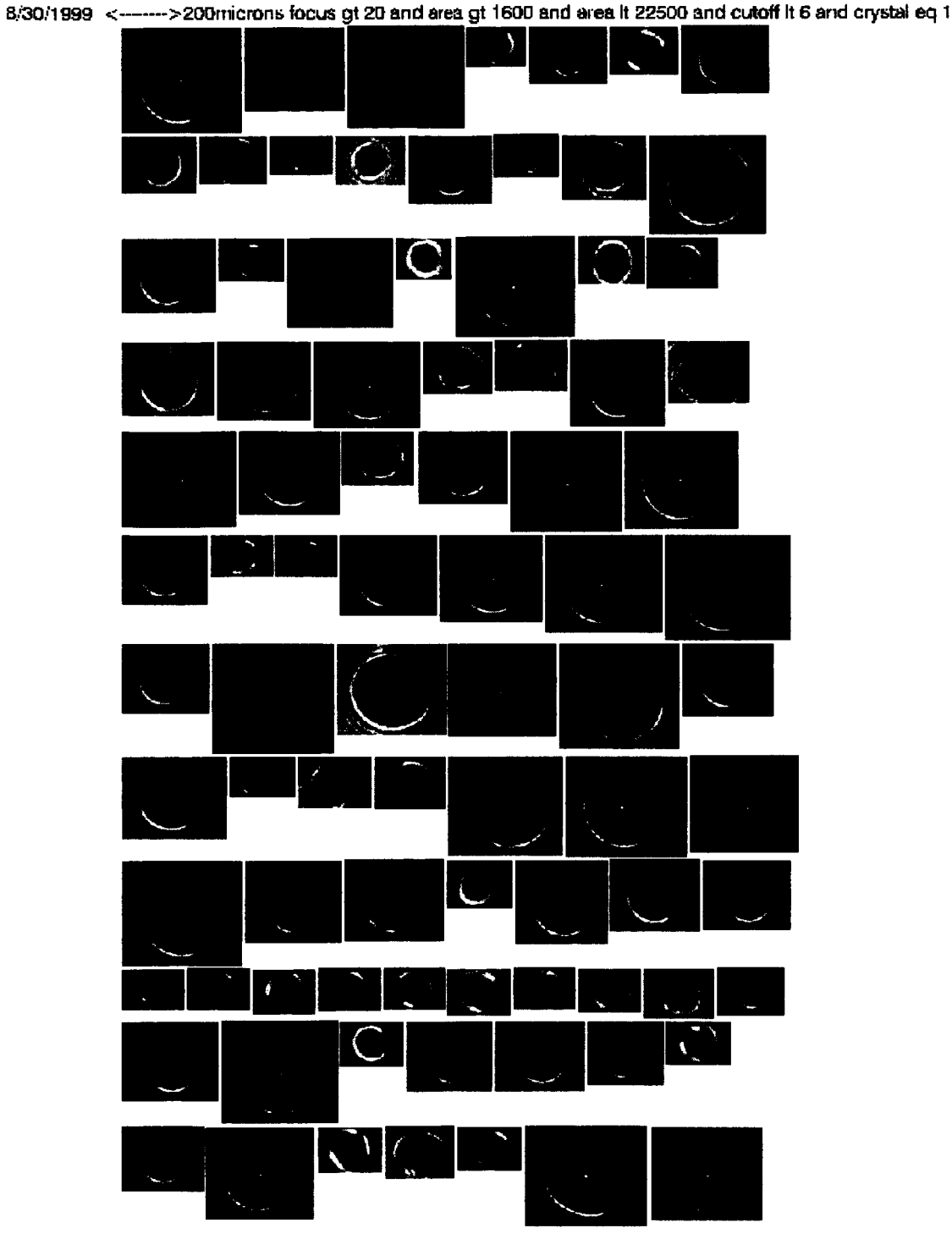

Figure 20: Examples of particles classified as spheres by the simple criteria described in the text.

Figure 21: Examples of particles not classified as long and skinny (columns and needles) or as spheres by the simple criteria described in the text.

percentages are considered. Finally we see in **Figure 21** that many particles that are not spheres or long and skinny are classified correctly. However some spherical particles and nearly spherical particles are also grouped with these. The very spherical looking particle near the center of the third row was classified

as non spherical because subtle gradients near the top edge caused the perimeter to be drawn in a jagged way. Fortunately this error is rare. Some of the nearly spherical drizzle particles are interesting. It can be seen by eye that they are frozen and are in various stages of growing facetted crystals by vapor deposition. It is a bit surprising that some of these were correctly classified by the simple criteria used. There are also particles that would easily be classified as columns in the sense of classical habits but were not classified as long and skinny by the simple criteria. They simply are not long and skinny enough. An arbitrary boundary must be set. Overall, we find the results of the criteria used quite satisfactory for this particular data set. We are still waiting for data from other groups to test the software before delivery and to see how these same criteria perform on those data sets.

1.6 Statistical Analysis of Ice and Water PSDs

Software was developed to compute mean particle size distributions and weight the PSDs by number, area, and mass. As shown in **Figure 22**, the variation from the mean gives an indication of the variability from cloud to cloud and region to region. This information is useful in validating both remote retrievals and cloud simulation models.

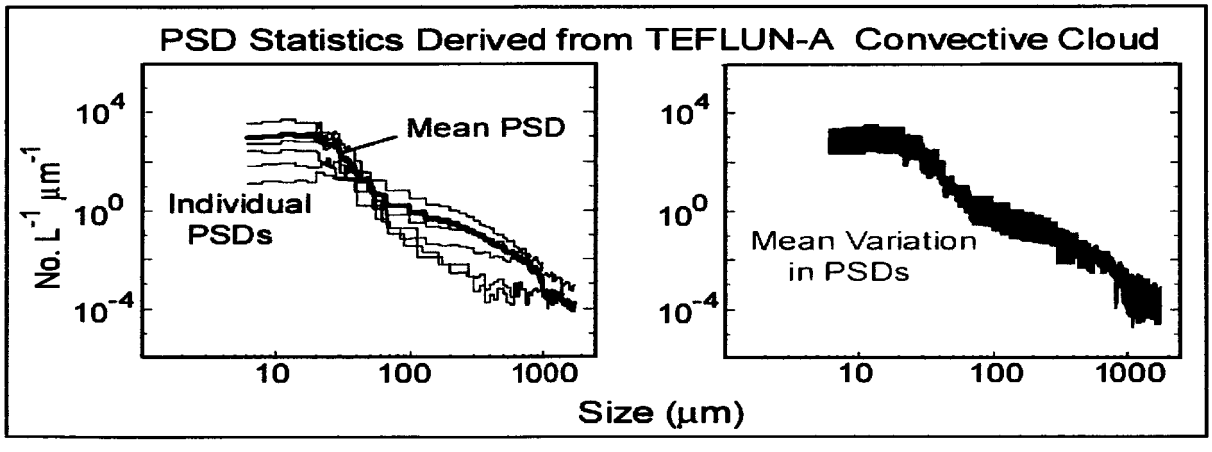

Figure 22. Example of particle size distributions (PSDs) collected from 192015 to 192145 on 18 April 1998 by the SPEC Learjet in a convective cloud investigated in TEFLUN-A. The panel at the left shows 5 contiguous PSDs and their mean; the panel at the right shows the mean PSD and a statistical computation of variability from the mean.

The CMP contains a very rigid data format. For example, all of the data are averaged over 1 Km, however, sometimes there are too few particles to produce statistically-significant averages over 1 Km. Another restriction occurs because the CPI data are only used in the size range from 40 to 150 μm while the 2D-C data are used in the size region up to several hundreds of microns. However, the 2D-C cannot reliably separate ice and water drops until the images achieve a size of at least 250 μm (and often larger), so drizzle-sized drops are often improperly classified in the CMP. **Figure 23** shows an example of CPI images of supercooled drops out to diameters of 200 μm in a convective cloud region investigated by the University of Washington Convair during Kwajex. This is a example where the CMP does not properly classify the 2D-C images, and in fact, parts of the convective region are classified as containing no supercooled liquid water. The particle size distributions shown in **Figure 23** have been properly separated into ice and water using CPI data. For comparison, **Figure 24** shows a stratiform cloud region that was separated by about 10 km from the convective region that does not contain supercooled drizzle. The light-scattering properties of ice particles and water drops are significantly different, *Z-R* relationships and TMI retrievals derived from these data will contain unnecessary errors.

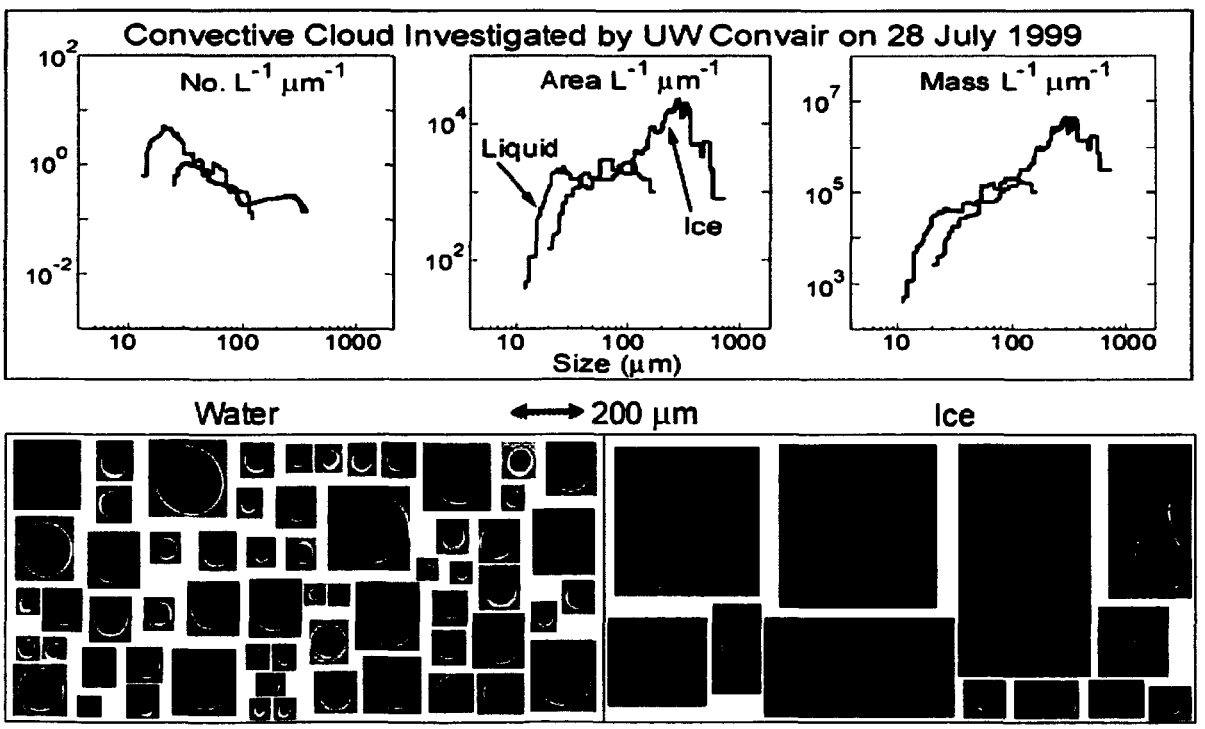

Figure 23. Example showing CPI derived water and ice particle size distributions and images in a convective cloud region (083320 - 083448) investigated at -°6 C by the UW Convair during Kwajex.

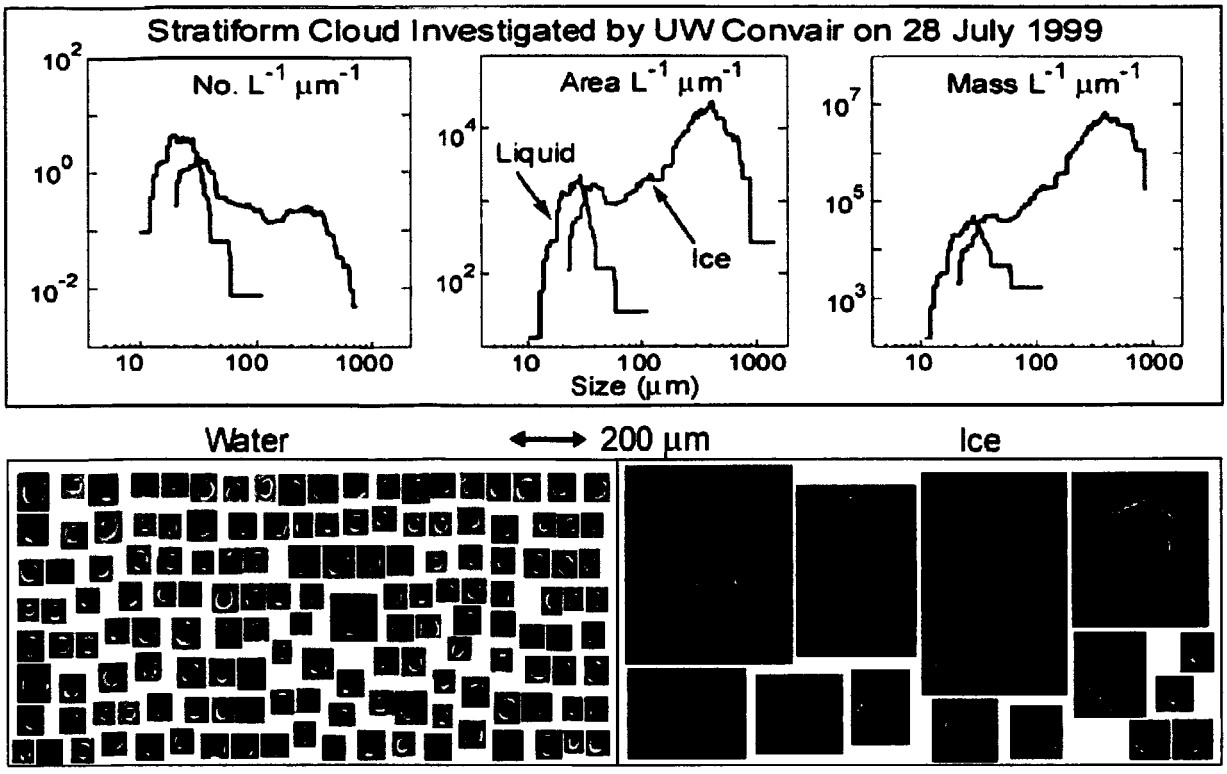

Figure 24. Example showing CPI derived water and ice particle size distributions and images in a stratiform cloud region (083130 - 083258) investigated at –6 ° C by the UW Convair during Kwajex.

Figure 25 shows examples of probability and cumulative distribution functions, along with time series measurements of extinction coefficient. Improved measurements of extinction coefficient are now being computed using the actual projected area of CPI images, plus the projected area from the 2D and HVPS probes. Along with more accurate calculations of extinction coefficient, values of effective radius have also been improved by dividing the integrated third moment by the integrated second moment of the PSD. The more accurate calculations for both IWC and projected area form the basis for an improved calculation of effective particle radius.

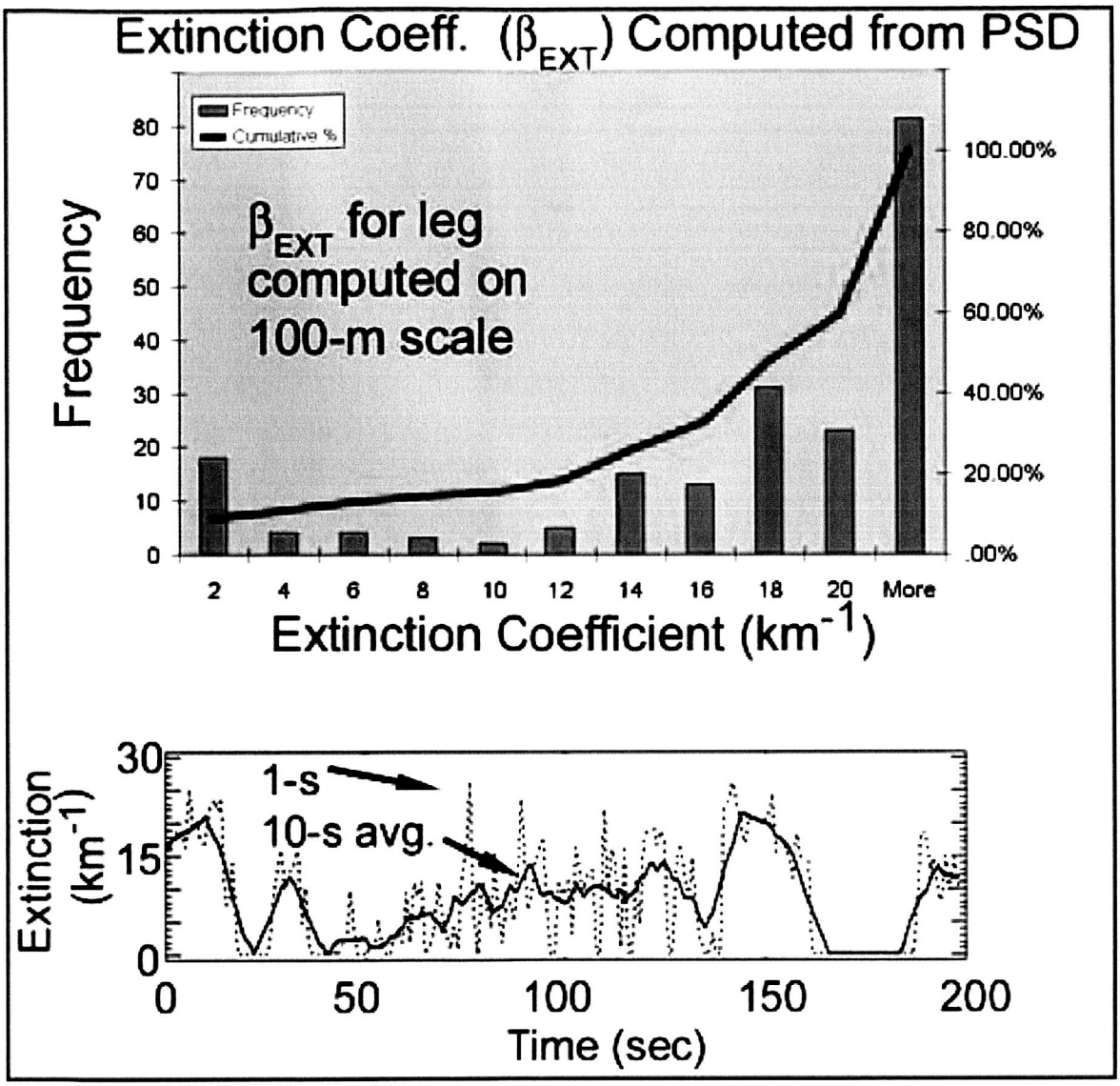

Figure 25. Examples of probability and cumulative distribution functions and time series measurements of extinction coefficient.

2. Software in support of CMP data file production

2.1 Continued support of the Common Microphysical Product (CMP) data files.

The greatest single effort expended during the course of this research has gone into creating software that will allow the creation of Common Microphysical

Product (CMP) data files so that CPI data could be included, and creation of TEFLUN-A CMP data files for submission to the archives. The creation of CMP data files was accomplished by writing the software necessary for all the groups to include CPI data into the CMP data files. As a result of continuous user testing and modifications to the CMP, we also spent considerable time quality controlling our software as well as the TMS software written by Alexei Korolev. For example, we processed and several times re-processed the priority legs from TEFLUN-A. We also processed example data files from other field campaigns as examples of CMP data files with CPI data included. All this is discussed in more detail below.

The generation of the CMP was the top priority of TRMM scientists, and it provided very useful information for validation and improvement of TRMM retrieval algorithms and numerical models. Unfortunately, due to the extensive amount of time spent supporting the development of the CMP, SPEC did not spend nearly as much time on scientific analysis of microphysical data. However, during the course of this effort, SPEC also developed new and improved software algorithms to generate composite particle size distributions, compute ice water content, effective radius, extinction coefficient and radar reflectivity. This report describes these improvements and how they can be applied to scientific analysis of microphysical data collected from the TRMM field campaigns.

We wrote software that includes CPI measurements in the CMP and provided the software with operating instructions to each of the groups processing TRMM aircraft data. We also processed five additional priority legs as examples. Two example legs were processed for the University of Washington group that is responsible for their Convair data from KWAJEX. The scaling of CPI data to the 2DC worked reasonably for much of those data, but there are some segments where the total concentration is low and the scaling factor determined from the leg averaged Particle Size Distributions (PSDs) seems too high to the eye. **Figure 26** shows an example of each case.

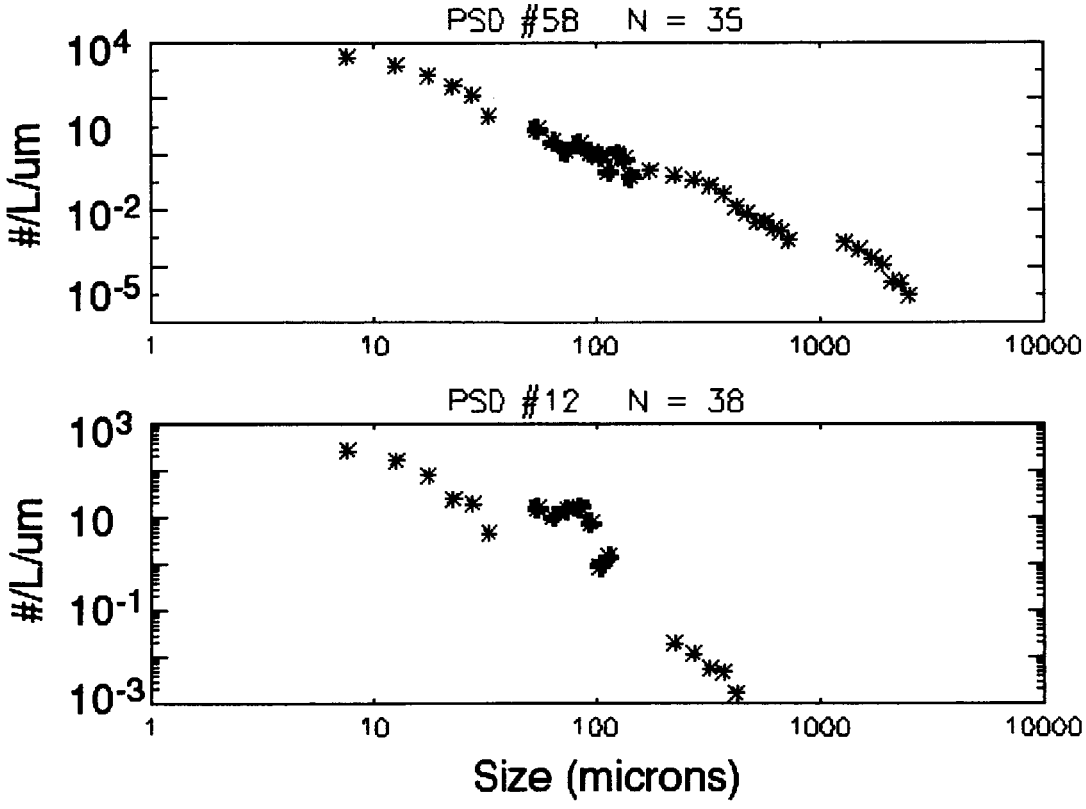

Figure 26. Examples of individual segment PSDs from a CMP data file. The data are from the University of Washington's Convair during KWAJEX. The CPI contribution is in blue.

Two example legs were processed for DRI who are responsible for KWAJEX data from the DC-8. The DC-8 flew primarily in thin cloud and clear air so sampling statistics for the CPI are poor for those data. There are too few particles observed by the CPI in the 150 to 300 micron size range to obtain a valid scaling of the CPI PSD. Most of the CPI data included in the CMPs from

these legs would need to be rescaled by the users or ignored. **Figure 27** shows examples. One leg was processed for the group responsible for KWAJEX Citation data. The scaling worked very well even on a segment-by-segment basis for this leg. Also note that the FSSP was not functioning properly. The FSSP data fills the PSD sizes smaller than 40 microns. Therefore for these data, without CPI data included, there would be no information on sizes smaller than 150 microns. **Figure 28** shows examples.

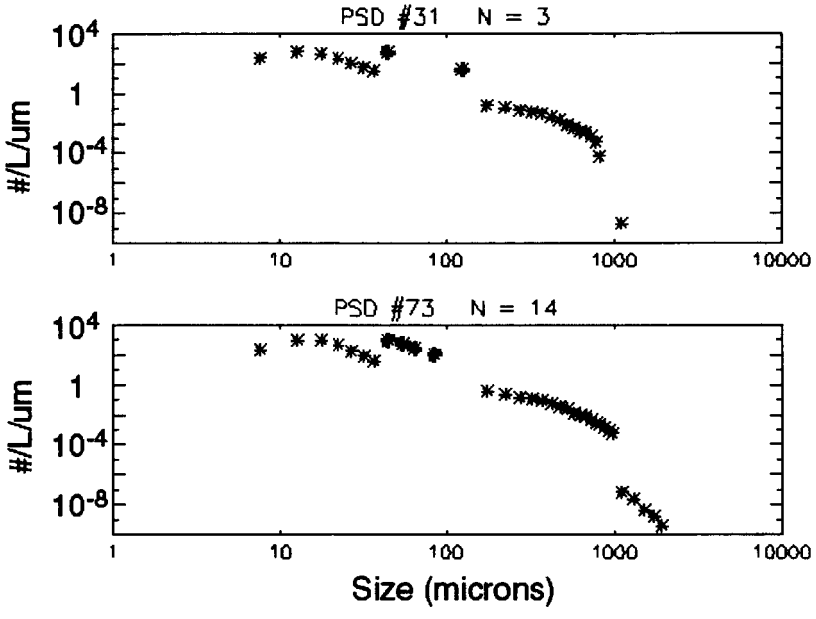

Figure 27. Examples of individual segment PSDs from a CMP data file. The data are from the NASA DC-8 during KWAJEX. The CPI contribution is in blue.

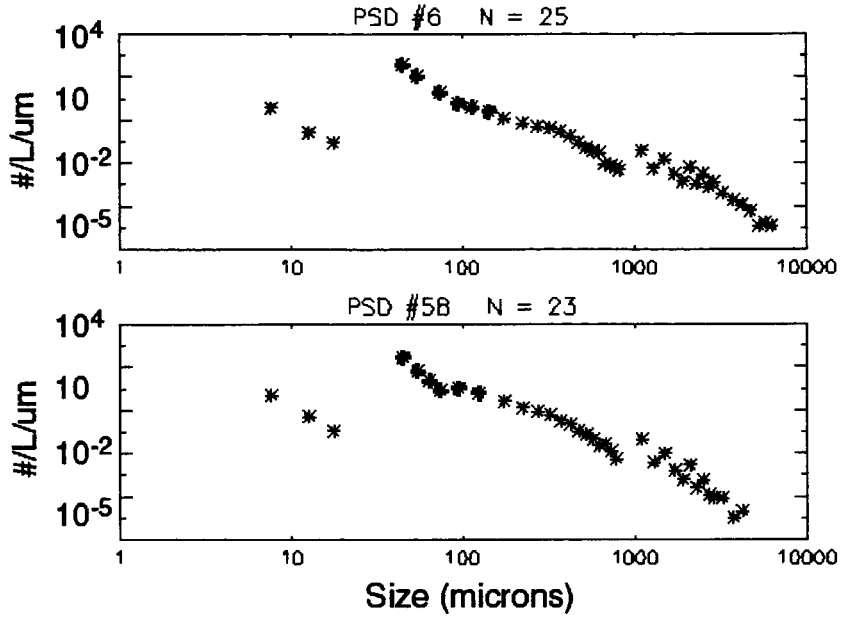

Figure 28. Examples of individual segment PSDs from a CMP data file. The data are from the UND Citation during KWAJEX. The CPI contribution is in blue.

We also produced two additional CMP data files with CPI data included. David Kingsmill chose these examples for use in the manuscript he is writing for publication on the CMP data files. CPI images were provided for these example legs. We have also supported David in his effort to succinctly report on the CPI processing details and will continue to do so until the paper is published.

2.2 Quality control of TMS software and correcting the CMP data files

We found a discrepancy between the particle area distributions produced by the TMS software and what we expected it should produce. We worked with David Kingsmill and Alexei Korolev to isolate the problem in the TMS software and to check that the revised and corrected TMS is now calculating particle area distributions correctly.

Once it was thought that all the bugs were discovered and corrected, we made the final processing of the TEFLUN-A priority legs with CPI data included. CPI images of particles were also included with the submission of the CMP data files. We also worked with Pat Hrubiak on checking and improving the accessibility of these data.

David later found further errors or inconsistencies in the TMS output CMP files. These were correctable without the lengthy process of re-running the TMS

program. David wrote a Matlab program to make the corrections and we applied this to the TEFLUN-A CMP files. The corrected CMP files have been submitted to the DAAC.

3. Submission of TEFLUN-A priority leg CMP data files to the DAAC

Using the software discussed above we processed the three TEFLUN-A legs defined by Gerry Heymsfield and placed the files in the DAAC. The first step in the production of CMP data files is the production of Common Flight Product (CFP) data files. These contain the basic aircraft data excepting particle image data. The format uses position in 1 Km segments as the independent variable. Thus the main task in producing these files is converting the data from the usual format where time is the independent variable to the CFP format. On a leg-by - leg basis quality control is also performed and problems are noted in the CFP file header. This programming task has been completed for TEFLUN-A and files produced for the 3 TEFLUN-A priority legs so far defined.

The next step in the production of CMP data files is to produce an analogous file for CPI data. This is accomplished via software written this year by SPEC that ingests the CFP data file and CPI ASCII data files. Originally it was intended that Korolev would write the TMS software to ingest the CPI ASCII files directly and process the CPI data according to the CMPD format. However, the Korolev contract was approaching its funding limit and there was still considerable code to complete, so it was decided that SPEC would write software to perform the processing and produce these analogous CFP_CPI data files. With SPEC performing this task, Korolev would only need to read the data, scale the PSD to the 2DC data PSD and write the CPI data out to the CMP data file. The main difficulty that was overcome in writing this software was making the best of small samples. Normally we process CPI data over distances large enough to insure statistically significant results. However the CMPD requires 1 Km segments and often the number of particles observed by the CPI is small. Thus, routines were written that optimize the output in regions with low particle concentrations. This software is finished and has been used on data from TEFLUN-A and tested on data from KWAJEX Convair and KWAJEX DC8.

The final step in producing CMP data files is to run the TMS software. It ingests the CFP and CFP_CPI data files and the raw 2D probe data files. In addition to its other functions it scales the CPI PSD to the 2DC PSD in the 150 – 300 micron size range. The TMS program then outputs the CMP data file.

We also wrote software that produces a new CMP file with the CPI data scaled and included. This software ingests a CFP_CPI data file and a CMP file produced by the TMS software that does not yet include CPI data. The new software was written for the following reasons.

1) The Korolev software did not yet perform this task and we desired to submit TEFLUN-A priority leg CMPs to the DAAC, including CPI data as soon as possible.
2) Once the Korolev software is completed and performs this task, the SPEC software can still be used to quality control the Korolev TMS software.
3) The SPEC software was used on actual priority legs to test the utility of the plan to scale CPI PSDs to the 2DC PSDs.

We have used the SPEC software to prepare CMP data files from TEFLUN-A. These files include CPI data, where CPI data exist. This allowed quality control of the process. In addition to finding and correcting bugs in code that we wrote, we also found bugs in the TMS code written for TRMM by Alexei Korolev. As discussed above we reported these bugs to Alexei Korolev and David Kingsmill and worked with them in finding solutions.

A major concern about including CPI data into the strict requirements of the CMP is statistical significance. The CPI often does not collect enough particle images in a 1-km segment to create a full or statistically significant PSD. For that reason new algorithms were written to do the best possible estimate with few particles and it was decided during the coding process to scale the leg averaged CPI PSD to the 2DC leg averaged PSD, instead of scaling on a segment by segment basis, as originally planed. When the number of particles is too low it would not be possible to scale on a segment by segment basis. Here, we show only one leg as an example but for this leg the results are encouraging. The leg is from TEFLUN-A, 18 April, 1998, with a start time of 18:25:00.

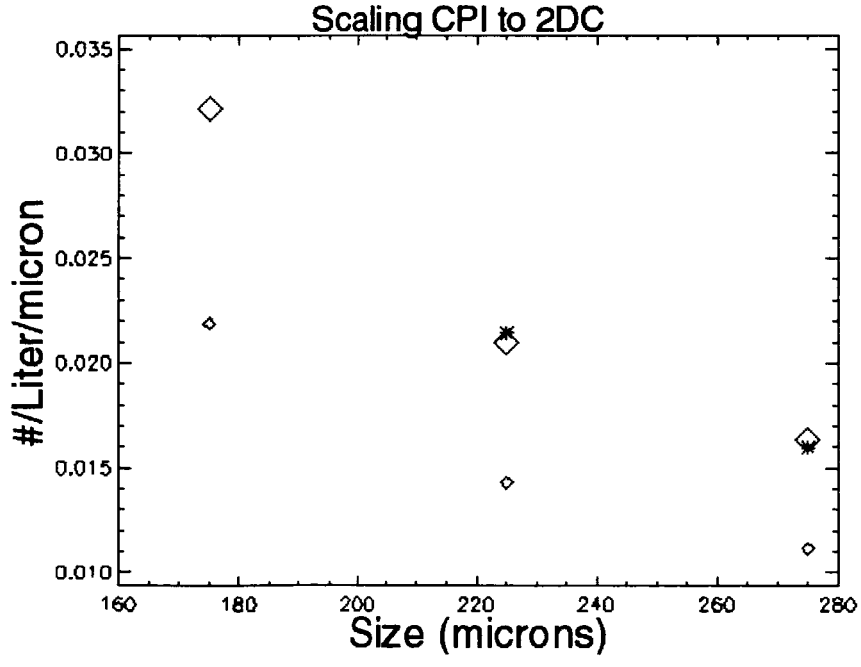

Figure 29: 2DC concentrations for the first three 2DC size bins (asterisks). These are 150-200, 200-250, and 250-300 microns. Also shown are the initial (small diamonds) and scaled (large diamonds) CPI concentrations.

Figure 29 shows how the scaling was accomplished by multiplying the CPI concentrations by a scaling factor. The scaling factor is found by dividing the 2DC concentration, averaged over the whole leg, by the initial CPI concentration, averaged over the whole leg, for each of the first three 2DC size bins, and then averaging the three ratios together. The 2DC data for these three bins are plotted with asterisks. The initial CPI data points are plotted with small diamonds and the scaled CPI data are plotted with large diamonds. The scale factor for this case was about 1.5. There are no 2DC data for the first bin. This is one of the small bugs we found with the TMS software. It was reported and has already been corrected.

Figure 30 shows the resulting full PSD averaged over the whole leg. One factor outside of our control in this process is how the CPI PSD matches up on the small end with the FSSP PSD. For this case the match is excellent. The region from 40 to 150 μm between the FSSP and 2DC is filled in very well using CPI data. We cannot expect such a good match between the FSSP and 2DC PSDs in all cases, but this one case is very promising.

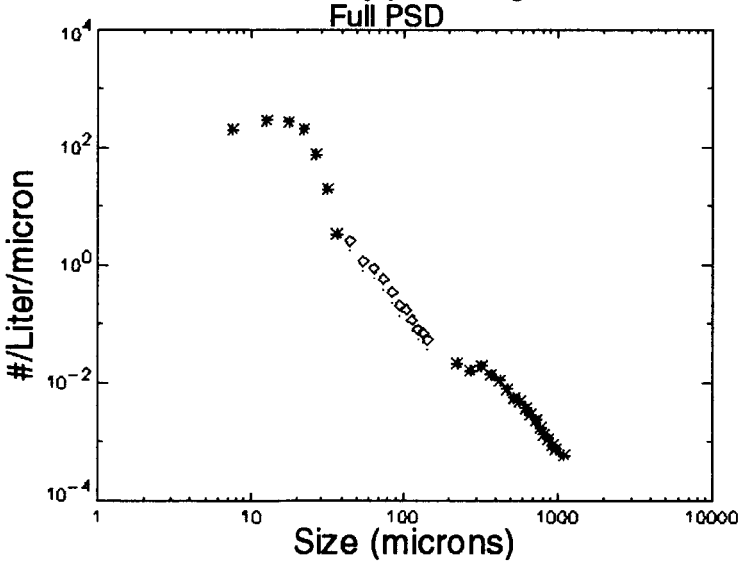

Figure 30: The full PSD averaged over the whole leg. Small sizes with asterisks are FSSP data. CPI data are plotted with diamonds and larger sizes are from the 2DC plotted with asterisks.

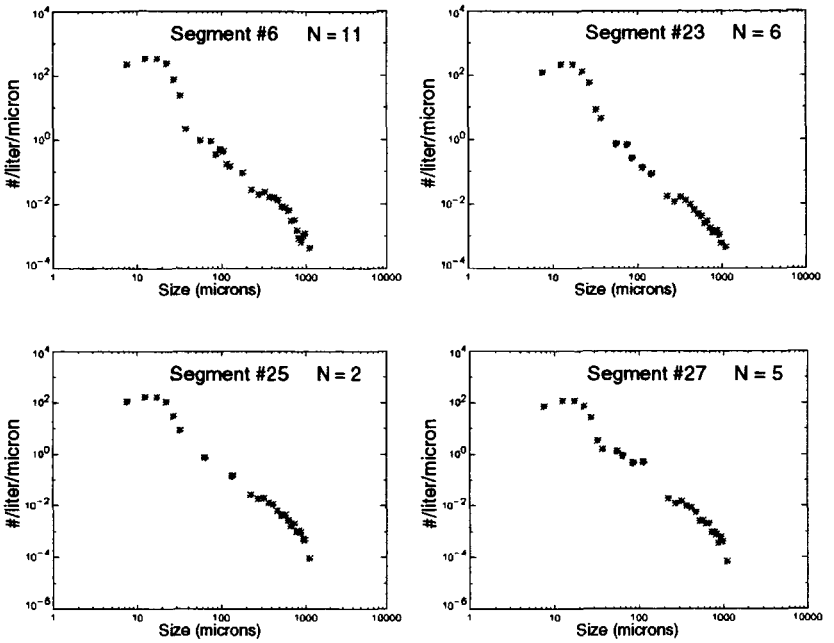

Figure 31: Particle size distributions for 1-Km segments with small N. The CPI part of the particle size distribution is in blue.

The other major uncertainty is the statistical significance of the CPI on a segment by segment basis. When the size distribution is built from only a few particles, we cannot expect great significance. However, for this leg at least, when the number of particles (N) is small, scaling with the whole leg averages worked very well, as shown in **Figure 31**. Again this is promising even though it may not work as well in all cases. When N was larger, scaling with the whole leg average worked less well, as shown in **Figure 32**. This may require users to look at the data and decide whether to accept the values, rescale the values, or ignore them. We have considered more sophisticated scaling algorithms but they are not warranted and would not resolve all scaling problems.

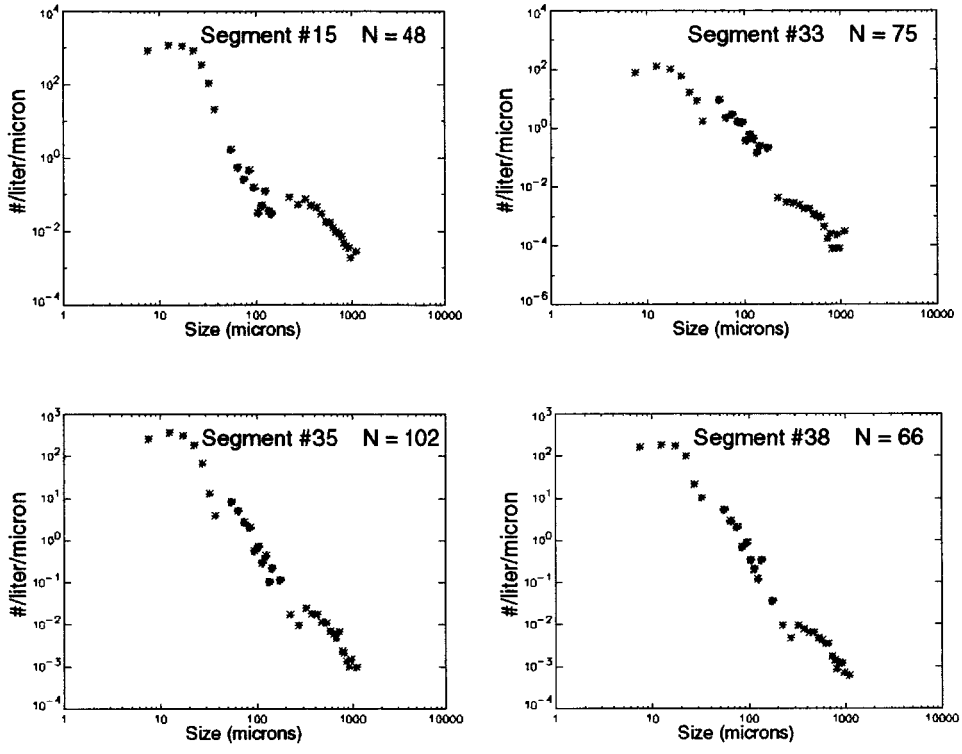

Figure 32: Particle size distributions for 1-Km segments with large N. The CPI part of the particle size distribution is in blue.

4. Analysis of Convective and Stratiform Cloud Regions

TRMM is concerned with identifying the microphysical properties of convective and stratiform regions of tropical clouds. In this case, the stratiform region is a residual of previous convective activity. **Figure 33** shows vertical profiles of particle size distributions, CPI images, LWC and IWC based on a spiral descent conducted by the UND Citation in stratiform and convective regions of a KWAJEX cloud system. The data are typical of measurements collected in other stratiform and convective regions of KWAJEX clouds. The data in **Figure 33** suggest several differences between the stratiform and convective regions:

- In the upper region near –20 to –25 ° C, the stratiform cloud contains very high (> 1 cm^{-3}) concentrations of small ice particles, which are suspected to be a residual from homogeneous freezing and sedimentation of small drops in a convective updraft.

- In the upper region near –20 to –25 ° C, the convective cloud contains aggregates, which are not found lower in the cloud. The stratiform cloud contains aggregates at all levels, with the majority in the lowest levels.

- The convective region contains much higher LWC and drop concentrations than the stratiform region at all levels, and higher IWC in the middle and upper regions. The stratiform cloud contains higher IWC than the convective cloud only at the lowest level.

- Irregular shaped ice particles are found in very high concentrations throughout both convective and stratiform cloud regions.

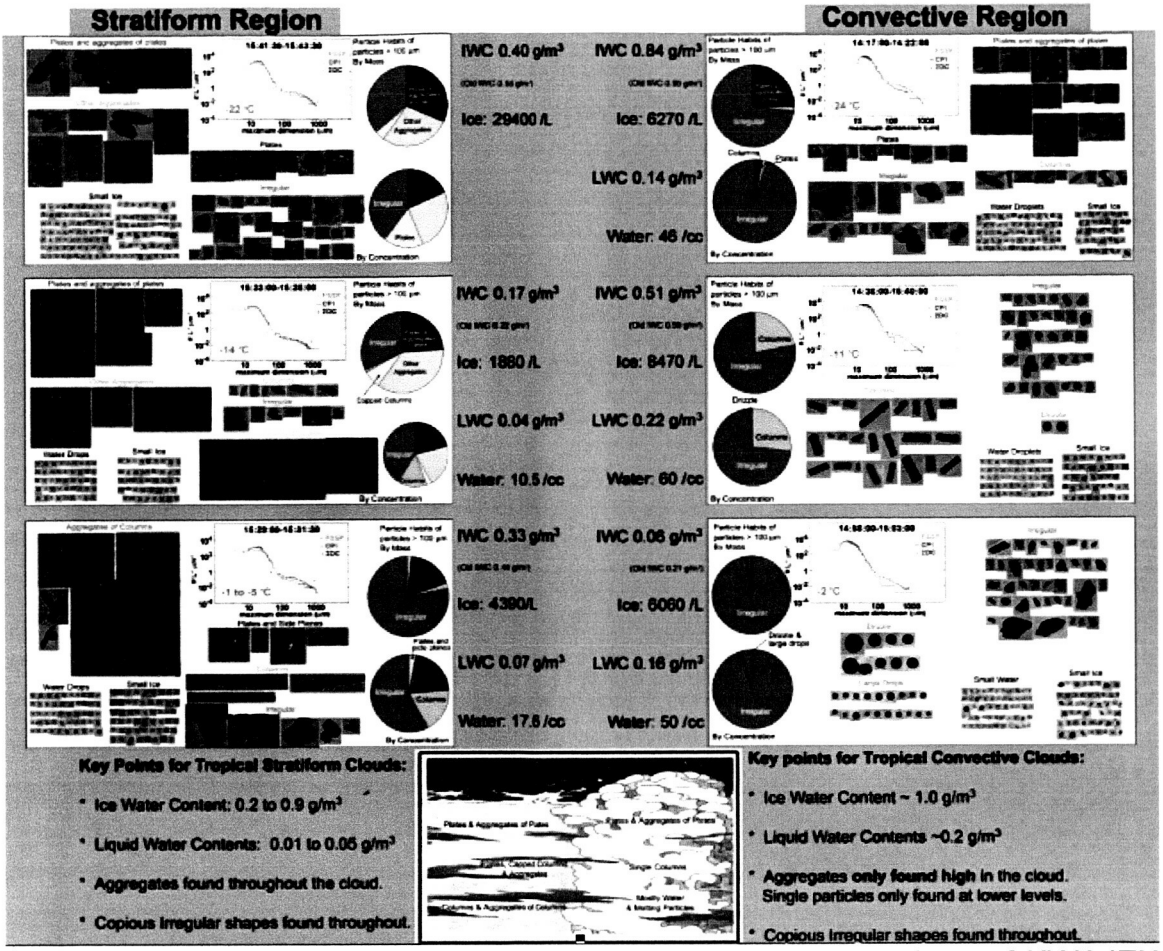

Figure 33. Typical properties of convective and stratiform portions of KWAJEX clouds based on a spiral descent made by the UNS Citation.

5. Analysis of Particle Types in Mid-latitude, Florida, Darwin and Kwajex Anvils

5.1 Comparison of Tropical and Mid-latitude Anvils

Here we present a comparison of the amount and types of ice particles in the outflow regions of mid-latitude, Florida and Kwajex storm outflows (i.e, anvil clouds). Three tropical storms observed during Kwajex are compared with one mid-latitude thunderstorm anvil observed over eastern Colorado. Qualitative comparisons with anvil cloud observations from Darwin Australia and from Florida are also presented. We pay particular attention to observations of aggregates that appear to be formed in the presence of high electric fields.

As shown in **Figure 34**, the SPEC Lear jet penetrated an anvil in three different locations in eastern Colorado. The particles were almost exclusively frozen spheroids and aggregates thereof. **Figure 34** shows examples of images of the aggregates. Of particular interest is the way the spheroids tend to aggregate in long chains. Charges on particles and strong electric fields should enhance aggregation and might also tend to cause these chains. The laboratory work of Saunders and Wahab (1975) supports this speculation. Saunders and Wahab allowed ice particles to aggregate in a cold cloud chamber with and without strong (100 KV/M) electric fields. With the strong electric field they observed chains similar to those we observed in the anvil cloud and shown in **Figure 34**. **Figure 35** shows a reproduction of a photograph of the chains of ice crystals produced in a cloud chamber by Saunders and Wahab.

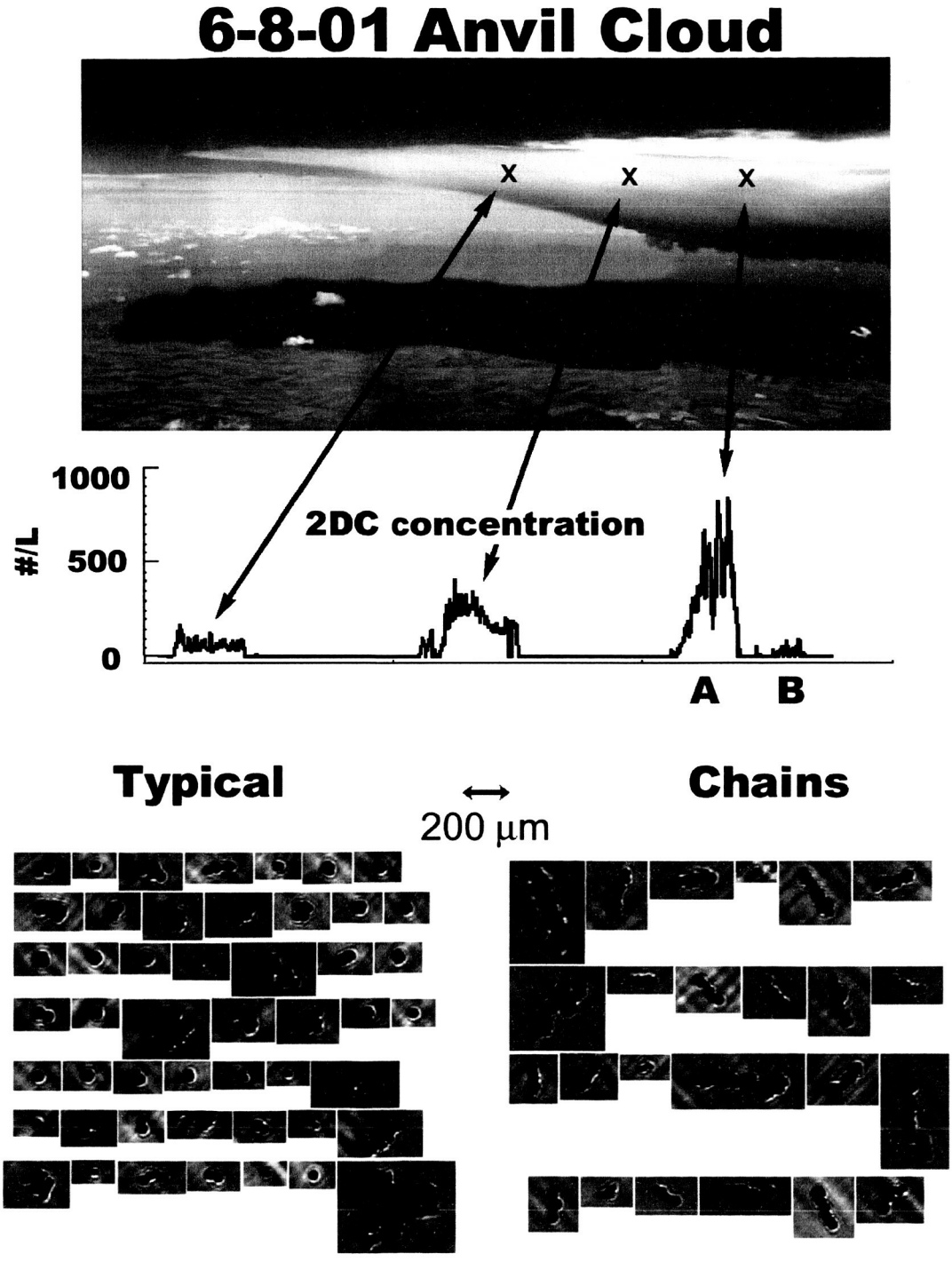

Figure 34. Photograph of anvil cloud and examples of the aggregates and chains observed in an Eastern Colorado thunderstorm anvil cloud on June 8, 2001. Anvils in Eastern Colorado typically have strong electric fields.

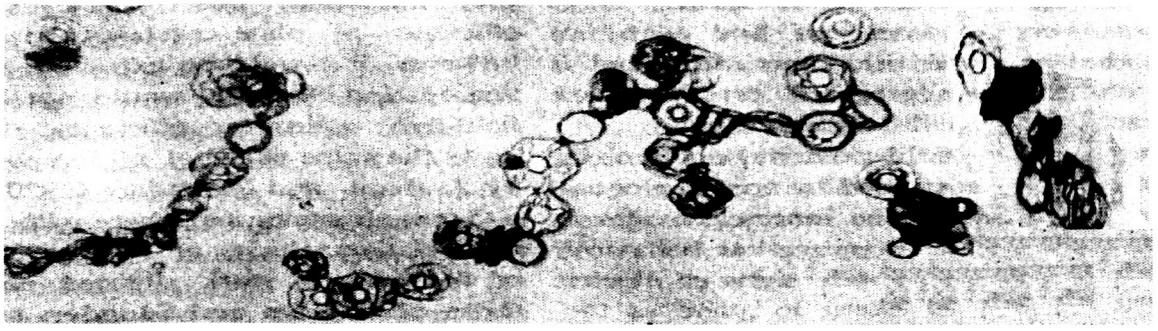

Figure 35. Chains of ice crystals aggregated in a cold chamber under the influence of a strong (100 KV m^{-1}) electric field (from Saunders and Wahab 1975).

Images from three separate aircraft missions during Kwajex when the DC-8 and Citation flew in outflow regions were searched for similar chain-like ice particles. **Figures 36-38** show flight tracks of the aircraft in stratiform outflow regions of Kwajex storms. 19,803 particle CPI images the NASA DC-8 3 August 1998 mission, 8,470 particle CPI images from the CPI on the DC-8 25 August 1998 mission and 58,911 particle CPI images from the UND Citation 2 September 1998 mission were examined for aggregates and chains of small particles. On these missions the aircraft spent most of their in-cloud-time in the stratiform precipitation regions of cloud.

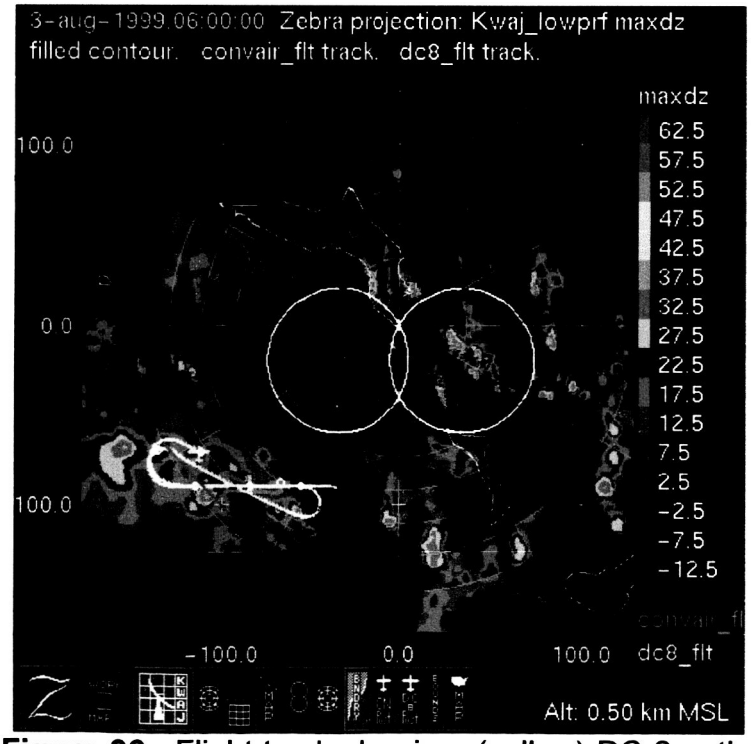

Figure 36. Flight track showing (yellow) DC-8 path in the stratiform outflow (anvil) region of the tropical storm on 3 August 1999.

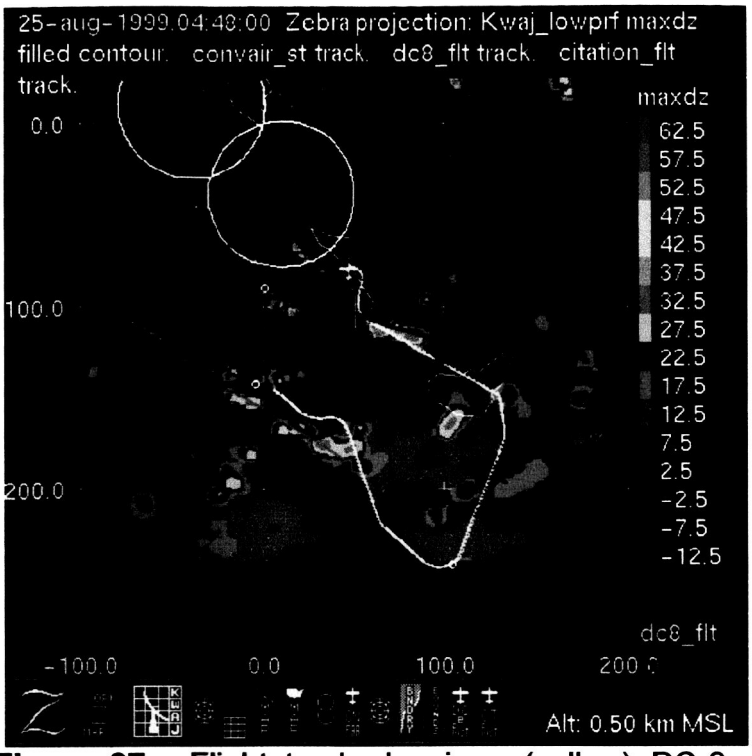

Figure 37. Flight track showing (yellow) DC-8 path in the stratiform outflow (anvil) region of the tropical storm on 8 August 1999.

These stratiform regions are what remain after the convection that initially formed the cloud has decayed. Thus, these regions are the most similar region in these clouds to the anvil region of a mid-latitude continental thunderstorm cloud, such as the cloud shown in **Figure 34**. **Figures 39, 40 and 41** show typical images from each of the Kwajex missions just described. **Table 3** presents results of counting the percentage of images that were chains, doublets, or other aggregates. Notice also that besides the lack of chains, aggregates of other types were nearly absent in these Kwajex clouds, compared to about a 30% occurrence in the eastern Colorado anvil. Doublets are aggregates of two and only two small particles. These were quite noticeable on the 2 September 1998 Citation mission (**Figure 41**) and on the Lear 8 June 2001 mission (**Figure 34**).

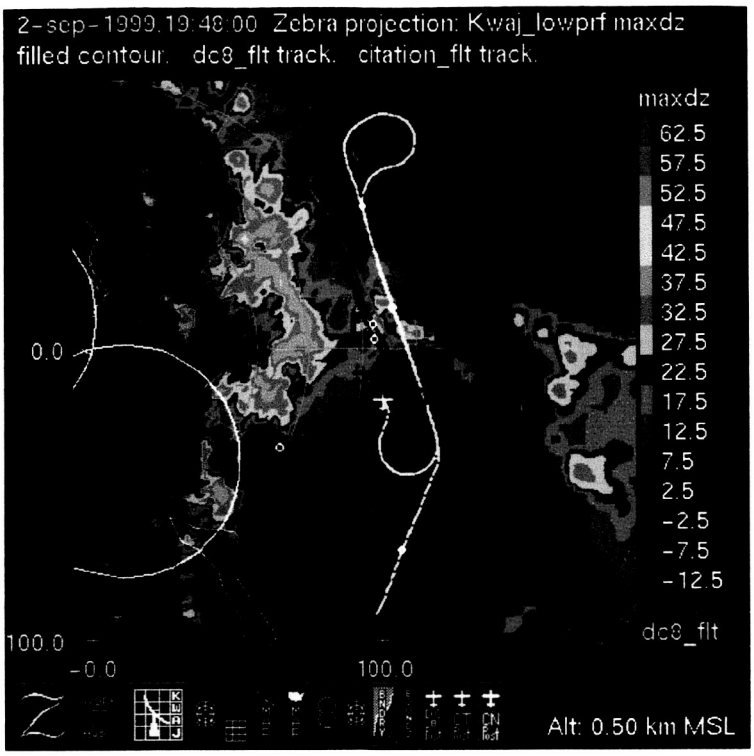

Figure 38. Flight track showing (cyan) Citation path in the stratiform outflow (anvil) region of the tropical storm on 2 September 1999.

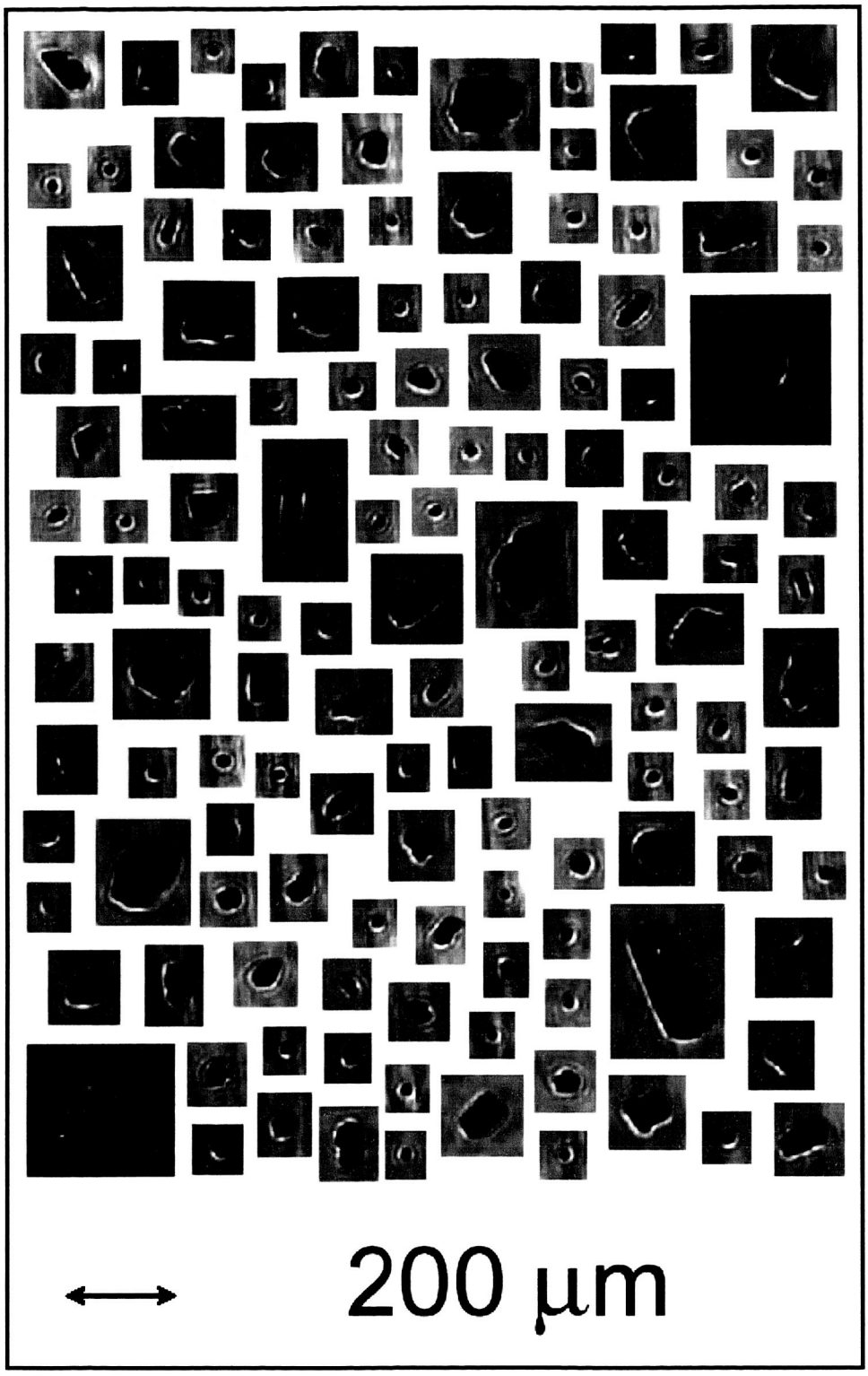

Figure 39. Typical particles from the 3 August DC-8 Kwajex mission. Anvils in clouds in the Central Pacific typically have low electric fields.

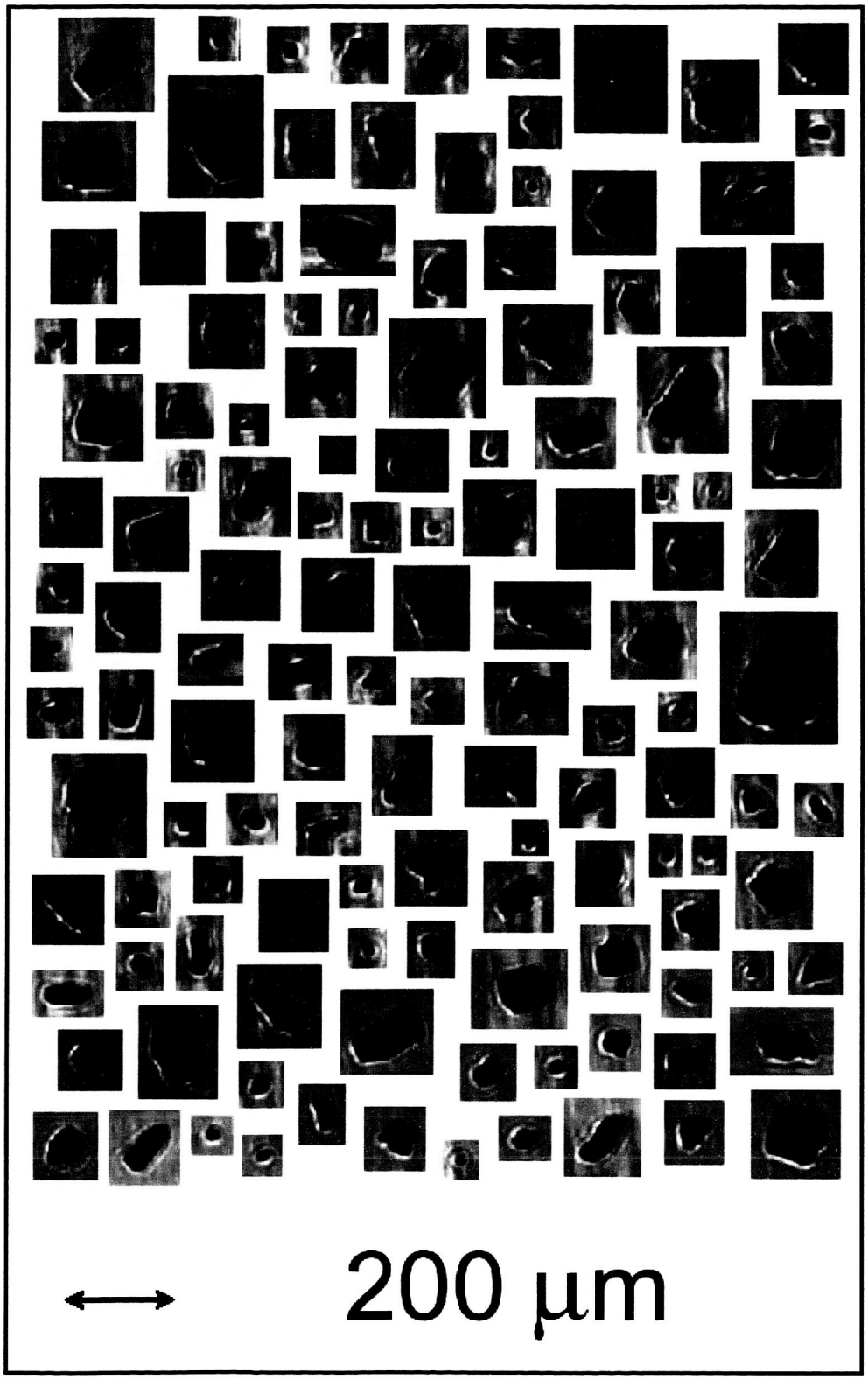

Figure 40. Typical particles from the 25 August DC-8 Kwajex mission. Anvils in clouds in the Central Pacific typically have low electric fields.

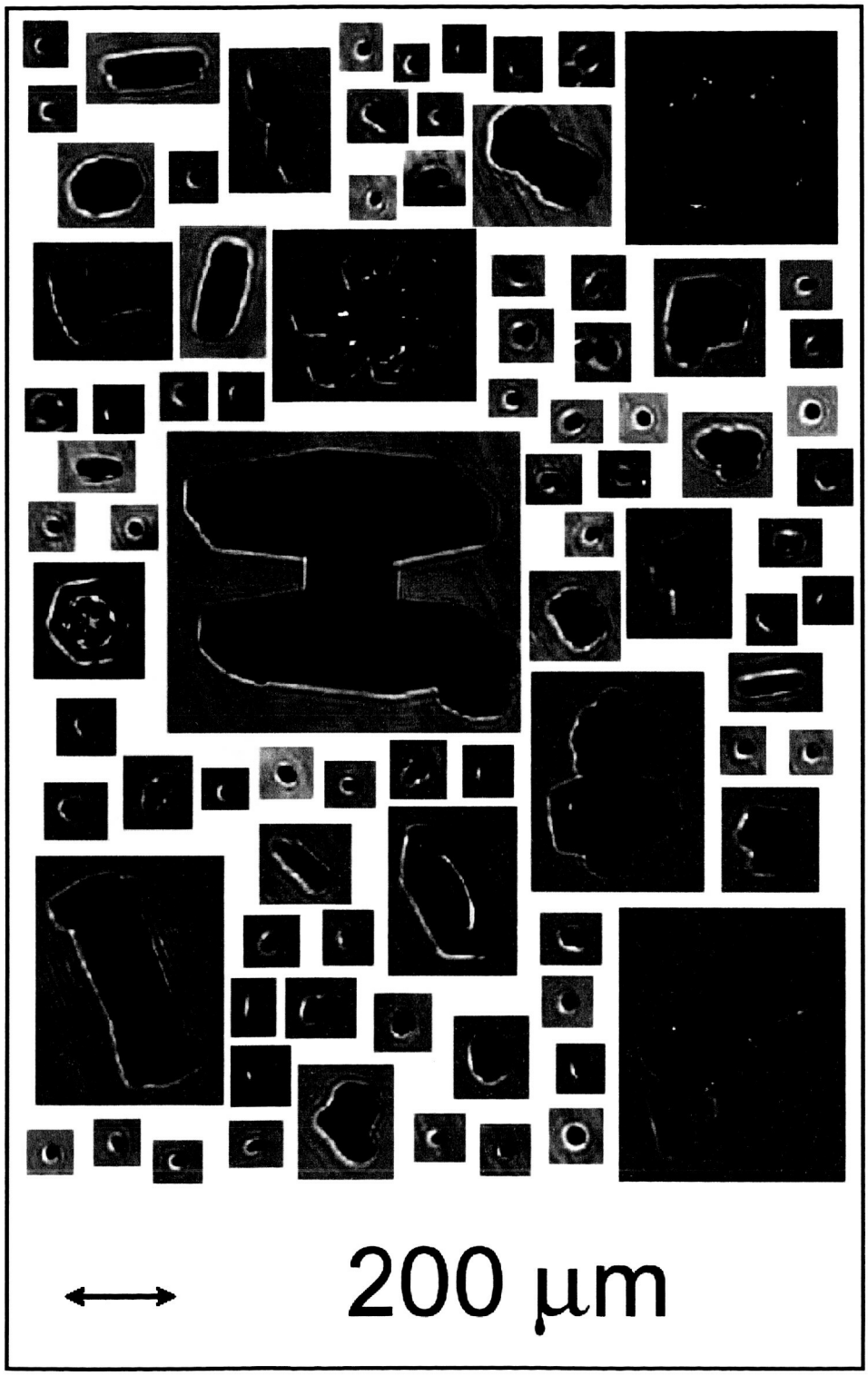

Figure 41. Typical particles from the 2 September Citation Kwajex mission. Anvils in clouds in the Central Pacific typically have low electric fields.

Table 3.

Comparison of the amount of aggregation in different storm outflow regions.

	# particles counted	% chains	% doublets	% other aggregates	Temperature
6-8-01a	3400	3	6	25	-47 C
6-8-01b	1400	2	5	32	-47 C
6-8-01c	3800	2	4	28	-47 C
8-3-98	3900	0	1	0.4	-40 to -60 C
8-25-98	1700	0	0.1	0.5	-55 C
9-2-98	11000	0	2.3	1.4	-5 to -40 C

Figure 42 shows a map of lightning frequency where it can be seen that, despite the frequent occurrence of cumulus nimbus, the frequency of lightning in the Kwajelein area is orders of magnitude less than in eastern Colorado. Thus we can speculate again that the differences in aggregation seen in these storm outflow regions has been influenced by the degree of electrification.

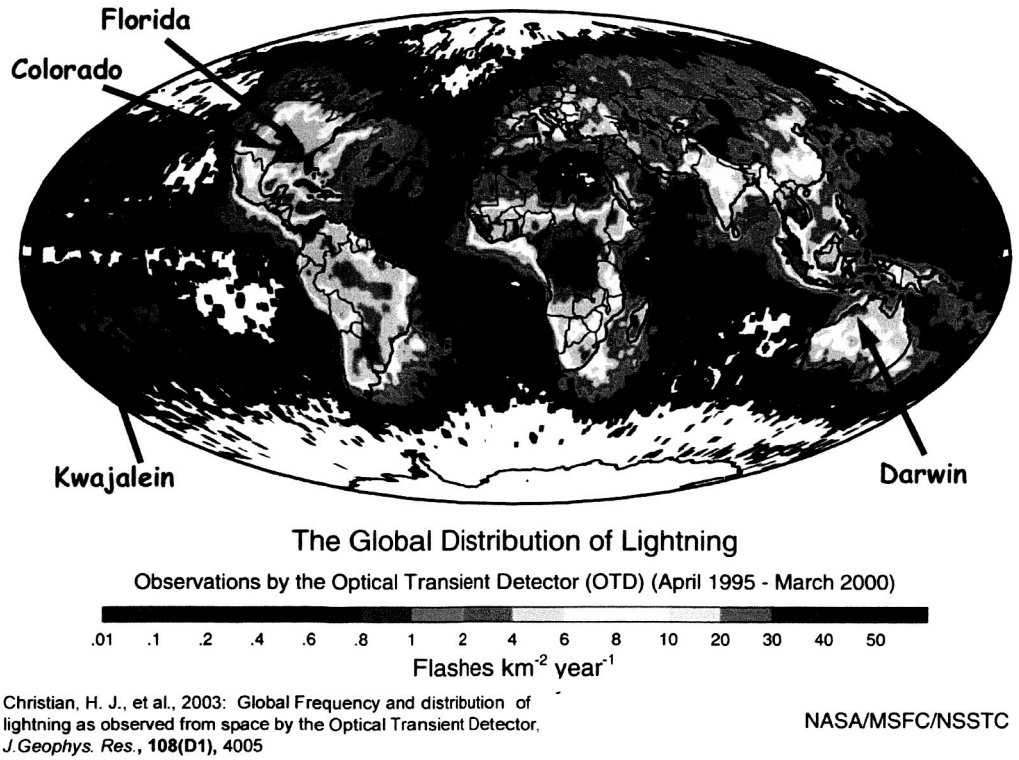

Figure 42. Annual distribution of lightning flashes (after Christian et al. 2003).

Other data sets were also qualitatively searched for occurrences of chain aggregates. An example of CPI images of chain aggregates found in a Florida anvil cloud investigated with the NASA WB-57 aircraft during the Crystal Face project on 16 July 2002 are shown in **Figure 43**. Similar CPI images of chains (also shown in **Figure 43**) were also observed in an anvil cloud near Darwin, Australia by an Egrett research aircraft operated by Airborne Research Australia during the Emerald II project (http://users.aber.ac.uk/ccc97/emerald.htm). The data were provided courtesy of Dr. Martin Gallagher of UMIST. Both Florida and Darwin are seen in **Figure 42** to have high rates of lightning like Eastern Colorado. This is again consistent with the speculation that lightning rates indicate higher electric fields, which influence aggregation in the storm outflow regions.

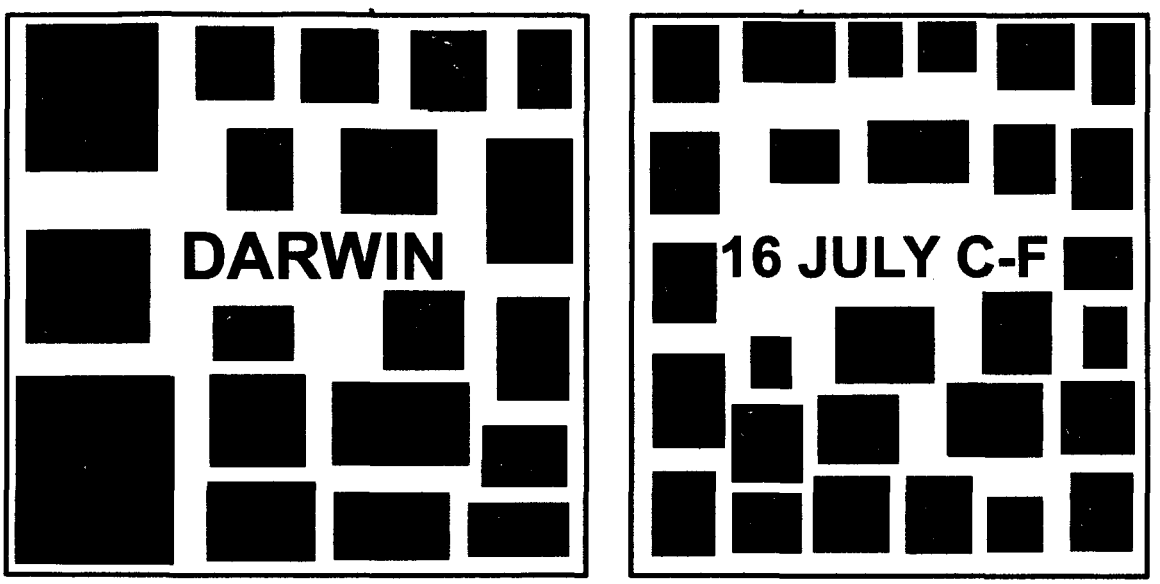

Figure 43: Examples of CPI images showing chainlike aggregates from anvil clouds investigated during the Emerald II (Darwin) and Crystal Face (Southern Florida) projects, where anvils typically have high electric fields.

5.2 A Detailed Analysis of Particle Shapes in Tropical and Mid-latitude Anvils

In addition to the generalized analysis of tropical and mid-latitude anvils, we performed a detailed analysis of the particle types in the anvil regions of mesoscale storms investigated during KWAJEX (Kwajalein) and CRYSTAL-FACE (South Florida). In each case, we examine the properties of the ice crystals from data collected at two levels near the tops of each anvil. As explained in the previous section, the striking difference in particle types is hypothesized to be a result of the difference in electric field strength of storms in the two locations.

The analysis of particle types is labor intensive because, unlike other cloud regions, anvils often contain particle shapes that cannot be identified using automated techniques. Approximately 3,000 CPI images were classified manually and sorted into categories. Examples of CPI images in each of the categories are shown in **Figure 44.**

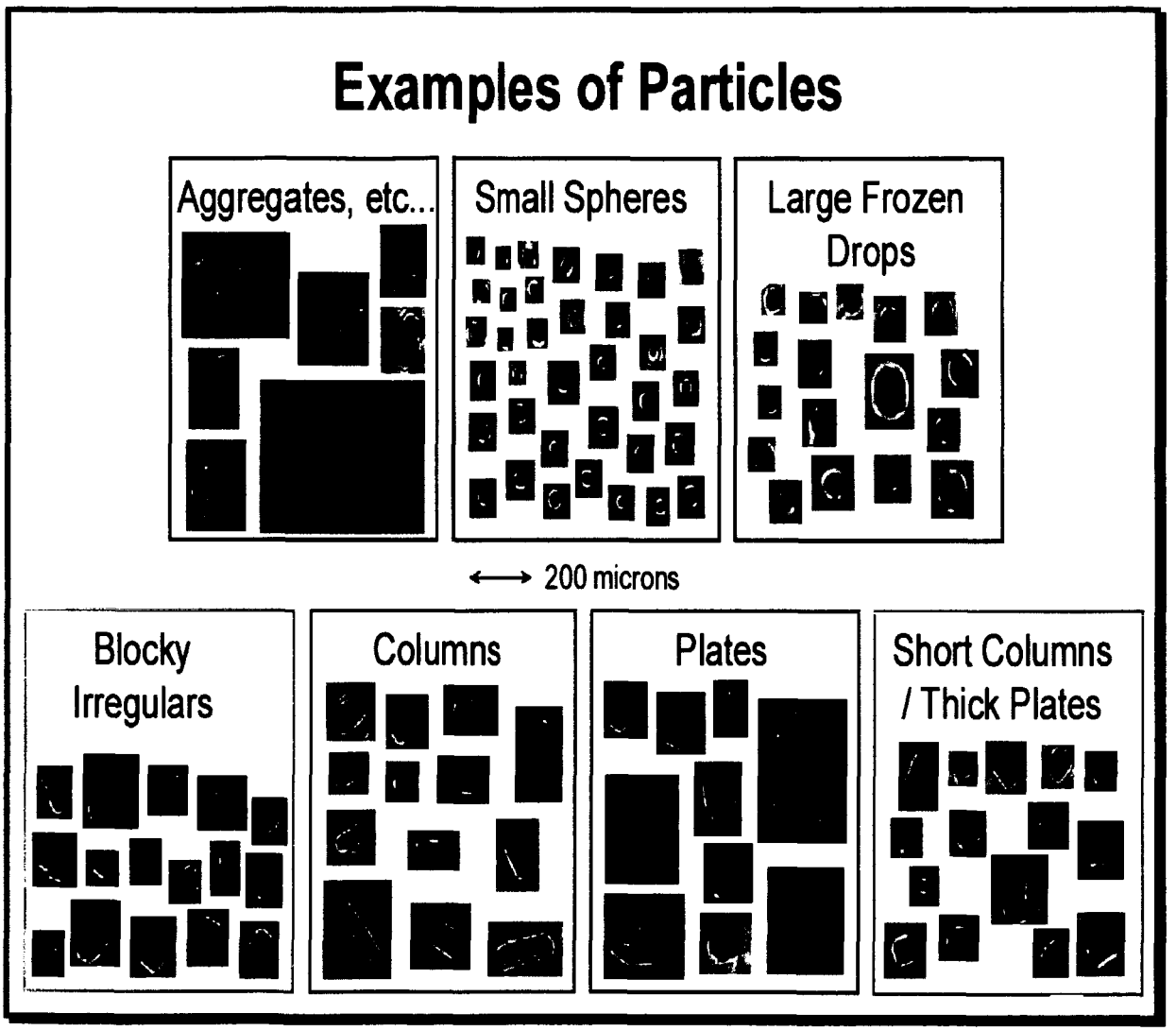

Figure 44. Examples of CPI images found in each of the seven categories used to classify particle types in anvils. Note that the Aggregates, etc., category includes rimed particles, particles with sideplanes and aggregates that look like "chains" of particles.

Proj.	Date/Times (UTC)	FL (x100ft)	T (C)	Conc (#/L)	IWC (g/m^3)	β_{ext} (Km^{-1})	R_{eff_a} (μm)	R_{eff_b} (μm)
C-F	16 July 02 2037-2038	460	-65	12027	0.87	45	31	32
C-F	16 July 02 2034-2035	390	-39	4759	0.61	29	244	35
KWAJ	3 August 99 0501-0506	400	-60	3540	0.08	5	47	28
KWAJ	3 August 99 0510-0514	400	-60	4860	0.13	7	63	29
KWAJ	3 August 99 0533-0536	350	-41	8275	0.16	12	75	22

Table 4. Values of Temperature (T), total particle concentration (Conc), ice water content (IWC), extinction coefficient (B_{ext}), and effective radius computed using two different techniques (R_{eff_a} and R_{eff_b}) for aircraft penetrations at two different levels (FL 460 and FL 390) for a CRYSTAL-FACE (C-F) anvil and three levels of a KWAJEX (KWAJ) anvil.

Table 4 shows summary values for each of the flight legs flown in CRYSTAL-FACE (C-F) and KWAJEX anvils. The KWAJEX measurements were made by the DC-8; the C-F measurements at FL 460 were made by the WB-57 and at FL 390, they were made by the Citation. It can be seen from **Table 4** that the particle data collected in the C-F anvil were denser and the resulting ice water contents (IWCs) and extinction coefficients were considerably larger. We do not mean to imply that the two cases presented here are typical of IWCs and extinction coefficients found in all C-F and KWAJEX anvils. Instead, we will focus our discussion mainly on the particle types, which are very typical of other cases investigated in the respective locations.

The KWAJEX data were collected during horizontal legs at –60 ° C and –41 ° C in the anvil region of a convective system investigated on 3 August 1999. Radar plots with overlays of the DC-8 and UW Convair flight tracks for the time period of interest are shown in **Figures 45-47**. The PPI and RHI plots of radar reflectivity suggest that this was a stratiform region with precipitation reaching the surface. The Convair reported flying in mostly stratiform cloud and occasional convective cells. The C-F data were collected during horizontal legs at –65 ° C and –39 ° C in the anvil region of a convective system investigated on 16 July 2002 near the southwestern tip of Florida. Radar plots with overlays of the WB-57 and UND Citation flight tracks for the time period of interest are shown in **Figure 48**. As can be seen from **Table 4** and **Figures 45-48** the horizontal legs were flown at approximately the same temperatures in the anvil regions of

convective systems, however, the mass of ice particles was higher in the C-F case.

Figures 49 & 50 show composite particle size distributions (PSD) from the FSSP, CPI and 2D-C probes for all five legs shown in **Table 4**. In these figures the upper-level measurements are shown in blue and the lower-level legs are shown in gold. At both locations the PSDs show that the larger particles are found on the lower-level legs in the anvil. Also, the C-F PSD shows a significantly higher concentration of particles in the 50 to 200 μm size range at the upper level.

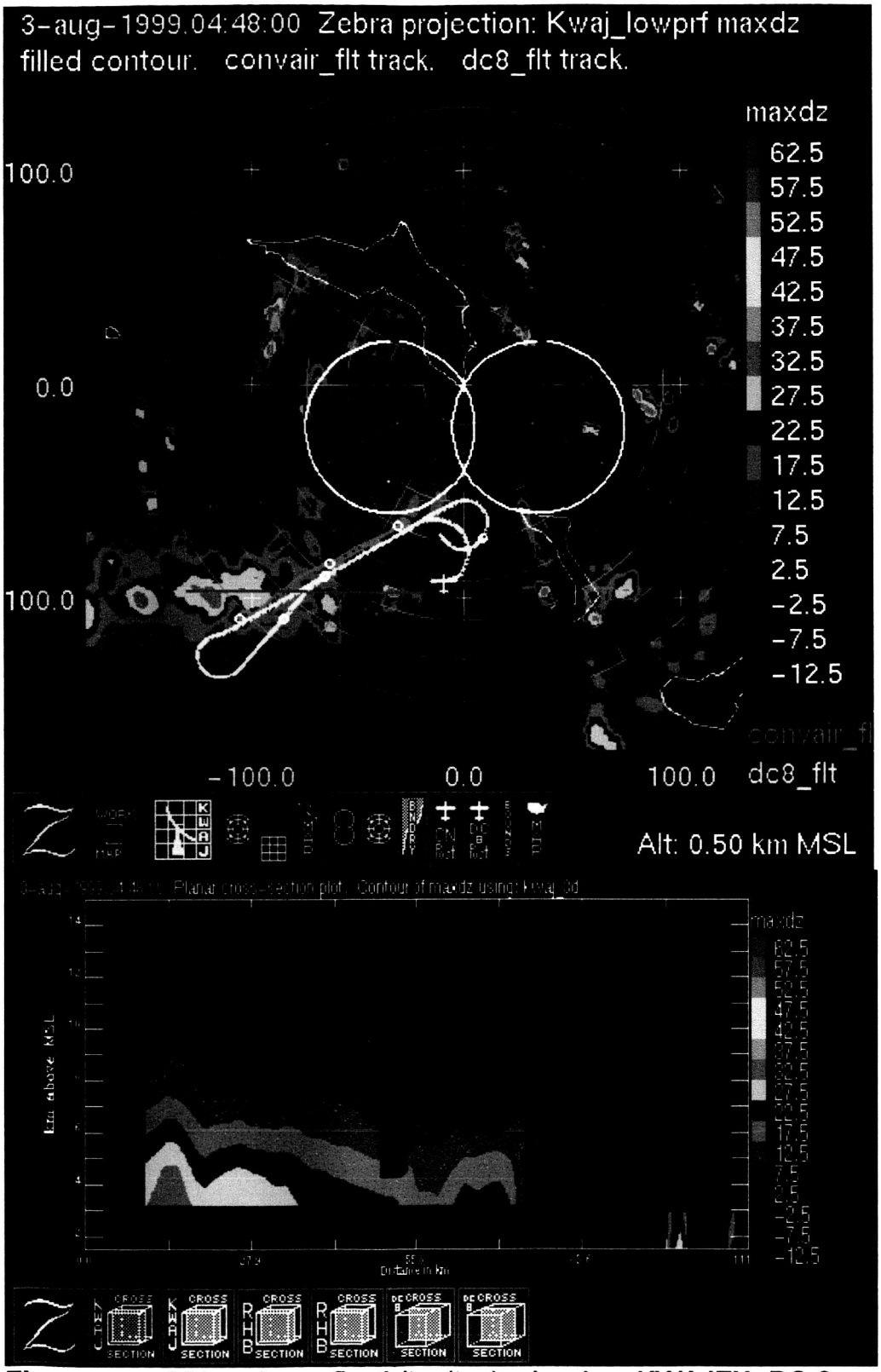

Figure 45. PPI radar reflectivity (top) showing KWAJEX DC-8 and Convair flight tracks, and (bottom) RHI slice through the light blue line shown on the PPI plot for the time period 04:48 – 05:11 on 3 August.

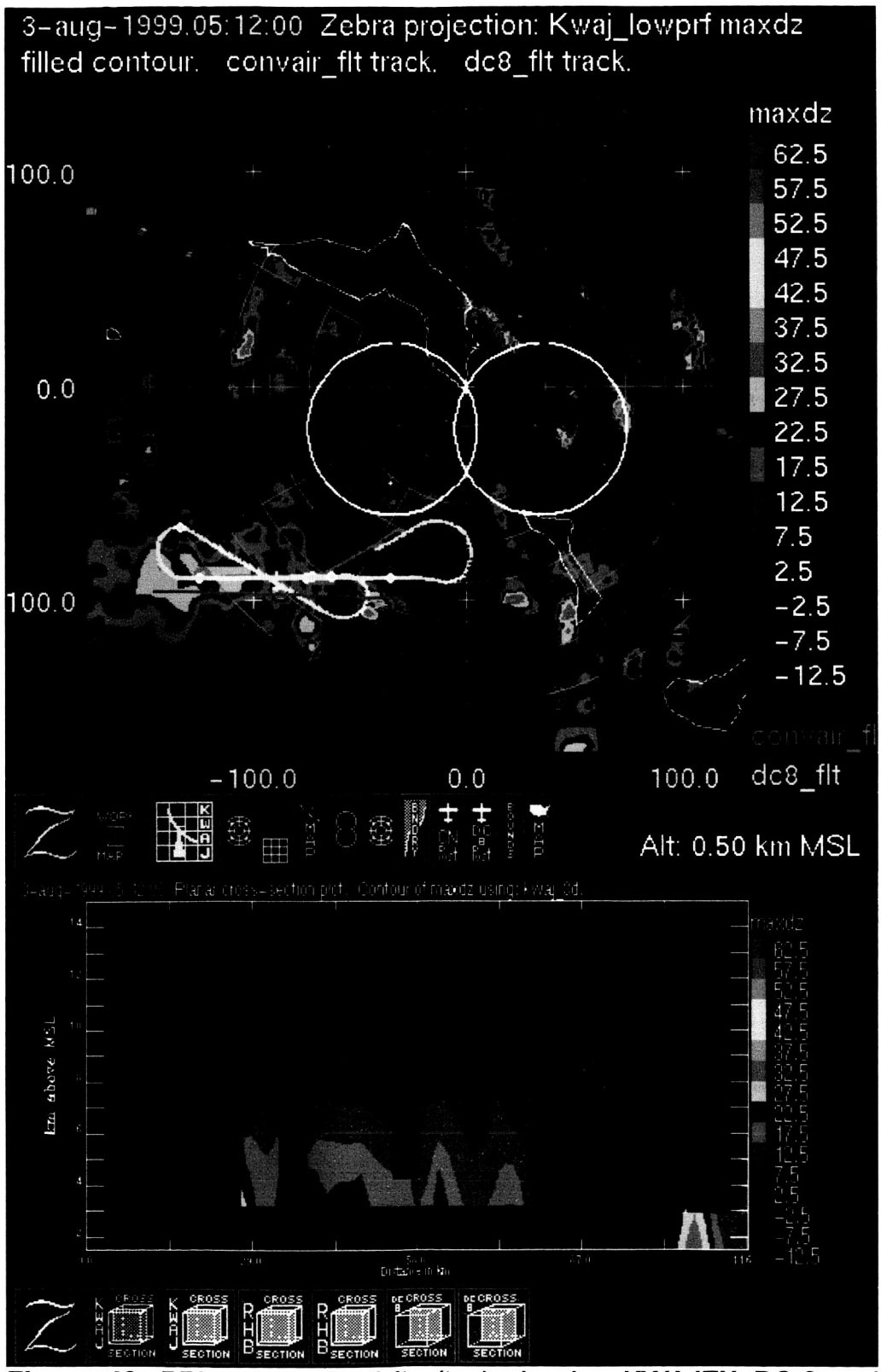

Figure 46. PPI radar reflectivity (top) showing KWAJEX DC-8 and Convair flight tracks, and (bottom) RHI slice through the light blue line shown on the PPI plot for the time period 05:12 – 05:35 on 3 August.

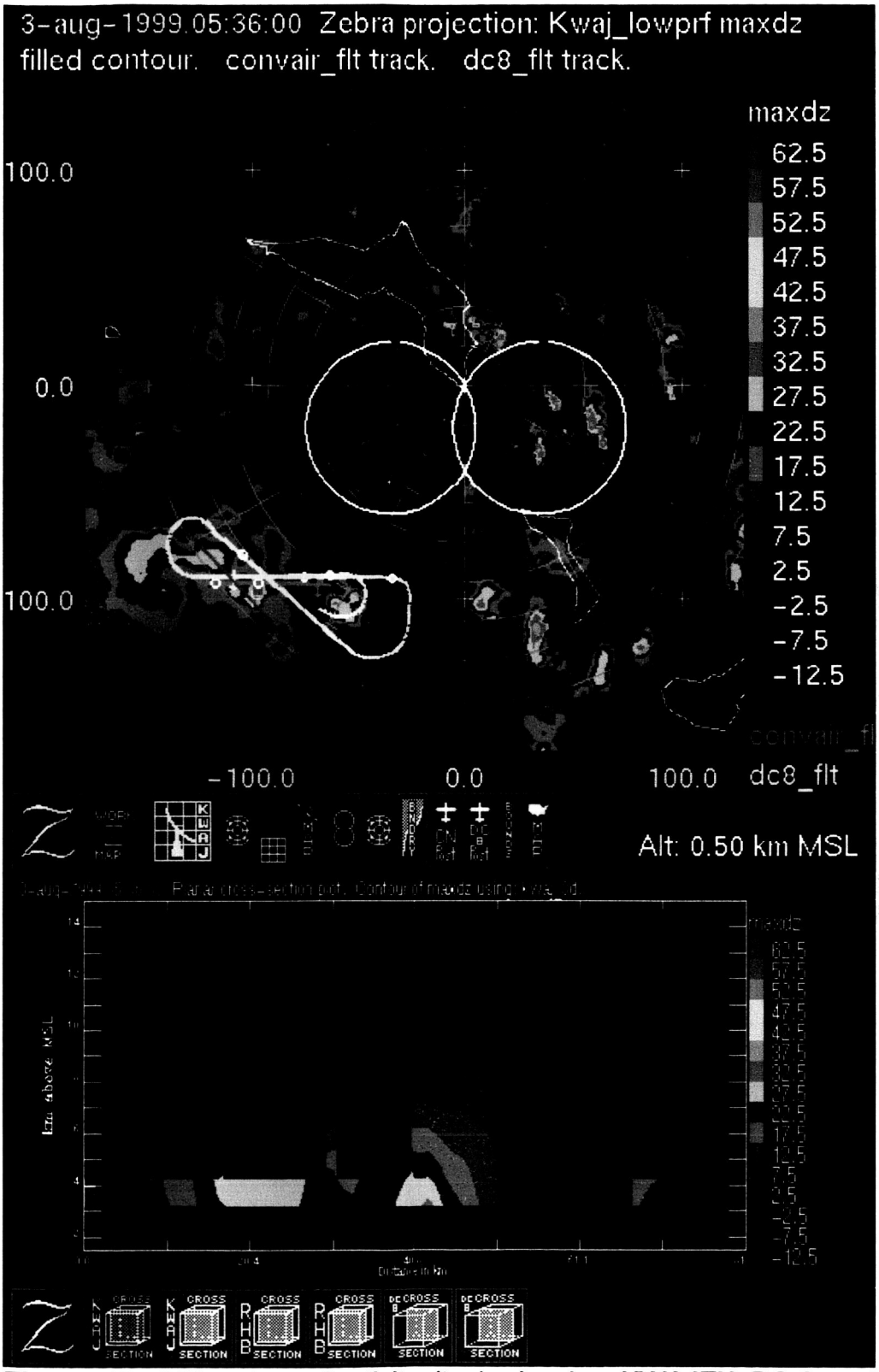

Figure 47. PPI radar reflectivity (top) showing KWAJEX DC-8 and Convair flight tracks, and (bottom) RHI slice through the light blue line shown on the PPI plot for the time period 05:36 – 05:59 on 3 August.

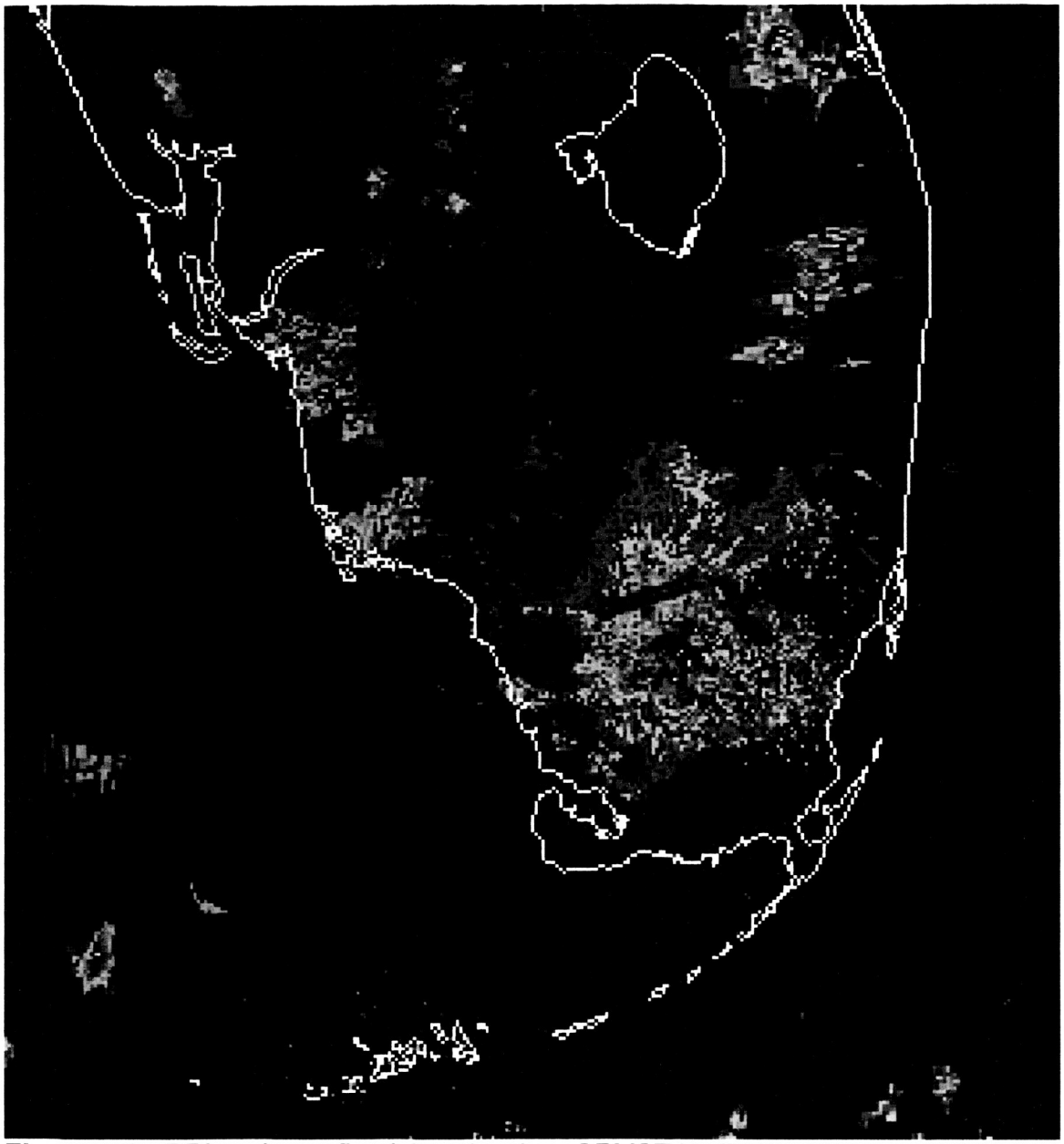

Figure 48. PPI radar reflectivity showing CRYSTAL-FACE DC-8 and Citation flight tracks for the time period 05:12 – 05:35 on 16 July 2002.

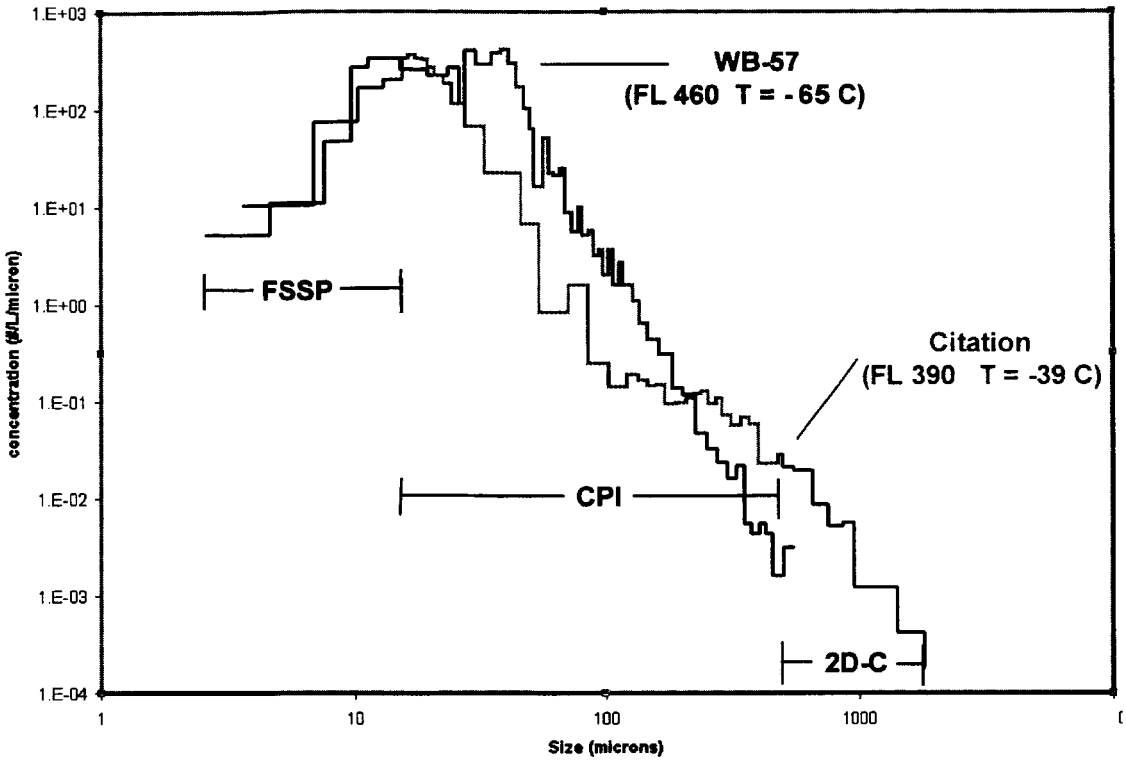

Figure 49. Particle size distributions measured by the WB-57 and Citation in a CRYSTAL-FACE anvil.

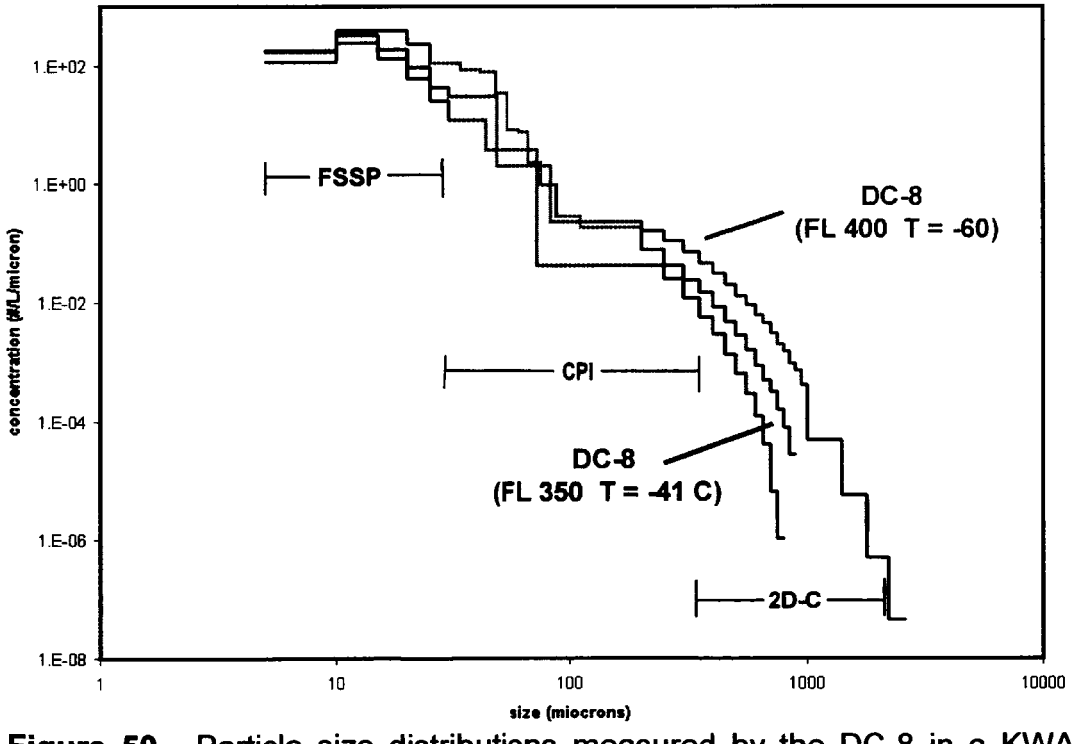

Figure 50. Particle size distributions measured by the DC-8 in a KWAJEX anvil.

As mentioned previously, the principal difference between the particle characteristics observed over Florida and near Kwajalein is found in the shapes of the particles. **Figures 51-54** show the C-F and KWAJEX PSDs for both the upper and lower levels in a form t that codes the relative percentages of particle types as a function of size, area, and mass. The key at the left of each PSD can be referenced to **Figure 44** to see examples of actual CPI images of the particles in each category. The striking difference between the PSDs from C-F and KWAJEX is that the overwhelming majority of the larger particles observed in the KWAJEX anvil are categorized as blocky irregular single particles, whereas most of the larger particles observed in the C-F anvil are aggregates, rimed particles or particles with sideplanes. While these examples are not statistically significant, our inspection of CPI images from several different anvils investigated during KWAJEX and in C-F and mid-latitudes suggests that these trends are typical.

A question begs to be answered: What are the differences in the physics of (maritime) tropical compared with (continental) Florida and mid-latitude anvils that are responsible for the observed differences in crystal types? In particular, the question can be asked: What processes could contribute to the formation of complex crystals observed in the C-F storms that are not present in the tropical storms? Two distinctive differences between tropical and mid-latitude storms often reported are that updraft velocities are much higher and lightning is more prevalent in mid-latitude storms. For example, Jorgensen and LeMone 1989; Wei, et al. 1998 found that the maximum updraft velocities in the central Pacific during GATE and TOGA-COARE did not exceed 15 m s^{-1}, while updraft velocities up to 50 m s^{-1} have been recorded in mid-latitude storms (Musil et al. 1986). As shown in **Figure 42,** the frequency of lightning strikes is much higher in Florida and mid-latitudes than it is in the Central Pacific (Christian et al. 2003).

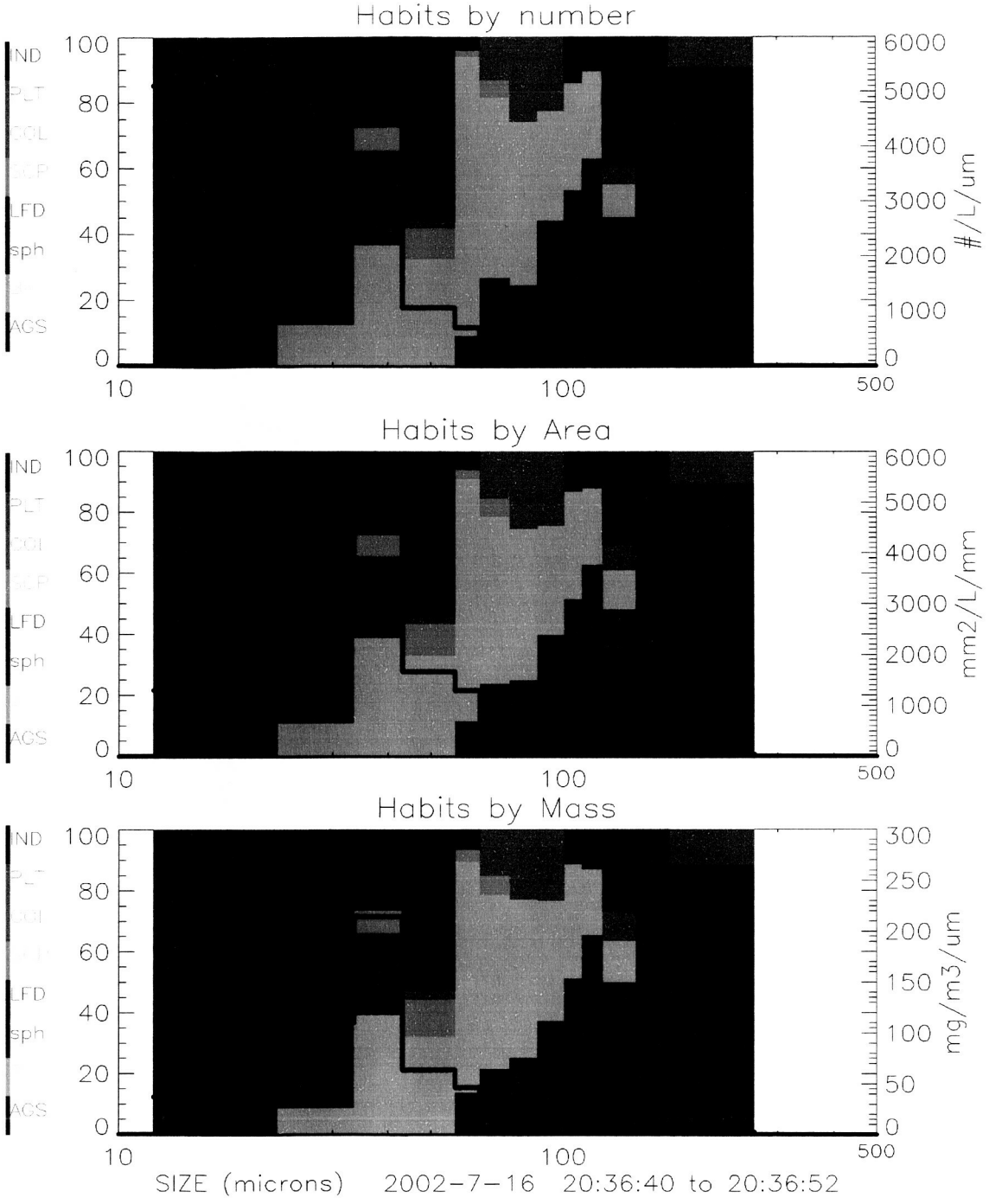

Figure 51. Particle size distributions (PSDs) shown as a function of (top) number, (middle) area and (bottom) mass for the C-F Leg at FL 460 (-65 ° C). The black line in each PSD is referenced to the vertical axis at the right. The color-coding shows the percentage of each particle type as a function of particle size shown on the x axis. The particle types are: AGS = Aggregate, Sideplane or Rimed, BKI = Blocky Irregular, Sph = small spheroidal, LFD = Large Frozen Drop, SCP = Short Column/Thick Plate, COL = Column, PLT = Plate, IND = Indistinguishable.

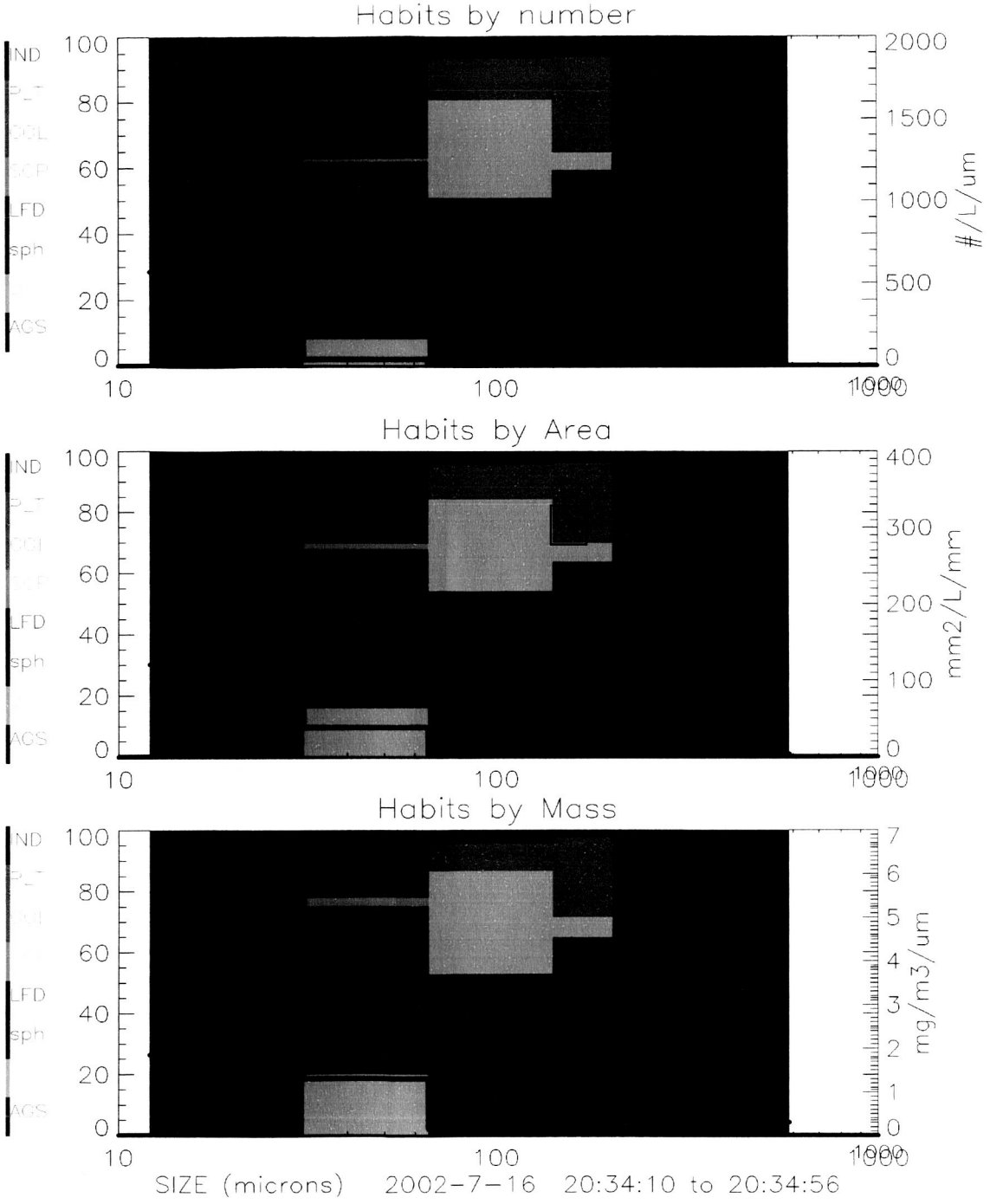

Figure 52 Particle size distributions (PSDs) shown as a function of (top) number, (middle) area and (bottom) mass for the C-F Leg at FL 390 (-39 ° C). The black line in each PSD is referenced to the vertical axis at the right. The color-coding shows the percentage of each particle type as a function of particle size shown on the x axis. The particle types are: AGS = Aggregate, Sideplane or Rimed, BKI = Blocky Irregular, Sph = small spheroidal, LFD = Large Frozen Drop, SCP = Short Column/Thick Plate, COL = Column, PLT = Plate, IND = Indistinguishable.

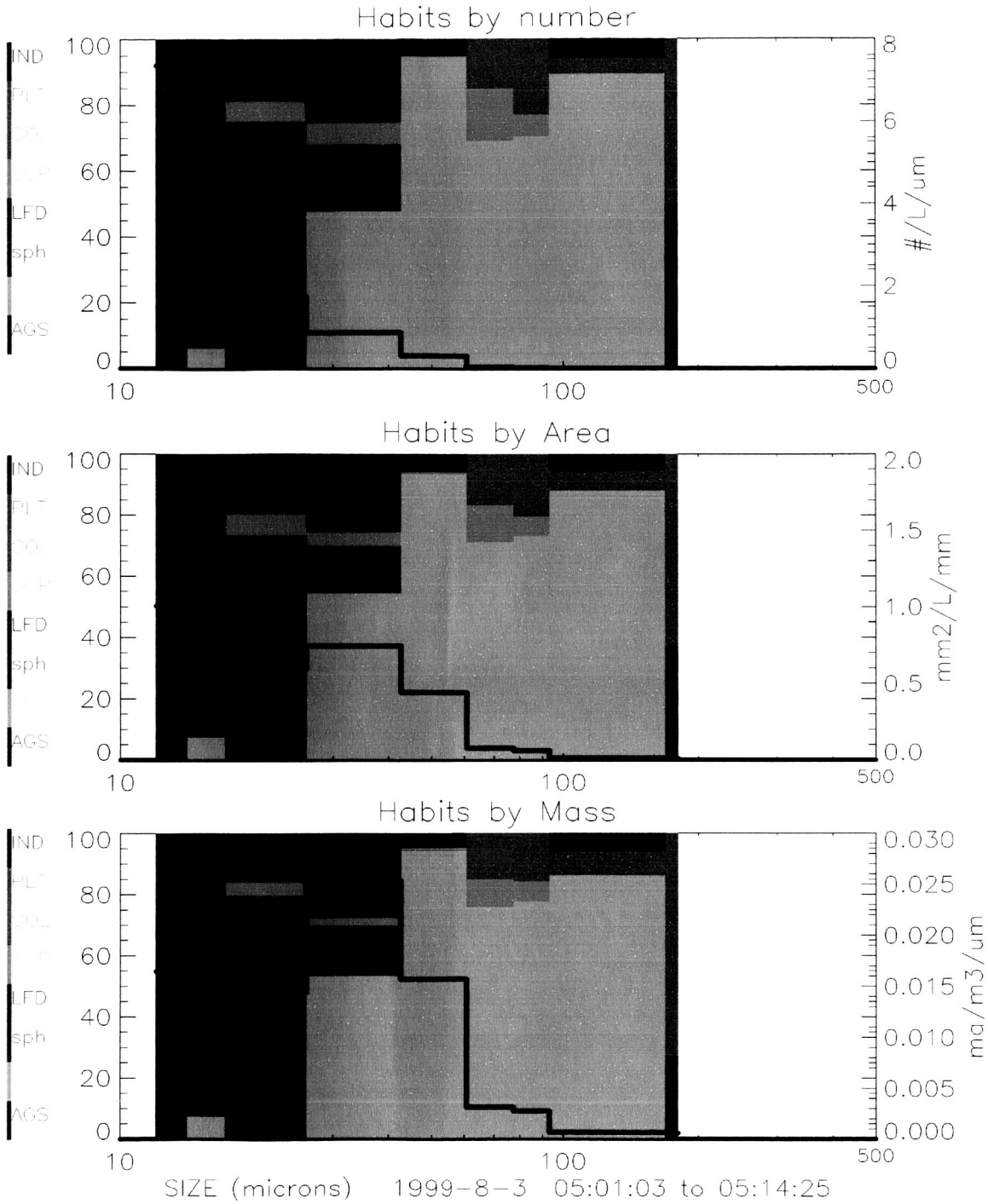

Figure 53. Particle size distributions (PSDs) shown as a function of (top) number (middle) area and (bottom) mass for KWAJEX Leg at FL 400 (-60 ° C). The black line in each PSD is referenced to the vertical axis at the right. The color-coding shows the percentage of each particle type as a function of particle size shown on the x axis. The particle types are: AGS = Aggregate, Sideplane or Rimed, BKI = Blocky Irregular, Sph = small spheroidal, LFD = Large Frozen Drop, SCP = Short Column/Thick Plate, COL = Column, PLT = Plate, IND = Indistinguishable.

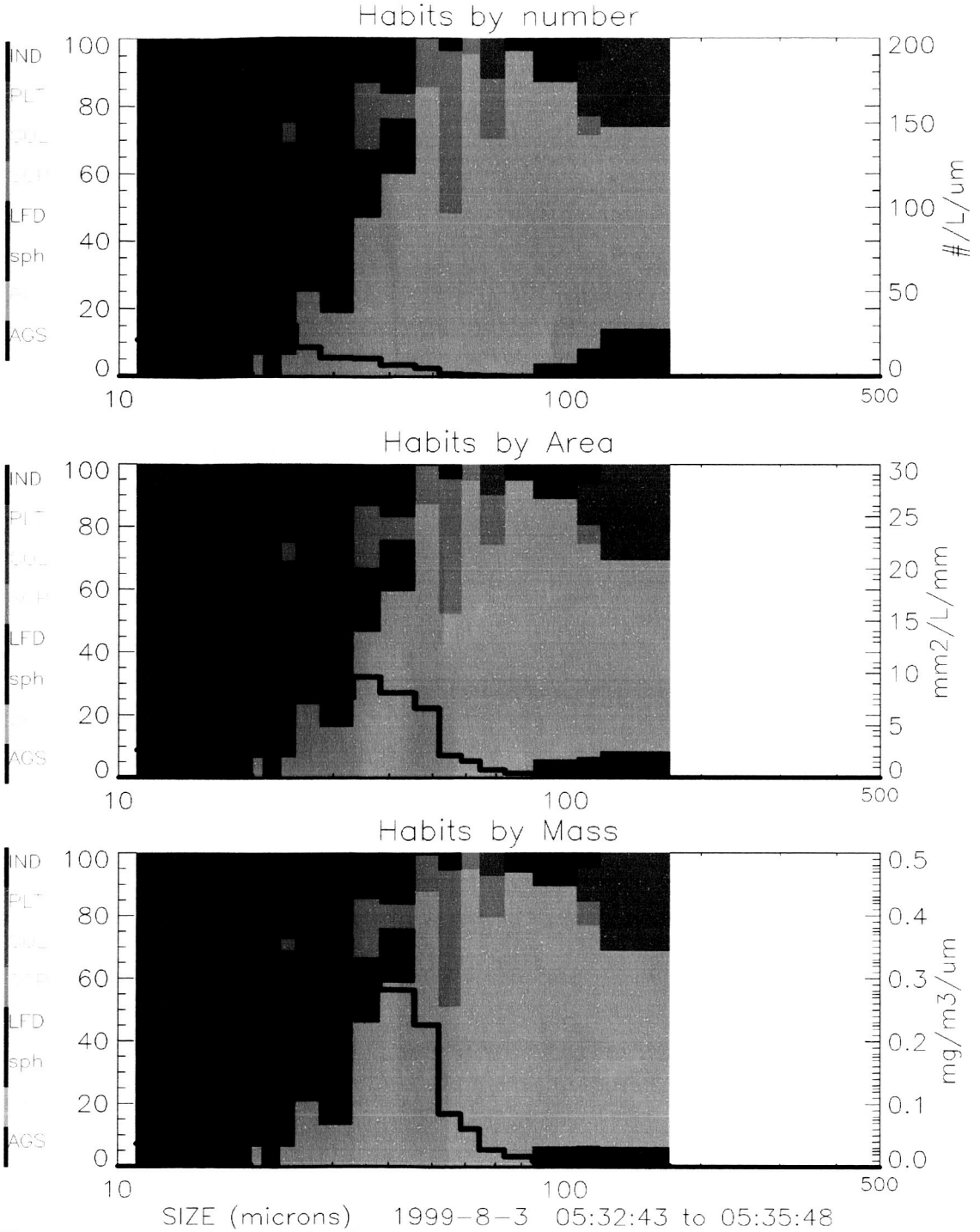

Figure 54. Particle size distributions (PSDs) shown as a function of (top) number (middle) area and (bottom) mass for KWAJEX Leg at FL 350 (-41 ° C). The black line in each PSD is referenced to the vertical axis at the right. The color-coding shows the percentage of each particle type as a function of particle size shown on the x axis. The particle types are: AGS = Aggregate, Sideplane or Rimed, BKI = Blocky Irregular, Sph = small spheroidal, LFD = Large Frozen Drop, SCP = Short Column/Thick Plate, COL = Column, PLT = Plate, IND = Indistinguishable.

The existence of high concentrations of small particles in the C-F anvil suggests a process where cloud drops are transported to high, cold elevations in the storm before being frozen. The cloud drops then freeze homogeneously near –37 ° C and the strong updrafts presumably transport the frozen drops into the anvil region of the storm. CPI observations show that most of the small (< 50 μm) frozen ice particles are not spherical, but instead, typically have a quasi-spheroidal shape, which may be multi-faced "droxtals." As explained by Ohtake (1970), if crystals form from supercooled water droplets near –40 ° C, the droplets may freeze so quickly that the crystals do not have time to reach an equilibrium state for the development of normal hexagonal and rectangular faces. The result is a particle that appears to be quasi-spheroidal or potato-shaped because the resolution of the image is not good enough to see the multiple facets.

Thus, the high updrafts that carry frozen drops aloft could explain the higher concentration of small ice particles but, what about the much higher percentage of aggregates and complex ice crystals seen in the larger end of the C-F PSDs seen in **Figures 51 & 52.** It is well known that the particle collision process is enhanced by increasing particle concentration, especially when the size distribution is broad so there is a large differential in fall velocities (e.g., Pruppacher and Klett, 1978). However, aggregation requires not only particle collision, but that the particles "stick" together once they collide. Several investigators have reported that the aggregation process is enhanced near 0 ° C (e.g., Sasyo 1971; Rogers 1973; Lawson et al. 1998), where the ice particles are thought to become more sticky near the melting layer. On the other hand, it has generally been thought that the likelihood of particles sticking together after colliding decreases with decreasing temperature (Pruppacher and Klett 1978). This is in contrast to several of the images of aggregates seen in C-F and mid-latitude anvils. For example, some of the CPI images of aggregates in **Figure 44** show a delicate interlacing of small particles that appear to be stuck together. Examples of aggregates that are composed of intricate structures of crystals stuck together are often observed in Florida and mid-latitude anvils (**Figure 55**), but not in KWAJEX anvils.

The much higher occurrence of aggregation in C-F clouds may be due to the much stronger electric fields in Florida and mid-latitude clouds compared with KWAJEX anvils. If lightning flashes are used as a surrogate for electric field strength, the lightning distribution shown in **Figure 42** shows that the field strengths in Florida and mid-latitudes are much stronger than near Kwajalein. **Figure 35** shows microphotographs of ice crystals that were exposed to a high (100 KV) electric field in a cloud chamber (Saunders and Wahab, 1975). The small ice crystals formed chains of particles that are very similar to those found in Florida and mid-latitude anvils. The much higher concentration of small ice

particles and aggregates in Florida and mid-latitude anvils compared with KWAJEX anvils should have a significant impact on radiative transfer calculations.

Another very interesting feature of data shown in **Table 5** is the difference between the values of effective radius calculated using two different techniques. The values are labeled R_{eff_a} and R_{eff_b} in **Table 5.** R_{eff_a} is calculated in the "traditional" way, taking the integral of the third moment of maximum particle dimension and dividing by the integral of the second moment. R_{eff_b} is calculated by computing the mass of each particle, using a new improved technique, (Baker et al. 2002), and dividing by the projected area of the particle. If there is no measurement error, the two calculations will produce equal values only when the particle is a sphere. The large difference seen in the C-F values at FL 390 between R_{eff_a} and R_{eff_b} can be explained if the particles are low-density aggregates, whose area is much greater than the mass of an equivalent sphere. This is consistent with CPI images of the ice particles observed at FL 390 in the C-F anvil. In contrast, the strong agreement between R_{eff_a} and R_{eff_b} at the FL 460 in the C-F anvil is reflective of the large number of quasi-spheroidal particles (droxtals) seen at this level. The intermediate differences in R_{eff_a} and R_{eff_b} in the KWAJEX anvil is consistent with observations of mostly blocky, irregular single particles and the relatively fewer small speroidal particles.

5.3 Dimensional and Radiative Properties of Ice Particles in Anvils

The resolving power of the cloud particle imager (CPI) provides unprecedented accuracy in measurements of crystal dimensions, including length, width, area, perimeter and derived parameters. When incorporated with the ability to automatically classify crystal habit, the CPI images yield more reliable correlations between dimensional parameters that can be used to improve parameterizations in models of radiative transfer **Table 5** lists characteristics of nine anvil clouds from which data are analyzed and presented, including thunderstorm anvils observed by the SPEC Learjet in mid-latitudes, the NASA WB-57 and UND Citation in Florida, the ARA Egrett in Darwin and the NASA DC-8 in Kwajalein.

Figure 55 shows examples of CPI images observed in continental storms in Colorado, Florida, Darwin, and in a maritime tropical storm near Kwajalein. The predominant crystal type in cirrus clouds, outside of irregulars, is the bullet rosette. Examples of bullet rosette ice crystals observed by the SPEC Learjet in a mid-latitude cirrus cloud over Utah are shown in **Figure 56**. However, inspection of over 1 million CPI images of particles observed in anvils in Colorado, Florida, Darwin and Kwajalein revealed that < 0.01% of the particles are bullet rosettes. Particles observed in the anvils of mid-latitude, Florida and Darwin thunderstorms tend to contain a high percentage of aggregates and chain-like crystals. An intensive visual analysis of the images revealed that

about 30% of the CPI images in the continental anvils are comprised of aggregates, or complex chains of particles that appear to be aggregates or heavily rimed particles, while less than 1% of the images in the Kwajalein anvil were aggregates. In addition, about 5% of the images in the continental storms appeared to be chains of small particles. These "chains" are very similar in appearance to chains of ice crystals observed in a cold chamber under a high electric field.

Table 5.
Cloud base and cloud top altitude, temperature and duration in cloud for anvil clouds.

Date	Cloud Base	Cloud Top	Temperature	Duration in Cloud
8/13/98	**FL 300**	**FL 330**	**-32 C to –39 C**	**1 hour**
8/3/99	**FL 250**	**FL 410**	**-18 C to –60 C**	**2 hours 45 minutes**
9/2/99	**FL 300**	**FL 330**	**-29 C to –39 C**	**1 hour**
6/13/00	**FL 290**	**FL 360**	**-29 C to –52C**	**3 hours**
6/8/01	**FL 150**	**FL 350**	**-3 C to -49 C**	**2 hours**
7/16/02	**FL 350**	**FL 510**	**-52 C to –63 C**	**4 hours 30 minutes**
7/28/02	**FL 400**	**FL 510**	**-57 C to –67 C**	**4 hours**
5/23/03	**FL 400**	**FL 410**	**-61 C to –64 C**	**2 hours**
5/24/03	**FL 350**	**FL 360**	**-48 C to –51 C**	**2 hours**

Regardless of whether the anvils are continental or maritime, the particle shapes in anvils bear virtually little resemblance to the shapes of particles in cirrus clouds. This can be explained through the realization that most of the ice crystals in thunderstorms are nucleated in the updrafts at temperatures > - 30 ° C. The ice particles are then carried up into the anvil. On the other hand, cirrus and wave clouds are formed in situ at temperatures that are generally < - 30 ° C, so polycrystalline structures such as rosettes are expected. The difference in the shapes of the particles in cirrus clouds, compared with those in anvils, are significantly different such that they will have substantially different phase functions (Lawson et al. 1998). The different phase functions will have a significant impact on calculations of radiative transfer. Here we compare measured maximum particle dimension and projected particle areas in various anvil clouds.

Figure 57 shows plots of projected particle area versus maximum particle length for nine anvils studied in Colorado, Florida and Kwajalein. The chain-like particles, which have the smallest area-to-length ratio, were observed in mid-latitude storms in Colorado. The blocky crystals, which have the largest area-to-length ratio, were observed in tropical storms in Kwajalein and in a storm near Cape Canaveral, Florida. Between these two extremes are curves

representative of crystals observed in Colorado and during the CRYSTAL-FACE project near Key West, Florida. The chain-like particles observed in Colorado have area-to-length ratios similar to columnar crystals. The blocky crystals observed in Kwajalein and near Cape Canaveral have area-to-length ratios closer to irregulars. These comparisons show that there can be a substantial difference between area-to-length ratios for crystals in continental versus maritime anvils.

There can also be a significant difference between area-to-length ratios from storm-to-storm in the same locale, or even within the anvil of the same storm. For example, **Figure 57** shows curves for three anvils in Colorado. Two of the anvils, 8 June and 23 May, contained mostly aggregates and chain-like crystals, while an anvil investigated on 24 May contained crystals that were more blocky, although not as blocky as the tropical anvils. **Figure 58** shows a comparison of area-to-length ratios for ice particles in two 10-km regions of the outflow region of a thunderstorm. The two regions were in juxtaposition in the same thunderstorm outflow studied by the UND Citation during the TRMM TEFLUN-B project near Cape Canaveral, Florida (**Figures 10** and **11** shows examples of CPI images in the two regions). One region contained faceted plates and aggregates of plates, while the other region was comprised mainly of rimed particles. The particles in the rimed region were likely formed in an updraft with relatively high LWC, while the particles in the faceted region were probably grown in a region with low LWC. In this case, the data sets were each fit with two curves, one for (smaller) particle sizes from 50 to 400 μm and another fit for (larger) particles > 400 μm. This was done because inspection of the CPI images and the scatterplots show that the smaller rimed particles are more chain-like than the larger rimed particles. As expected from the inspection of the images and scatterplots, the best-fit equations have significantly different slopes in the two regions. The small-particle area-to-length ratios of the rimed particles are less than the faceted particles and the reverse is true in the large-particle region. The differences between the area-to-length curves for rimed and faceted particles shown in **Figure 58** emphasize the potential variability within the anvil itself.

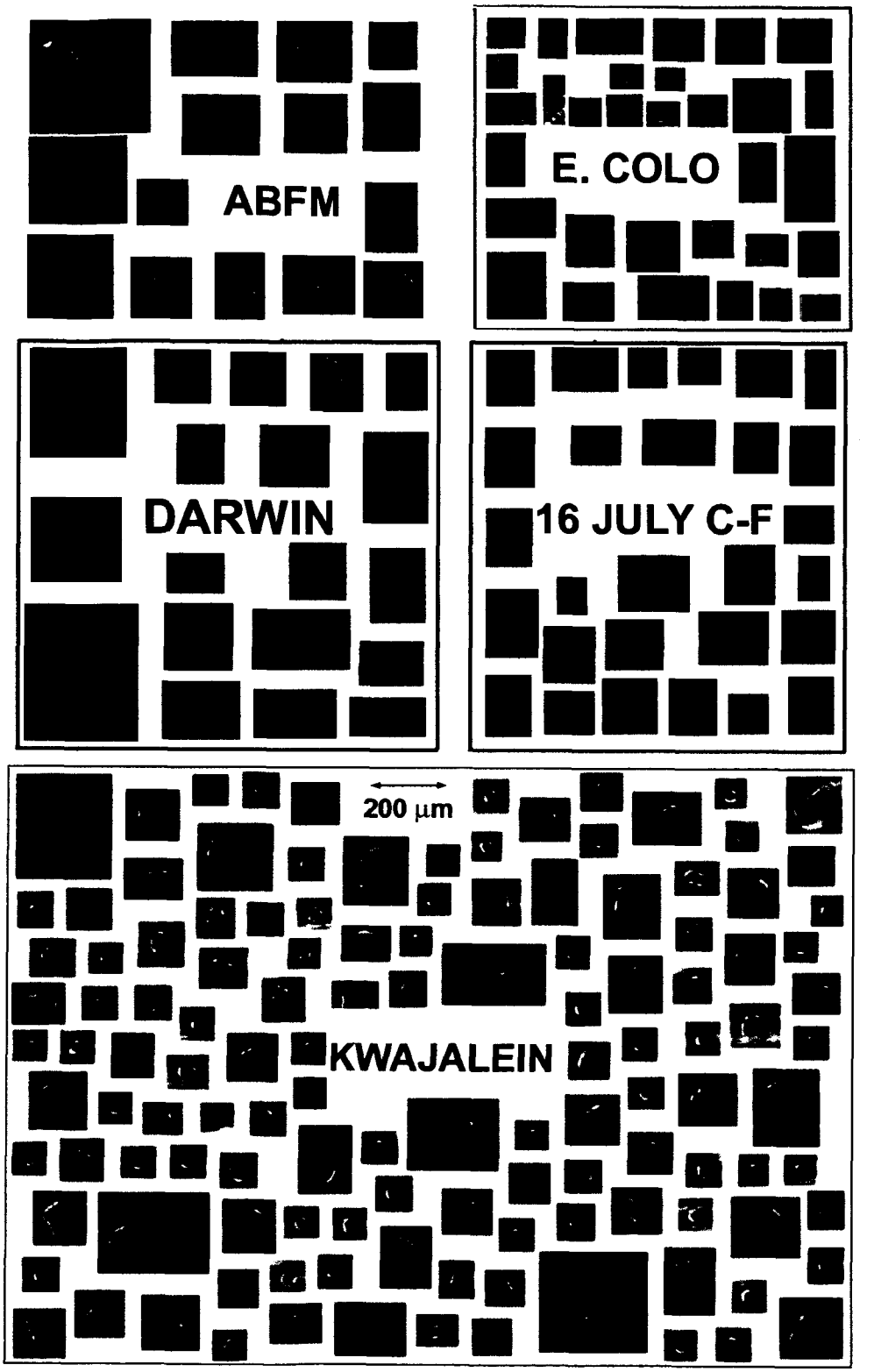

Figure 55. Examples of CPI images from (top four panels) continental anvils and (bottom panel) maritime anvil.

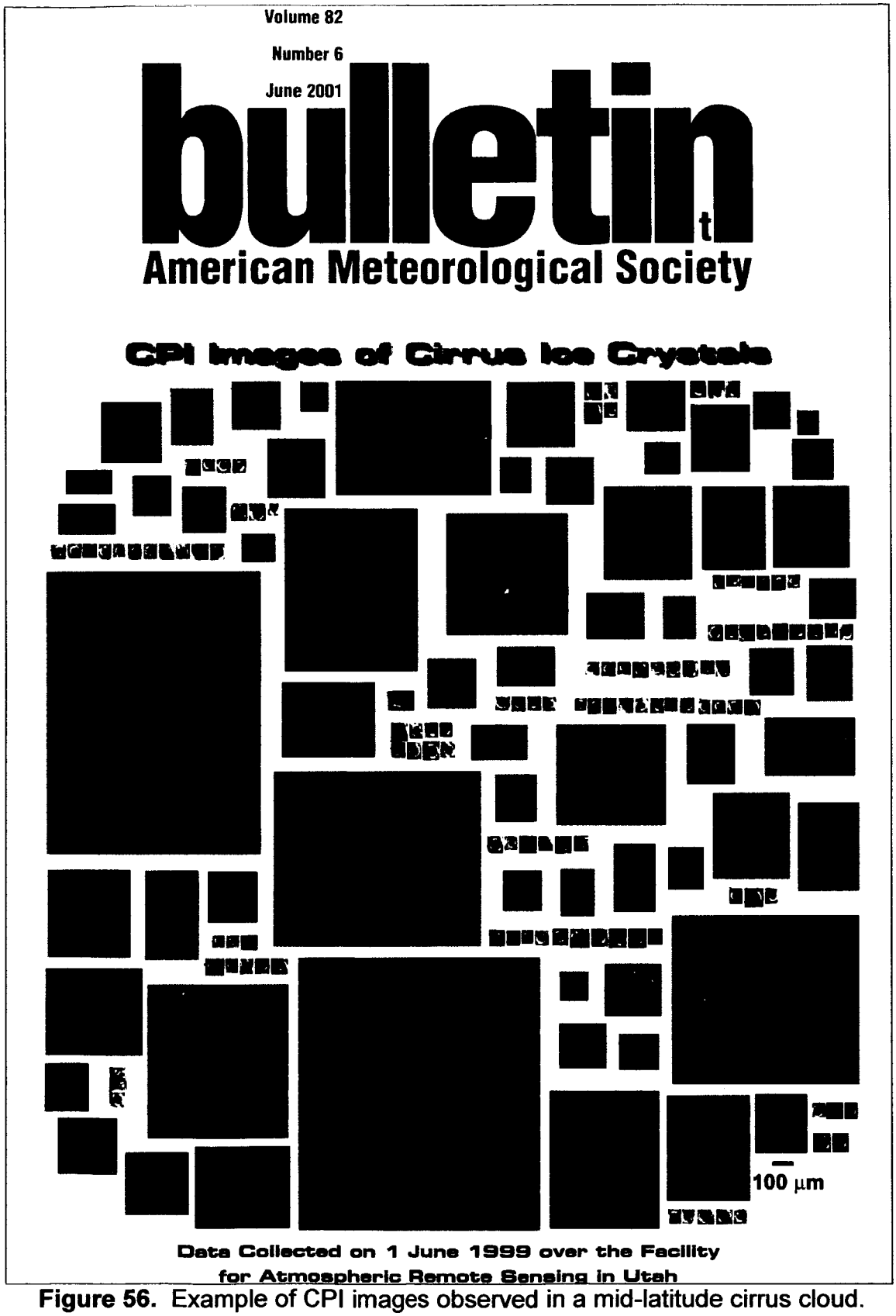

Figure 56. Example of CPI images observed in a mid-latitude cirrus cloud.

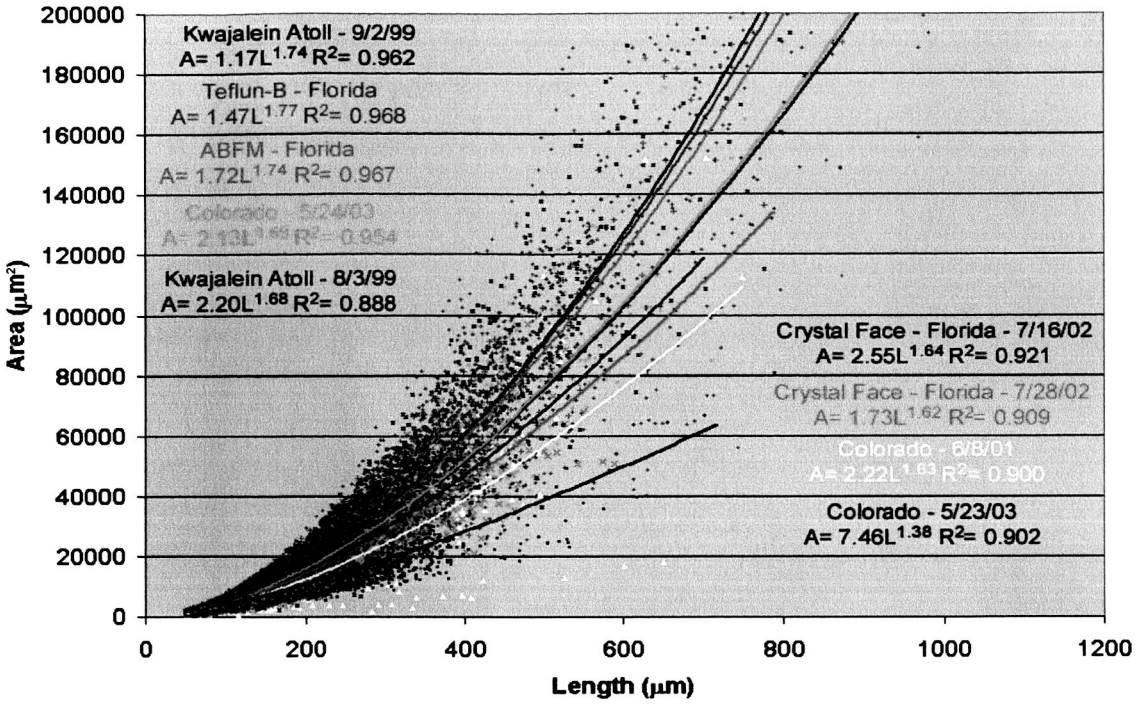

Figure 57. Plot of area (μm^2) versus length (μm) for particles observed in nine different anvils.

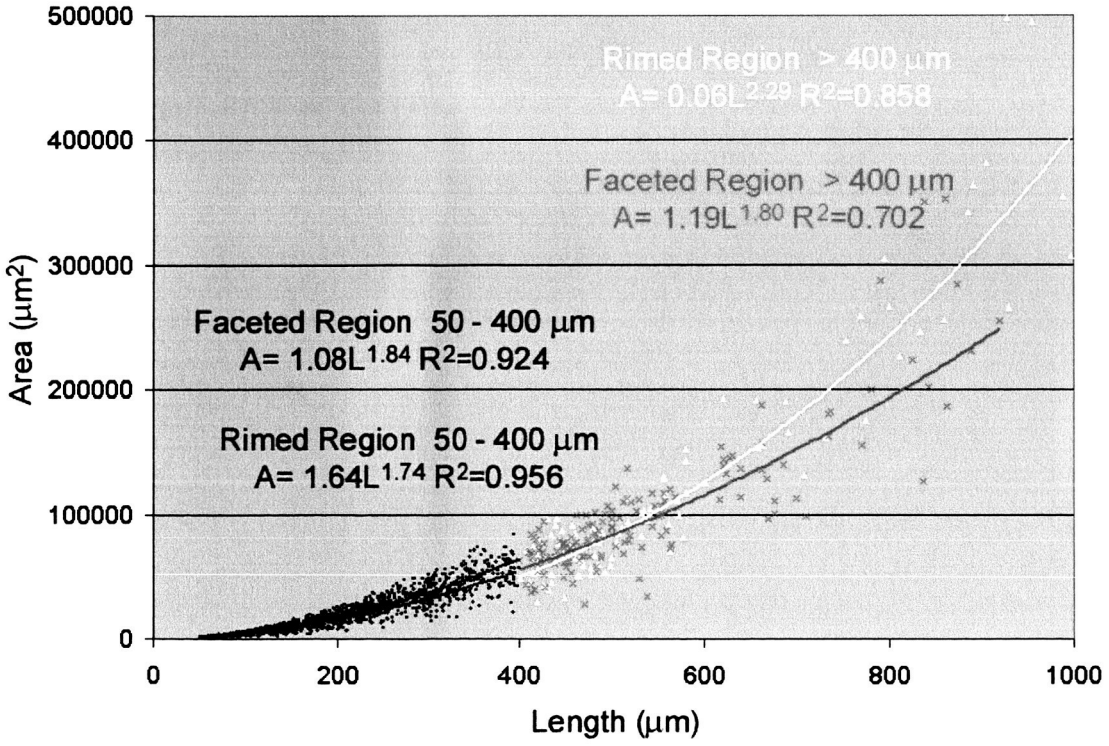

Figure 58. As in **Figure 57**, except for particles observed in two 10-km regions in juxtaposition in a Florida anvil.

5.4 Implications for Radiative Transfer

In situ microphysical measurements of wave clouds, mid-latitude cirrus, continental and tropical anvils are discussed. **Table 6** lists summary properties of each cloud type based on the microphysical measurements discussed in this paper.

Table 6. Typical values of total particle concentration (Conc.), ice water content (IWC), effective radius (r_{eff}), extinction coefficient (β_{ext}) and particle type for wave clouds, mid-latitude cirrus clouds, Continental and Maritime anvil clouds.

Cloud Type	*Conc. (No. cm^{-3})*	*IWC ($g\ m^{-3}$)*	*r_{eff} (μm)*	*β_{ext} (km^{-1})*	*Predominant Particle Type*
Wave	10 to 30	0.01 to 0.2	5 to 30	1 to 10	Rosettes and Budding Rosettes, except at T < - 50, small spheroids, Aggregates and Complex Crystals downwind of supercooled liquid
Mid-latitude Cirrus	0.1 to 10	0.001 to 0.05	10 to 30	0.1 to 1	Rosettes and Budding Rosettes for –55 < T > -25 C, Small Spheroids, few columns, virtually no plates
Cont. Anvil	10 to 100	0.1 to 2.0	10 to 50	10 to 100	Irregulars, Aggregates, Rimed particles, sideplanes, Small Spheroids, Chains of small particles
Maritime Anvil	10 to 100	0.1 to 1.0	10 to 30	10 to 100	Blocky, single-particle Irregulars, small spheroids, few columns and plates

The data in **Table 6** are a departure from number concentrations and particle shapes generally reported in the literature for cirrus and wave clouds (e.g., Heymsfield and Platt 1984; Dowling and Radke 1990). For example, Heymsfield and Platt (1984) report number concentrations from about 10 to 100 L^{-1} in mid-latitude cirrus, and the data in **Table 6** suggests that concentrations are more than an order of magnitude higher. Also, Heymsfield and Platt (1984) do not report many rosettes in mid-latitude cirrus, finding more plates and columns,

while **Table 6** suggests that rosettes are the predominant particle shape in cirrus and wave clouds.

Mishchenko et al. (1996) suggest that using the wrong phase function in radiative transfer retrievals can produce errors of a factor of three in optical depth. The phase functions used in radiative transfer retrievals and codes are often derived from ray-tracing (Takano and Liou 1995), which display a strong halo a 22 ° and a weaker halo at 46 ° for columnar and rosette crystals. Lawson et al. (1998) show phase function measurements of various crystal types grown in a cloud chamber, including bullet rosettes, which display a featureless phase function.

References

Baker, B., C. Schmitt, P. Lawson, D. Mitchell, 2002: Further analysis and improvements of ice crystal mass-size relationships. *11th Conference on Cloud Physics*, Ogden, Utah, 3-7 June 2002, P2.15.

Bashkirova, G.M. and T. A. Pershina, 1964: On the mass of snow crystals and their fall velocity. *Tr. Gl. Geofiz. Observ.*, Engl. Transl., **No 165**, 83-100.

Brown, P.R.A. and P.N. Francis, 1995: Improved measurements of the ice water content in cirrus using a total-water probe. *J. Atmos. Oceanic Technol.*, **12**, 410-414.

Christian, H. J., et al., 2003: Global Frequency and Distribution of Lightning as Observed from Space by the Optical Transient Detector, *J. Geophys. Res.*, **108** (D1), 4005.

Davis, C.I., 1974: The ice-nucleating characteristics of various AgI aerosols. *University of Wyoming, Department of Mechanical Engineering*, Ph.D. dissertation.

Dowling, D.R., and Radke, L.F., 1990. A summary of the physical properties of Cirrus clouds. *J. Appl. Meteor.*, **29**, 970-978.

Gayet J-F, P. R. Brown and F. Albers: 1993: A comparison on in-cloud measurements obtained with six PMS 2D-C probes. *J. Atmos. Ocean. Tech.*, **10**, 180-194.

Heymsfield, A., 1972: Ice crystal terminal velocities. *J. Atmos. Sci.*, **29**, 1348-1357.

Heymsfield, A.J., and R.G. Knollenberg, 1972: Properties of cirrus generating cells. *J. Atmos. Sci.*, **29(7)**, 1358-1366.

Heymsfield, A.J., and C.M.R. Platt, 1984: A parameterization of the particle size spectrum of ice clouds in terms of the ambient temperature and the ice water content. *J. Atmos. Sci.*, **32**, 799-808.

Jorgensen and Lemone 1989: Vertical velocity characteristics of oceanic convection. *J. Atmos. Sci.*, **46**, 621-640.

Knollenberg, R.G., 1970: The optical array: An alternative to scattering or extinction for airborne particle size determination. *J. Appl. Meteor.*, **9**, 86-103.

Korolev, A.V., J.W. Strapp, G.A. Isaac and A.N. Nevzorov, 1998: The Nevzorov Airborne Hot-wire LWC-TWC Probe: Principle of operation and performance characteristics. *J. Atmos. Oceanic Technol.*, **15**, 6,1495-1510.

Lawson, R.P., A.J. Heymsfield, S.M. Aulenbach and T.L. Jensen, 1998: Shapes, sizes and light scattering properties of ice crystals in cirrus and a persistent contrail during SUCCESS. *Geo. Res. Let.*, 25(9), 1331-1334.

Lawson, R. P., R. E. Stewart and L. J. Angus, 1998: Observations and numerical simulations of the origin and development of very large snowflakes. *J. Atmos. Sciences*, **55** (21), 3209-3229.

Lawson, R.P., B.A. Baker, C.G. Schmitt and T.L. Jensen, 2001: An overview of microphysical properties of Arctic clouds observed in May and July during FIRE.ACE. *J. Geophys. Res.*, **106**, 14,989-15,014.

Locatelli, J.D. and P.V. Hobbs, 1974: Fall speeds and masses of solid precipitation particles. *J. Geophys. Res.*, **79**, 2185-2197.

Mishchenko, M.I., W.B. Rossow, A. Macke and A.A. Lacis, 1996: Sensitivity of cirrus cloud albedo, bidirectional reflectance, and optical thickness retrieval accuracy to ice-particle shape. *J. Geophys. Res.*, **101**, D12, 16973-16985.

Mitchell, D.L., R. Zhang and R.L. Pitter, 1990: Mass-Dimensional Relationships for Ice Particles and the Influence of Riming on Snowfall Rates. *J. Applied Meteor.*, **29**, 153-163.

Musil. D. J., A. J. Heymsfield, and P. L. Smith, 1986: Microphysical characteristics of well-developed weak echo region in a High Plains supercell thunderstorm. *J. Climate Appl. Meteor.*, **25**, 1037-1051.

Ohtake, T., 1970: Unusual crystal in ice fog. *J. Atmos. Sci.*, **27**, 509-511.

Pruppacher, H.R., and J.D. Klett, 1978: *Microphysics of Clouds and Precipitation,* D. Reidel Publishing Company, 707 pp.

Rogers, D. C., 1973: The aggregation of natural ice crystals. Ph.D. Dissertation, University of Wyoming, Laramie, Wyoming, pp91.

Saunders and Wahab, 1975: The Influence of Electric Fields on the Aggregation of Ice Crystals, *J. Meteor Soc Japan*, 53, 121-126.

Sasyo, Y., 1971: Study of the formation of precipitation by the aggregation of snow particles and the accretion of cloud droplets on snowflakes. *Papers in Meteorology and Geophysics*, **22 (2),** 69-142.

Takano, Y. and K. N. Liou, 1995: Radiative transfer in cirrus clouds; Part III: Light scattering by irregular ice crystals. *J. Atmos. Sci.*, **52**, 818-837.

Twohy, C. H. and B. Gandrud, 1997: Ice-forming particles in aircraft exhaust. Submitted to *Geophys. Res. Let.*

Wei, D., A. M. Blyth, and D. J. Raymond, 1998: Buoyancy of convective clouds in TOGA COARE. *J. Atmos. Sci.*, **55**, 3381-3391.